Order Number 9207076

Test of the ionization threshold law through spin-dependent collisions of electrons and hydrogen atoms

Guo, Xiao-Qin, Ph.D.

City University of New York, 1991

U·M·I
300 N. Zeeb Rd.
Ann Arbor, MI 48106

A

TEST OF THE IONIZATION THRESHOLD LAW THROUGH SPIN-DEPENDENT COLLISIONS OF ELECTRONS AND HYDROGEN ATOMS

by

XIAO-QIN GUO

A dissertation submitted to the Graduate Faculty in Physics in partial fulfillment of the requirements for the degree of Doctor of Philosophy, The City University of New York.

1991

This manuscript has been read and accepted for the Graduate Faculty in Physics in satisfaction of the dissertation requirement for the degree of Doctor of Philosophy.

August 27, 1991
Date

Prof. Michael S. Lubell
Chair of Examining Committee

Sept 3, 1991
Date

Prof. Joseph Krieger
Executive Officer

Prof. Kurt H. Becker

Prof. Joel Gersten

Prof. Marvin H. Mittleman

Prof. Carl M. Shakin
Supervisory Committee

The City University of New York

Abstract

TEST OF THE IONIZATION THRESHOLD LAW

THROUGH SPIN-DEPENDENT

COLLISIONS OF ELECTRONS AND HYDROGEN ATOMS

by

XIAO-QIN GUO

Adviser: Professor *Michael S. Lubell*

Using a crossed-beam apparatus with polarized electrons and polarized atoms, the ionization spin asymmetry for atomic hydrogen, defined as $A=\frac{\sigma(\uparrow\downarrow)-\sigma(\downarrow\downarrow)}{\sigma(\uparrow\downarrow)+\sigma(\downarrow\downarrow)}$, has been measured for incident electron energies between 13.67 to 15.27 eV. In the energy range within 0.5 eV above threshold, our results reveal the failure of the conventional Wannier theory which predicts a constant spin-asymmetry. For the full energy range investigated, the presence of structure is clearly evident and is quantitatively inconsistent with any existing theoretical calculation. Moreover, our reinvestigation of the results of four previous experimental studies, all of which claimed to support the Wannier theory, show deficiencies. Our conclusion in this regard is based upon extensive statistical analyses of the published data. Finally, our reexamination of the Wannier theory also indicates a lack of selfconsistency in the theory itself.

Acknowledgements

First and foremore, I would like to express my appreciation and respect for my thesis advisor, Prof. Michael S. Lubell. I have benefited much from his knowledge and guidance during my study in The City College of CUNY. Special thanks go to Mr. Daniel Crowe for his help and effort in making this experiment possible. I appreciate very much the work done by Dr. F. C. Tang, Dr. A. Vasilakis, Prof. J. Slevin, Prof. M. Eminyan, and Prof. K. Rubin in the development of the experiment. Dr. M. R. Frankel and Mr. J. R. Friedman helped a lot in part of the data analysis. I also thank Dr. K. Becker for his help at various stages of my experiments and Dr. M. Mittleman for his discussions. The fine work performed by J. Altmann and other machinists, particularly S. Forst, in the workshop of Physics Department in City College is appreciated. The quality of the written in this thesis would not be so good without the great effort by Prof. Lubell. These years of study would not have been possible without the love, deep understanding and great support of my parents, who spent many lonely years because of my study; my wife, who bears a lot during this period; my brother, who spends a lot of time taking care of our parents. It is for them also that I have completed this thesis.

Table of Contents

List of Figures

List of Tables

Chapter 1. Spin-Dependent Atomic Scattering

The understanding of the physics associated with particle spin has led to many important advances in the history of physics. For example[1.1] the development of quantum electrodynamics was initiated in part by the fact that the g-factor of the electron differs from 2 by about 0.1%; parity violation in the weak interaction was confirmed by the measurements on the spatial anisotropy of the emitted electrons arising from the beta-decay of polarized Co^{60} nuclei; measurement of a positive spin asymmetry in the inclusive deep-inelastic cross section for scattering from a nucleon provided an important test of the quark-parton model. Since 1960, due to advances in producing polarized electrons, research on collisions between polarized electrons and atoms has grown rapidly. Some of the details of scattering processes that were previously masked, such as the spin exchange effects and fine structure effects, [1.2],[1.3] are now accessible to measurement, thus providing a much deeper understanding of the physics involved in the atomic collisions. More accurate tests of the theory are thus made possbible through the measurement of spin-dependent effects.

This chapter will provide some background information on spin-dependent atomic scattering. Sect. 1.1 introduces three of the most important spin effects: spin exchange effects; effects due to the spin-orbit interaction; and spin-orbit (hyperfine)

coupling effects. The observables are usually the spin asymmetry of the particles involved or the polarization of the emitted light. Sect. 1.2 reviews some important experimental work carried out in this rapidly growing field. Sect. 1.3, the last section, concentrates on the experiments related to the study of near threshold ionization.

1.1 Exchange, Spin-Orbit Effects and Asymmetries

In an electron-atom collision, if one traces an electron with a certain initial spin orientation, the spin of this electron after scattering will either be the same as it was or it will be "flipped". A spin-flip process can happen even without any explicit spin-dependent force, because the atomic electrons and the incident electrons can exchange their respective roles. This is called exchange scattering, in contrast to direct scattering where roles of the electrons remain unchanged. Let the target electron spins be denoted as A(↑) and A(↓) for spin quantum number +(1/2) and -(1/2) respectively, then the typical channels for the scattering are summarized as follows:[1.2]

Process	*Cross Section*	
$e\uparrow + A\uparrow \rightarrow e\uparrow + A\uparrow$,	$\lvert f-g\rvert^2$;	(1.1)
$e\uparrow + A\downarrow \rightarrow e\uparrow + A\downarrow$,	$\lvert f\rvert^2$;	(1.2)
$e\uparrow + A\downarrow \rightarrow e\downarrow + A\uparrow$,	$\lvert g\rvert^2$.	(1.3)

In the above processes, the total spins are conserved and the wave functions are antisymmetric under particle exchange. The quantity $|f|^2$ is the cross section for direct scattering, and $|g|^2$ is the cross section for exchange scattering, as is clear from the pictorial representation. In terms of the direct and exchange amplitudes, f and g respectively, the singlet (σ_s), triplet (σ_t), spin parallel ($\sigma(\uparrow\uparrow)$), and spin antiparallel ($\sigma(\uparrow\downarrow)$) cross sections can be expressed as

$$\sigma_s = |f+g|^2 \tag{1.4}$$

$$\sigma_t = |f - g|^2 \tag{1.5}$$

$$\sigma(\uparrow\uparrow) = \sigma(\downarrow\downarrow) = |f-g|^2 \tag{1.6}$$

$$\sigma(\uparrow\downarrow) = |f|^2 + |g|^2 . \tag{1.7}$$

From the above equations, it is easy to see that if only the total cross section is measured, information concerning each individual scattering process is masked. Three more independent measurements are needed in order to determine the scattering amplitudes completely (f, g, and their relative phase). This constitutes the so-called "perfect experiment."[1.4] One of the independent measurements may be the determination of the spin-asymmetry, A, the quantity studied in this thesis, which is defined as[1.5]

$$A = \frac{\sigma(\uparrow\downarrow) - \sigma(\uparrow\uparrow)}{\sigma(\uparrow\downarrow) + \sigma(\uparrow\uparrow)} . \tag{1.8}$$

The asymmetry can also be expressed as

$$A = \frac{1-r}{1+3r} = \frac{|f||g|\cos\theta}{\bar{\sigma}} , \tag{1.9}$$

where r is the ratio of the triplet and singlet cross sections, $\cos\theta$ is the phase difference between the direct and exchange amplitudes, and $\bar{\sigma} = \frac{1}{4}\sigma_s + \frac{3}{4}\sigma_t$ is the spin-averaged cross section. Therefore, if A is known, the cross sections for singlet and triplet scattering can be evaluated separately, provided the spin-averaged cross section, $\bar{\sigma}$, is also known. The balance of the "perfect experiment" might then include the measurement of polarization of electrons scattered from an unpolarized electron beam and the study of spin rotation from orthogonally polarized beams. The role

spin plays can be understood from such measurements. They provide a powerful way of studying the interaction dynamics present during a collision. In addition, spin asymmetries generally can be measured with better precision, because only ratios of quantites need to be measured at given energies, thus eliminating uncertainties associated with energy-dependent beam profiles and detector acceptances.

Neglect of spin-dependent forces is possible only for light atoms. When a beam of polarized electrons scatters from heavy atoms, the strong electric field and large angular momentum involved in the collision causes the spin-orbit interaction to play a prominent role in spin-flip effects.[1.6] The spin-dependent force is proportioonal to $\vec{L}\cdot\vec{S}\frac{dV}{dr}$, where $\frac{dV}{dr}$ is the radial derivative of the potential and where $\vec{L}$ can be considered as the angular momentum of the incident electron orbiting around the nucleus, its direction being determined once the trajectory of the electron is specified (either scattering to the right or to the left of the target atoms). Thus when the spin vector of the electron ($\vec{S}$) is reversed, the spin-orbit force changes sign and a different scattering cross section is produced relative to that of the previous spin orientation. The same effect can be obtained by observing the difference between the cross sections for electrons passing the atom to the right and those passing to the left, because the directions of the angular momentum for these two classes of electrons are opposite.

Let $\hat{n}$ be the unit vector normnal to the scattering plane. Then the dependence of the scattering cross section on spin can be written in the form[1.2]

$$\sigma(\theta,\phi) = I(\theta)[1 + S(\theta)\vec{P}\cdot\hat{n}] , \tag{1.10}$$

where $S(\theta)$ is the "Sherman function" or analyzing power characterizing the magnitude of the spin-dependent effects, $\vec{P}$ is the polarization of the electrons, θ is the polar scattering angle, and ϕ is the azimuthal scattering angle. Then the left-right asymmetry can be expressed as[1.6]

$$A = \frac{N_L - N_R}{N_L + N_R} = PS(\theta) . \tag{1.11}$$

The Sherman function is large for high-Z atoms and has been calculated to high precision (2%) for several atomic species such as gold and mercury.[1.7] Thus, a measurement of the asymmetry given by Eq. (1.11) provides a determination of the polarization of an electron beam. This is in fact the standard technique used for measuring electron polarization and is called "Mott scattering."[1.2,1.6]

In general, the electron polarization after scattering will be different both in magnitude and in direction from the initial polarization due to the spin-orbit interaction. An unpolarized electron beam, for example, can gain spin polarization of magnitude $S(\theta)$ along the normal direction to the scattering plane. Morever, only when the intitial polarization vector is perpendicular to the scattering plane will its direction remain unchanged, but its magnitude may still change (unless it already has the maximum value of unity).

The spin-orbit interaction experienced by the target electrons may also produce a left-right asymmetry in electron scattering, provided the fine structure of the atoms is resolved.[1,3] For example, consider the fine structure of a $P_{1/2}$ state. Using the simple LS coupling rule, we see that half of the atoms are in a state with total angular momentum quantum number of $m_j = +1/2$ and the other half in a state with $m_j = -1/2$. Atoms in these two states can be viewed as having opposite spins. In a collision with polarized electrons, these two classes of atoms will have different cross sections because one will effectively have a "spin parallel" configuration and the other an "antiparallel" configuration. Therefore, the target atoms are "effectively polarized." When the electron spin is flipped, there is an associated spin asymmetry, or equivalently, a left-right scattering asymmetry. This behavior is called the spin-orbit coupling effect (actually the fine structure effect). A deexcitation collision involving a fine-structure selected atoms is called "superelastic scattering."[1,3] The time-reversed process; that is, excitation of atoms to certain fine-structure states by polarized electrons, will display an analogous spin-orbit coupling effect.

1.2 Progress in Atomic Collisions with Polarized Beams

Generally speaking, the developments in the field of electron-atom collisions with polarized beams can be classified under the following areas: (1) the preparation of polarized atomic beams and their application to collisions with unpolarized electrons; (2) the advances in polarized electron sources and their application to collisions with unpolarized atomic beams; (3) the detection of both electron and atom polarization; (4) the scattering of two polarized beams; and (5) superelastic scattering involving polarized electrons. Of course, the advances in each of the above areas are related.

While optical-pumping techniques are effective methods for producing polarized alkali beams, the well known Stern-Gerlach method, and its improved versions,[1.9] are efficient ways to produce polarized hydrogen beams. In addition, the Stern-Gerlach method provides a method for measuring atomic polarization. For polarized hydrogen beams, the two-wire dipole magnet has been largely replaced by the hexapole magnet which separates the spin states at higher field (>0.8 T) and focuses the $m_s = +\frac{1}{2}$ substate at the region of interest. Studies of collisions of unpolarized electrons with polarized alkali atoms in optical pumping experiments revealed the effects of spin-exchange as early as in 1958.[1.10] Additional optical studies were carried out during the early 1960's. Exchange effects in electron-hydrogen collisions were first reported by Lichten and Schultz [1.11] who measured

the ratio of the exchange to the total inelastic cross section for the 1S-2S excitation with the use of a polarized atomic beam. Additional early studies of exchange effects in electron-alkali scattering were carried out at NYU and JILA.[1.12] The first spin-exchange measurements employing a beam of polarized electrons were reported by Hanne and Kessler [1.13] based on an experiment in which electron spin analysis was performed following the 6P-excitation from mercury.

There are several ways of producing polarized electrons.[1.2] Scattering of unpolarized electrons at high energy from high Z materials has been used to produce polarized electrons by means of Mott scattering. The spin-orbit effect can also be used at low energies to produce polarized electrons through scattering of unpolarized electrons from a mercury atomic beam. Exchange scattering from a polarized alkali vapor was also used quite a number of years ago to produce an ensemble of polarized electrons, but these ensembles were not formed into a beam.

The sources which rely on spin-orbit or spin-exchange scattering are inefficient, both with respect to the current extracted and the magnitudes of polarization produced. Photoionization of polarized alkali[1.14] (Li and K) beams by unpolarized light proved to be far more efficient. In 1969, Fano[1.15] suggested that polarized electrons could be produced if unpolarized Cs or Rb atoms were photoionized by circularly polarized light with a wavelength tuned to the Cooper minimum of the photoionization cross sections. Sources based on this effect, called Fano-type polar-

ized electron sources, produce polarization close to unity.[1.16] By today's standards however, their intensities are small, and for low-energy electron-atom scattering they suffer from a relative large (≥ 1 eV) energy spread. Field emission of electrons from magnetic materials provides beams with narrower energy spread and potentially higher currents, but changes in the beam characters under polarization reversal have restricted its development and usage.[1.2] Today, serious development continues on only two sources: the optically pumped He discharge[1.2] and the GaAs photoemitter,[1.17] the latter being used now almost exclusively in all polarized electron experiments. In its conventional form, the GaAs source is inherently limited to a polarization of ≤ 0.5 by the crystal band structure.[1.2] However, very recently a strain-induced InGaAs source was reported, which holds promise for much improved polarization. The highest polarization obtainable right now is 0.7 at a suitable incident photon energy.[1.18]

The standard way of detecting the electron polarization is based on the left-right asymmetry in the Mott scattering generally from Gold-foil targets. Originally discussed by Mott in 1929, the effect was first realized experimentally in 1943 by Shull *et al.*[1.19] The precision of Mott measurements has gnerally been limited to ±5%.[1.8] However, within the last few years, techniques have been developed that now make it possible to achieve a precision of ± 1% through the use of extremely thin-foils, energy discrimination of the scattered electrons, and calibration tech-

niques based upon double-scattering studies and optical methods.[1.20] With the high precision measurement of electron polarization vital to many scattering experiments, relatively low energy (~ 20 keV) Mott scattering has been applied in the development of a fist-size polarimeter in which targets of thorium (Z = 90 compared to Z = 79 for gold) have been used.[1.21]

Spin-dependent collisions proved to be a powerful way to study the scattering dynamics. Elastic scattering of a 50 eV electron beam on Hg and Xe by Berger and Kessler,[1.22] yielded complete sets of observables. Interesting comparisions were made by the Münster group for the angular dependence of polarization of electrons scattered elastically from mercury, thallium, lead, and bismuth[1.23] which have atomic configurations $^1S_0$, $^2P_{\frac{1}{2}}$, $^3P_0$, and $^4S_{3/2}$ respectively. Angular dependence studies as well as stuies of the energy dependence of the left-right scattering asymmmtry, normalized to the incident electron polarization for excitation of the Hg $6^3P_{1,2}$, and 6^1P_1 states were also performed at Münster.[1.24] Their results reveal the important role that spin plays in atomic collisions. Complete measurements of left-right asymmetries in superelastic scattering on Na were accomplished in 1990 by Nickich *et al.*[1.25]

Experiments involving two polarized beams, which provide significantly more information, are much more difficult to perform. The pioneering work of Alguard *et al.*[1.26] dealt with the impact ionization of atomic hydrogen and was later extended

to elastic scattering by Fletcher *et al.* at Yale.[1.26] Hils and Kleinpoppen[1.27] conducted similiar ionization measurements on potassium and sodium at Stirling while comprehensive work on the alkalis (Li, Na, K, Cs), as well as metastable helium, was carried out at Bielefeld by Baum, Raith, and their collaborators.[1.28] McClelland *et al.*[1.29] at NIST (formerly NBS) measured the spin asymmetry for elastic scattering of polarized 54.4 eV electrons from polarized Na atoms,[1.29] while Baum *et al.*[1.28] obtained spin asymmetries for both elastic and 2P-excitation for Li atoms as a function of energy. Detailed studies of asymmetry measurements on sodium, including those very close to threshold, were also performed at NIST by Kelly, McClelland, Celotta and their collaborators, and recently the NIST group performed a "perfect experiment" for elastic scattering at several energies for sodium.[1.30]

1.3 Motivations for the Near Threshold Study

The study of near threshold ionization is very important, because the problem it confronts is that of a highly correlated three-body system, the very essence of atomic physics. In this region, quantum mechanical treatments are extremely difficult and semiclassical approaches must be treated with great care. Wannier[1.31] provided the first serious analysis of the problem of two-electron escape in 1953 and predicted that near threshold the ionization cross section should vary as $E^{1.127}$, where E is the kinetic energy of the escaping electrons and where the residual ion is left with unit positive charge.

Since Wannier first derived the classical ionization threshold power law, many experiments have been performed to test the theory of two-electron escape, the earliest being perhaps the electron impact ionization studies of atomic hydrogen carried out by McGowan and Clark.[1.32] Brion and Thomas, and Merchand *et al.* all carried out early measurerments on ionization of helium.[1.33] Although confirming the predictions of Wannier, these earlier experiments suffered from the weakness that the spread in energy (typically ≥ 70 meV) of the incident electrons caused the measured ionization yield to be rounded-off at threshold. Thus even a cross-section that rises linearly from the threshold would have given a measured yield that starts with a power-law exponent greater than unity, providing the potential for a misinterpreted agreement with Wannier's prediction. Nevertheless, in the most accurate of such

measurements, that of Merchand *et al.*, adequate allowance was made for the effect of the energy spread, and a power-law index of 1.16(3) was deduced, in agreement with the Wannier law.

Vinkalns and Gailitis[1.34] predicted a uniform energy partitioning function between the two escaping electrons based on Wannier's classical treatment in 1967. Similiar calculations performed by Read[1.35] in 1984 at higher precision revealed that the partitioning function should be non-uniform within 5%. During the 1970's, the coincidence measurements by Cvejanovic and Read[1.36] for two escaping electrons in impact ionization of helium (called (e,2e) measurements in modern language) displayed an energy partitioning function that was uniform within the statistical uncertainties (15%) at an excess energy of 0.8 eV above threshold. Pichou *et al.*[1.37] performed almost the same measurements, but at more incident electron energies and angular positions. They reached the same conclusion as in the experiment of Cvejanovic and Read. High precision measurements of the energy partitioning function were performed more recently by Hammond *et al.*[1.38] in which only electrons with some constant energy were detected while the energy of the incident electron beam was scanned 2.3 eV above threshold (CRE mode). The authors claimed that their results were consistant with Read's calculations. A reexamination of both the Pichou and Hammond results will be made in Sect. 4.2.

In 1982, Donohue *et al.*[1.39] measured the cross sections of double photodetach-

ment of negative hydrogen ions very close to the ionization threshold with fine energy steps. They obtained n=1.15(4) for a functional fit of E^n. Similiar work on potassium was reported by Bae and Peterson[1.40] in 1988, who obtained a value of n = 1.16(5). Close examination of their results, however, reveal that the functional fits are not completely valid, as will be discussed in detail in Sect. 4.2.

With the developements of the polarized electron source, the test of the Wannierlaw by the study of spin-asymmetry became possible. At NIST, Kelly *et al.*[1.41] measured the ionization spin asymmetries for sodium in the threshold region and found a constant function, consistant with the prediction of the Wannier theories. Recently, however, at Bielefeld, Baum *et al.*[1.42] obtained a rising function for cesium starting from the threshold, inconsistent with the Wannier prediction. Such a rise also appears to be present for lithium, but absent for potassium.[1.28]

The triple differential cross section (TDCS) has also been studied close to the threshold as a means of investigating the angular correlation of the two escaping electrons. Early work on helium was carried out by Ehrhardt *et al.* and Schubert *et al.* at 6 eV above threshold.[1.43] Fournier-Lagarde *et al.*[1.44] first measured the TDCS for helium at low energies and found that their results did not comform well to the Wannier theory. In 1989, Schlemmer *et al.* compared the TDCS's for both hydrogen and helium at an excess energy of 4 eV and found a target dependence on the measurerd TDCS--the same results was reached when the excess energy was

lowered to 2 eV later by Rosel *et al.*,[1.45]--again in disagreement with the Wannier prediction. Further coplanar TDCS measurements for ionization of Ne, Ar, and Kr were performed by a group at Paris.[1.46] Comparision of all their results show that the TDCS also has target dependence. Recently, Pan and Starace published a theoretical explanation of the target dependence, but the validity of their calculation has been challenged by Madison.[1.47]

It should be mentioned that several experiments on higher charges of residual ions have also been used to test the Wannier theory. For a residual ionic charge of Z = 2, the Wannier theory predicts a power law of $E^{1.056}$. Experiments on the double- photoionization of helium[1.48] yielded an exponent of n = 1.05(2), in good agreement with the prediction. For triple escape of oxygen and neon, Samson and Angel[1.49] found that the cross section followed a power law with n = 2.17(9), again in agreement with the expected value of 2.162 derived by Klar and Schlecht[1.50] based on the Wannier theory. It is interesting to note that for this particular process, a second power law, $E^{1.821}$, represented their data up to 5.5 eV beyond threshold, a result that was derived theoretically later by Feagin and Filipczyk.[1.51] Lablanquie *et al.*[1.52] used single-photon double-ionization techniques for argon to study the final states of the two electron pairs. They claimed that their results supported the prediction that some final states should be suppressed in the total cross section due to nodes in the wavefunction, a result that follows from the required symmetry proper-

ties in the Wannier theory. However, Price and Eland[1.53] performed similiar experiments on xenon and mercury and did not find any evidence for suppressed state.

In general, experimental studies of any threshold problem are difficult. The cross section is very small close to threshold, and for most experiments using electron beams, it is hard to handle the low energy beam and almost impossible to get enough data close to threshold, since the energy spread of the beams is often too wide. A definitive comparision with theory is not easy. Thus, although the Wannier theory was put forward almost four decades ago, experimental investigations of its validity are still far from complete. Existing results very often make decisive judgements extremely problematic, particularly when distinctions between competing theories are attempted. For example, the results of H^- double phtodetachment experiments of Donahue *et al.* was found to be in reasonable agreement with both the Wannier power law and a modulated threshold law proposed by Temkin.[1.54] (Temkin's analysis, known as the Coulumb-dipole theory, will be discussed in Sect. 2.2.)

Regarding spin-asymmetry studies in hydrogen, the experiment of Alguard *et al.*[1.26] was unable to probe the near threshold region because of the 2.5 eV energy spread of the electron beam that was produced by the Fano-type source employed. The use of a GaAs polarized electron source, which has much narrower spread of approximately 0.17 eV(FWHM),[1.17] combined with the use of an improved atomic

hydrogen source,[1,9] have now made detailed studies of the near threshold ionization process possible. The choice of hydrogen as target atoms is very obvious since it provides the most unambigous test of the theory. The experimental results presented in this thesis represent the newest effort of the CCNY group.

Chapter 2. The Ionization Threshold Law

In 1953, Wannier[2.3] published his classical treatment of the threshold behavior of impact ionization and derived the famous threshold power law. For a residual ion of unit charge and for a $^1S^e$ two-electron final state, Wannier showed that the total ionization cross section, σ, obeyed the relation $\sigma \sim E^{1.127}$ for small values of the excess energy E. Since then, many theoretical calculations have been carried out based upon Wannier's *ansatz*. Prior to 1970, theoretical efforts concentrated on the analysis of the classical orbits for the escaping electrons. The most important results obtained during this period were the predictions that the energy partitioning function for the two outgoing electrons was a constant and the angular distribution for the orbits leading to escape between the departing trajectories had a width proportional to $E^{1/4}$.[2.6] In 1971, Rau[2.2] and Peterkop[2.5] independently obtained the Wannier power law using quantum mechanical techniques, again restricting the analysis to the $^1S^e$ final state. A year later, Roth[2.11] proved that Rau's derivation was valid even if terms of higher angular momenta were included in the Hamiltonian. The general importance of final states with higher angular momentum was first pointed out by Fano[2.4] in 1974. Subsequently Klar and Schlecht[2.12] extended Rau's formulism to include P, D, F and by extension, all other final states. Following the work of Klar and Schlecht, Greene and Rau[2.13] examined the symmetry constraints on the

Wannier law and showed that the $^3S^e$ and $^1P^e$ states were suppressed at threshold. Quantum mechanical derivations of the constant energy partitioning function and the $E^{1/4}$ power law for the angular distribution were carried out respectively by Peterkop[2.15] and by Feagin.[2.9]

As far back as in the early 1960's, Temkin[2.18–2.23] challenged some of Wannier's fundamental assumptions and developed the Coulomb-dipole (CD) model for double escape at threshold. The oscillatory features of the ionization cross section as a function of excess energy, predicted by the CD theory, have neither been proved nor been ruled out by experimental results to date.

Sect. 2.1 provides a summary of the main features of the Wannier theory. The classical derivations are discussed first, followed by the quantum mechanical treatments of Rau, Klar, Schlecht, Greene and Peterkop, with the extension of Peterkop's approach to include all the {LSπ} final states. The CD theory is discussed at the end of the chapter in Sect. 2.2.

2.1 The Wannier Model

2.1.1 Classical Treatment of the Threshold Problem

The consideration of the threshold behavior of the ionization process dates back to Wigner's 1948 seminal paper[2.1]. He asserted that the threshold behavior is a feature of the escape process only and does not involve the details of what happens in the "reaction zone" where the particles are close to each other and interact strongly. Thus, the way the "initial complex" is prepared in the reaction zone is irrelevant for the threshold law. Mathematically, such an assumption implies that the threshold law arises only through the energy dependence of the final-state wave function (as well as a phase space factor which depends on the choice of normalization for the wave function). In this way, for single electron escape, Wigner derived the threshold law

$$\sigma(E) \sim E^{l+\frac{1}{2}}, \tag{2.1}$$

where E is the available excess energy for ionizaion and l the angular momentum quantum number of the final state considered.

For the double escape problem, since the exact solution of the three-body Schrodinger equation for the final state is unknown, there is no unambigous way to derive the threshold law. However, it is instructive to look at two limiting cases at first.[2.2] If there is no screening at all, the wave functions for both electrons are only Coulombic in nature. The product of these two wave functions is the wave

function for the system, and a linear threshold law is obtained. If one electron completely screens the other electron, then one electron is represented by a Coulombic wave function and the other by a plane wave, with the consequence that an $E^{3/2}$ threshold power law is obtained.

The basic task of the conventional theory, originating with Wannier, is to generate the appropriate final-state wave function for the system. It has became common practice for such theory to use the hypershperical coordinates ρ, α, and θ_{12} defined by

$$\rho = \sqrt{r_1^2 + r_2^2}\ , \quad \tan(\alpha) = \frac{r_1}{r_2}\ , \quad \cos(\theta_{12}) = \hat{r}_1 \cdot \hat{r}_2\ , \tag{2.2}$$

where $\mathbf{r}_1$ and $\mathbf{r}_2$ are the position vectors of the electrons relative to the residual ion. When the problem is restricted to the case of an S-state (total angular momentum L = 0), the coordinate set $\{\rho,\alpha,\theta_{12}\}$ is sufficient to define the location of a configuration point. In the more general case, the system can be completely described by ρ, α, and the polar angles of the electron position vectors $\{\theta_1,\phi_1,\theta_2,\phi_2\}$. Often the five coordinates other than ρ are denoted by the symbol ω, which is used to designate final states with arbitrary total angular momentum L value.

The essential features of the double escape process were first identified by Wannier[2.3] in 1953 by purely classical analysis of the electron trajectories. He found that double escape is dominated by trajectories for which the two electrons are at almost equal distances from the residual charge center (which is considered

stationary) and move along opposite directions on either side of the center; that is, trajectories for which $\alpha \sim \frac{\pi}{4}$ and $\theta_{12} \sim \pi$. The result can be understood qualitatively as follows. If α is not close to $\frac{\pi}{4}$, one electron will screen the other. If this inner electron is slower than the other--a situation that will eventually be realized--it will be slowed down further and may eventully fall back to the nucleus, leaving only one electron free to escape from the nucleus. The condition on θ_{12} results from the $\frac{1}{r_{12}}$ repulsive potential between the two electrons, which minimizes the total energy of the system when $\theta_{12} \sim \pi$. The interaction potential can be written as $V = -C(\alpha,\theta_{12})/2\rho$, with the function C given by

$$C = \left[\frac{2Z}{\cos\alpha} + \frac{2Z}{\sin\alpha} - \frac{2}{[1 - \sin 2\alpha \cos\theta_{12}]^{\frac{1}{2}}} \right]. \tag{2.3}$$

Fig. 2.1 depicts the interaction potential of the system. From the figure, it is clear that the states corresponding to $\alpha = \frac{\pi}{4}$ lies on a ridge $\theta_{12} = \pi$. This potential energy region, which in the Wannier theory leads to the escape of both electrons, is called the Wannier ridge. With only the final-state wave function around the ridge of $\alpha \sim \frac{\pi}{4}$ and $\theta_{12} \sim \pi$ thus relevant to the ionization threshold problem in the Wannier picture, the Hamiltonian and the wave function can be expanded around the Wannier point ($\alpha = \frac{\pi}{4}$, $\theta_{12} = \pi$) to provide a basis for quantum mechanical calculations.

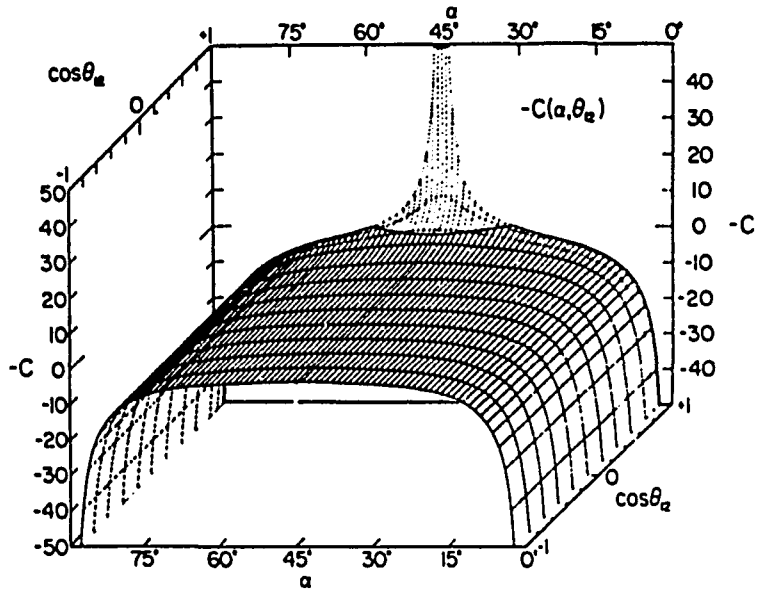

Fig. 2.1 The dependence of the potential function C on α and θ_{12}. The function C is plotted for Z = 1.

In 1974, Fano[2.4] first realized that the tight angular correlation of θ_{12} around π demands that there be a superposition of a large number of spherical harmonics for the wave function. This feature distinguishes the ionization threshold problem from some other low energy scattering processes where the S partial wave dominates and makes the study of the threshold problem unique in the understanding of two electron correlations. Nonetheless our discussion will first be limited to the $^1S^e$ state, although even in this case, the angular momenta of each of two electrons need not be zero so long as they are equal.

The Coulomb interaction for the system represented in Eq. (2.3) is long range in nature. When ρ is small, the interaction between the particles is very strong. The

system can only be described quantum mechanically. This region constitutes the so-called "reaction zone." When ρ is sufficiently large, the interaction between the particles is so weak that the kinetic energy dominates over the potential energy. This region of large ρ is called the "far zone." The region between the reaction zone and the far zone is called the "Coulomb zone" where one can apply semiclassical or classical treatments to the system. The three zones are illustrated in Fig. 2.2.

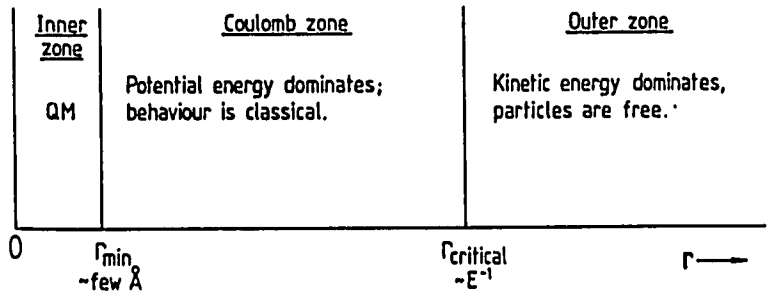

Fig. 2.2 The division of electron motions into inner, Coulomb and outer zones. The boundary between the Coulomb zone and the outer zone depends on the available energy E as shown.

We introduce two new variables,

$$\zeta = \alpha - \frac{\pi}{4} \quad \text{and} \quad \gamma = \theta_{12} - \pi \,, \tag{2.4}$$

both of which variables are small when $E \sim 0$. The classical equations for ζ and γ are separable and lead to the solution in the Wannier theory[2.5]

$$\zeta = c_{11}\rho^{m_{11}} + c_{12}\rho^{m_{12}} \tag{2.5}$$

$$\gamma = c_{21}\rho^{m_{21}} + c_{22}\rho^{m_{22}} \,, \tag{2.6}$$

where the C_{ij}'s are constants and

$$m_{i1} = -\frac{1}{4} - \frac{1}{2}\mu_i , \quad m_{i2} = -\frac{1}{4} + \frac{1}{2}\mu_i \tag{2.7}$$

with

$$\mu_1 = \frac{1}{2}\left[\frac{100Z - 9}{4Z - 1}\right]^{\frac{1}{2}}, \quad \mu_2 = \frac{i}{2}\left[\frac{9 - 4Z}{4Z - 1}\right]^{\frac{1}{2}} . \tag{2.8}$$

Eq. (2.6) shows that when $\rho \to \infty$, the two electrons will be found exactly back to back since $\mathrm{Re}(m_{2i}) = -1/4 < 0$. In addition, it can be shown that when $\rho \to \infty$, the first term in Eq. (2.5) is converging, but the second term is diverging unless $c_{12} = 0$. It can further be shown that for any finite but small value of E, both ζ and γ approach some arbitrary values.[2.3] Wannier then argued that the behavior of the angular correlation and the converging orbit in Eq. (2.5) are not crucial to the threshold law and can be neglected. In order for both electrons to escape, however, ζ must be small. Thus there must be an upper limit for the value of ζ, or equivalently, the coefficient c_{12} must have a maximun value c_{max}, which is dependent on the available energy E: as E approaches zero, C_{max} must also approach zero. Using the principle that converging electron orbits are similar to each other for different values of E, Wannier ultimately was able to show that c_{max} must obey the relation[2.3]

$$c_{max} \sim E^{m_{12}} . \tag{2.9}$$

In phase space, the volume which contains orbits leading to double escape shrinks as E goes to zero. Wannier assumed that such a shrinkage reflects the

change of the ionization cross section. Furthermore, Wannier assumed that the rate of ionization could be obtained by computing the volume in phase space which "escapes" per second from the reaction zone and which is subtended by orbits leading to double escape. Such a computation generally requires knowledge of the probability density function which describes the occupation of configuration points in phase space. However, without the full quantum mechanical solution of the problem, it is impossible to obtain the density function. Therefore, Wannier made Wigner's ergodic *ansatz* by assuming that the density of representive points of the system in phase space is constant in the mean. As a consequence, the calculation reduced to the time derivative of the volume of phase space only. Moreover, the required integration had to be performed over a surface of constant energy E and of constant ρ on the boundary of the rection zone. The total cross section then could be expressed as[2.3]

$$\sigma \sim \int d\zeta dp_\zeta d\gamma dp_\gamma , \tag{2.10}$$

where $\vec{p}$ is the linear momentum of the system. With the use of Eqs. (2.5) and (2.6), the integral in Eq. (2.10) can be expressed in terms of the c_{ij} coefficients. The range of c_{11} is not limited since it is associated with the converging orbit in Eq. (2.5). Wannier argued that the angular behavior is not crucial to the derivation of the threshold power law; that is, the ranges of c_{21} and c_{22} are irrelevant. Therefore, only the integration over c_{12} contributes to the ionization threshold law. Wannier's

famous ionization threshold law for two-electron escape follows directly and takes the form

$$\sigma \sim \int_0^{c_{max}} dc_{12} \sim E^{m_{12}}. \tag{2.11}$$

For unit residual charge (Z = 1), the power exponent is found to be $m_{12} = 1.127$ according to Eqs. (2.7) and (2.8).

In order to obtain the energy partitioning function $P(\varepsilon_1) = \frac{d\sigma}{d\varepsilon_1}$, where ε_1 is the final energy of one of the electrons, Vinkalns and Gailitis (1967)[2.6] performed a numerical integration of the classical equations for orbits leading to double escape using Eqs. (2.5) and (2.6) as initial conditions Their results showed that c_{12} was a linear function of ε_1 and could be written as

$$c_{12} \sim A(E)\varepsilon_1 \tag{2.12}$$

where A depends only on the excess energy E. Thus, they showed that the energy partitioning function was a constant function of the energy carried off by either one of the electrons. In other words, the probability of finding one of the electrons with zero energy is the same as finding it with half of the total available energy. The work of Read[2.7] many years later modified this result slightly, predicting a 5% difference between these two probabilities.

2.1.2 Quantum Mechanical Derivations

The quantum mechanical ionization cross section for the final angular momentum state L = 0 can be written in the form[2.5]

$$\sigma = \int k_1 k_2 |M(\varepsilon_1,\theta_{12})|^2 d\varepsilon_1 \sin\theta_{12} d\theta_{12} , \tag{2.13}$$

where $\vec{k}_1$ and $\vec{k}_2$ are the momenta of the two escaping electrons respectively, and the ionization matrix element M is taken as

$$M = (\Psi_f, V_{int}\Psi_i^+). \tag{2.14}$$

Here Ψ_f is the unperturbed final-state wave function, V_{int} the perturbation in the final channel, and Ψ_i^+ the exact wave function that includes the incident wave and the outgoing scattered wave. The differential cross section is just $|M|^2$. In order to perform the integration, one has to know the angular dependence of the differential cross section. For simplicity, we assume that $|M|^2$ has a rectangular dependence given by

$$\begin{aligned} M(\varepsilon_1,\theta_{12}) &= M(\varepsilon_1,\pi) , \quad \text{if} \quad \theta_{12} \geq \theta_{min} \\ M(\varepsilon_1,\theta_{12}) &= 0 , \quad \text{if} \quad \theta_{12} < \theta_{min} , \end{aligned} \tag{2.15}$$

where θ_{12} is the minimum mutual angle for which double escape will occur. The width of the angular distribution $\Delta\theta_{\frac{1}{2}}$ has been shown to be proportional to $E^{1/4}$ by the classical derivation of Vinkalns and Gailitis (1967)[2.6] as well as by the quantum mechanical derivations of Rau (1976)[2.8], Feagin (1984)[2.9], and Gailitis and Peterkop (1989)[2.10]. We thus write $\Delta\theta_{\frac{1}{2}}$ and θ_{min} in the form

$$\Delta\theta_{\frac{1}{2}} = bE^{1/4} \qquad or \qquad \theta_{min} = \pi - bE^{1/4}, \tag{2.16}$$

where b is a constant. Then the total cross section in Eq. (2.13) reduces to

$$\sigma = \int k_1 k_2 |M(\varepsilon_1,\pi)|^2 E^{\frac{1}{2}} d\varepsilon_1 . \tag{2.17}$$

In quantum mechanics, the direction of the propagating wave is normal to the surface of constant phase of the wave function. Rau[2.2] showed that there was both a converging wave and a diverging wave corresponding to Wannier's classical converging and diverging orbits. Furthermore, he showed in detail how to construct a quantum mechanical solution similar to the classical solution of Wannier at E=0 (Eq. (2.5)). The wave function Ψ_f is a superposition of both the converging wave U_c and the diverging wave U_d. Since the converging waves do not contribute to the total cross section, only the diverging wave function is relevant. Peterkop[2.5] showed that the correct final state wave function should then have the following energy dependance

$$\Psi_f \sim E^{\frac{m_{12}}{2}} U_d , \tag{2.18a}$$

where $E = \frac{1}{2} k^2$ is the excess energy, and the diverging wave has the energy dependence

$$U_d \sim E^{\frac{1}{4}} . \tag{2.18b}$$

The matrix element M has the same energy dependence as Ψ_f according to Rau's argument. Then integration of Eq. (2.13) leads to the same threshold law as Eq.

(2.11).

Rau's original derivation did not take into account the angular distribution of the ionization matrix element M. In fact, the energy dependance in Rau's M differs from that given above for Ψ_f by a factor of $E^{-\frac{1}{4}}$. Since Rau did not carry out the angular integration leading to Eq. (2.17), a procedure first suggested by Wannier, he thus arrived at the same threshold law. It should be noted that the power of the threshold law is explicitly contained in the square of the coefficient of U_d in Eq. (2.18).

Although Rau's derivation was limited to the $^1S^e$ state with the Hamiltonian containing the L = 0 term only, Roth[2.11] showed that the threshold law is unchanged if the L = 1 term is included and, in fact, suggested that the law was applicable to higher angular momentum terms as well. Klar and Schlecht[2.12] and then Greene and Rau[2.13] extended the derivation of the threshold law to all {LSπ} final states by introducing an additional function $f(\omega)$ into the final state wave function:

$$\Psi_f = f(\omega)(C(k)U_c + D(k)U_d)\,. \tag{2.19}$$

In Eq. (2.19), $f(\omega)$ is chosen to represent the symmetry properties of the {LSπ} final state. For the $^1S^e$ state, for example, $f(\omega)$ is a constant, as a consequence of which Eq. (2.19) reduces to the form used by Rau, and D(k) reduces to the energy dependent term $E^{\frac{m_{12}}{2}}$ (cf. Eq. (2.18a)) which carries the signature of Wannier's power

law. When the excess energy E is zero, it can be shown that the solutions for converging and diverging wave functions are both zero-order Bessel functions. At finite energy E, the coordinate ρ is replaced by $k\rho$, and $U_{c,d}$ assumes the form

$$U_{c,d} \sim (k\rho)^{n_{c,d}} \exp\left[i\, Q_{c,d}(\omega)(8\rho)^{\frac{1}{2}} \right], \tag{2.20}$$

where the exponent $n_{c,d}$ and the function $Q_{c,d}$ are determined from the E = 0 Schrodinger equation by requiring the sum of all terms of the order $\rho^{-\frac{3}{2}}$ to vanish. The energy dependence of the constant D can then be found, as shown by Klar *et al.*,[2.12] by requiring that as E goes to zero, the diverging wave function remains finite. The form for D and σ follow accordingly[2.13]:

$$D = k^{n_c - n_d - \frac{1}{4}} \equiv E^{\frac{n}{2}} \tag{2.21}$$

and

$$\sigma \sim E^n \tag{2.22}$$

with the exponent n calculated from the relation

$$n \equiv n_c - n_d - \frac{1}{4} = -\frac{1}{4} + \frac{1}{4}|\mu_2| \left[1 + 2 \lim_{\gamma \to 0} \lim_{\zeta \to 0} \frac{\zeta \partial f}{f \partial \zeta} \right]. \tag{2.23}$$

Two possible values for n follow from Eq. (2.23) depending upon the symmetry properties of $f(\omega)$:

$$n = \begin{cases} \frac{1}{4}(|\mu_2| - 1) & f(\omega) \text{ even when } \zeta \to -\zeta \\ \frac{1}{4}(3|\mu_2| - 1) & f(\omega) \text{ odd when } \zeta \to -\zeta . \end{cases} \tag{2.24}$$

Greene and Rau[2.13] showed that for four symmetries, ${}^1S^e$, ${}^3S^e$, ${}^1P^e$ and ${}^3P^e$, the radial interchange, $\zeta \rightarrow -\zeta$, has the effect

$$f(\omega) \rightarrow (-1)^{L+S} f(\omega) \qquad [L \leq 1, \text{ even parity}]. \tag{2.25}$$

Application of Eqs. (2.22) - (2.25) then gives $n = \frac{1}{4}(\mu - 1) = m_{12}$ (n is 1.127 for Z = 1, cf. Eq. (2.7)) for ${}^1S^e$ and ${}^3P^e$ states, and $n = \frac{1}{4}(3\mu - 1)$ (3.881 for Z = 1) for ${}^3S^e$ and ${}^1P^e$ states. Since E is very small close to threshold, contributions to the ionization cross section from both ${}^3S^e$ and ${}^1P^e$ are suppressed relative to those from ${}^1S^e$ and ${}^3P^e$ states.

For all other {LSπ} final states, the wave functions have no definite symmetry under radial interchange.[2.13,2.14] However, any wave function can be written as superposition of two functions, $f^+(\omega)$ and $f^-(\omega)$, which are even and odd under two-electron radial interchange. Klar and Schlecht[2.12] suggested that $f^+(\omega)$ and $f^-(\omega)$ give rise to independent contributions to the cross section, as a consequence of which, the even wave function leads to the Wannier threshold power law $E^{1.127}$ (for Z = 1) and the odd wave function leads to the suppressed threshold law $E^{3.881}$ (for Z = 1). Since the cross section is the simple addition of these two contributions, the Wannier term dominates. Therefore, the ionization cross sections for all {LSπ} final states except ${}^3S^e$ and ${}^1P^e$ states follow the m_{12} Wannier threshold power law.

Peterkop[2.15] performed numerical integrations of the (semiclassical) quantum

mechanical equation for the $^1S^e$ state and showed that the energy partitioning function was independent of the residual energy, ε_1, of either electron. Many authors[2.8,2.9,2.10], using both quantum mechanical and classical approaches have proved the $E^{1/4}$ power law for the angular width $\Delta\theta_{\frac{1}{2}}$ as we have already noted in Eq. (2.16).

In the Sect. 2.1.3, I will derive the threshold law without Klar's assumption about the independence of the f^+ and f^- contributions to the cross section. However, prior to that I will explore briefly the physical picture suggested by the Wannier theory. Let us first consider the effects of the so-called "dynamical screening."[2.2,2.16] As we have already noted, the Wannier threshold power exponent m_{12} depends on the charge, Z, of the residual ion. In the limiting case $Z \to \infty$, a linear threshold law is obtained, as shown by Eqs. (2.7), (2.8) and (2.11). It is obvious that this is equivalent to the absence of any screening. For the opposite extreme case, that of complete screening, for which Z = 0 in Eq. (2.8), the power exponent is 1.5, a result already stated at the begining of Sect.1.1.1. For $0 < Z < \infty$, m_{12} lies between these limits, implying that generally there is "partial screening." The escape process is thus a continuous competition between the nuclear attraction and the interelectronic repulsion. In the context of the Wannier picture, at one instant, one electron may be closer to the nucleus, but it will have higher velocity than the more distant one. As this closer electron catches up with the more distant one in radial distance,

it will lose energy, ultimately allowing the radial coordinates to approximately equilibrate. The competition between the attractive nuclear force and the dynamical screening provided by the repulsive interelectronic force leads to the strong radial correlation that characterizes the conditions for double escape. Fano[2.4] proved that this kind of behavior generally occurs for any system evolving along a potential ridge.

The angular correlation of electrons seems to be much more complex. Since the mutual angular coordinate θ_{12} is a stable coordinate, the "flux" of the particles along this "direction" is a conserved quantity. Thus the angular behavior of the two electrons should have no influence on the form of the threshold law.[2.5] The relative contribution to the total cross section of a particular state, however, does depend on the angular properties of the wave function. For example, for the $^1P^o$ state there is a node in the angular distribution. This state, although it follows the Wannier threshold law, thus has a relatively smaller cross section.

In Sect. 4.2, I will demonstrate that if one follows the semiclassical orbits and looks at the angular distribution through which the two electron escape at infinity, one finds that there are many zeroes in ζ as $E \to 0$. These zeroes may not change the "threshold law" exponent itself, but they introduce a separate energy dependence into the coefficient of the "power law," resulting in a rapid oscillation of the cross section as $E \to 0$. It appears that this behavior is enhanced when the two electrons

escape with almost equal energies.

2.1.3 Extension of Peterkop's WKB Approach

I will briefly present my derivations of the threshold laws for all {LSπ} final states based on Peterkop's WKB approach. As is well known, in the WKB approximation, the wave function can be written in the general form

$$\Psi_0 = P(\rho,\alpha,\theta)\exp\left[\, i\frac{S(\rho,\alpha,\theta)}{\hbar}\,\right], \tag{2.26a}$$

where $P(\rho,\alpha,\theta)$, the square root of the density wave function, and $S(\rho,\alpha,\theta)$, the action, satisfy the Hamilton-Jacobi equation[2.17]

$$(\nabla_1 S)^2 + (\nabla_2 S)^2 = 2(E - V)\,, \tag{2.26b}$$

and the continuity equation

$$\nabla_1(P^2\nabla_1 S) + \nabla_2(P^2\nabla_2 S) = 0\,. \tag{2.26c}$$

We expand $S(\rho,\alpha,\theta)$ in powers of ζ and γ, making use of the symmetry of the potential function around the Wannier ridge $\alpha = \frac{\pi}{4}$ and $\theta = \pi$, to obtain

$$S = S_0(\rho) + \frac{1}{2}S_1(\rho)\zeta^2 + \frac{1}{8}S_2(\rho)\gamma^2\,. \tag{2.27}$$

As shown by Peterkop,[2.17] the solutions for S_1 and S_2 obtained from the Hamilton-Jacobi equation are given by

$$S_i = \rho^2 w\frac{1}{u_i}\frac{du_i}{d\rho}\,, \qquad i=1,\ 2 \tag{2.28}$$

where $w = \left[2E + \frac{2Z_0}{\rho}\right]^{\frac{1}{2}}$ with Z_0 being the zero-order coefficient for the power expansion of the potential function, and u_1 and u_2 being hypergeometric functions.

The asymptotic behavior of u_1 and u_2 has been discussed in detail by Peterkop (1971, 1977)[2.17] and even more precisely by Gailitis and Peterkop (1989).[2.10] For the present purposes, I will use the forms originally obtained by Peterkop:

$$\lim_{\rho\to\infty} u_1 \sim E^{-m} \qquad (m \equiv m_{12} = 1.127 \text{ for } Z = 1) \tag{2.29}$$

$$\lim_{\rho\to\infty} u_2 \sim E^{\frac{1}{4}} . \tag{2.30}$$

The function $P(\rho,\zeta,\gamma)$ can be determined from Eq. (2.26c) (the continuity equation) using the form of S_i given by Eq. (2.27). Neglecting higher order terms, we obtain

$$D_0(wP^2) + \frac{S_1}{\rho^2 w}(D_1(\zeta wP^2)) + \frac{S_2}{4\rho^2 w}(D_2(\gamma wP^2)) = 0 , \tag{2.31}$$

where the D_i operators are given by

$$D_0 = \frac{1}{\rho^5}\left[\frac{\partial}{\partial\rho}\left[\rho^5\right]\right] \qquad D_1 = \frac{1}{\sin^2 2\alpha}\frac{\partial}{\partial\alpha}(\sin^2 2\alpha), \qquad D_2 = \frac{4}{\sin^2 2\alpha \sin\theta}\frac{\partial}{\partial\theta}(\sin\theta) . \tag{2.32}$$

Note that in Eq. (2.31) the higher order term neglected can be expressed as

$$G \equiv D_0\left[P^2\left[\frac{\partial S_1}{\partial\rho}\zeta^2 + \frac{1}{4}\frac{\partial S_2}{\partial\rho}\gamma^2\right]\right]. \tag{2.33}$$

Now deviating from Peterkop's approach, we write the function $P(\rho,\zeta,\gamma)$ in Eq. (2.26) in the form

$$P(\rho,\zeta,\gamma) = \sqrt{Q(\rho)}\, f(\zeta,\gamma) , \tag{2.34}$$

where we have included the function $f(\zeta,\gamma)$ to represent the symmetry properties of higher angular momentum states. (At small angles, only ζ and γ contribute to the threshold behavior, since the interaction potential is a function of these two

coordinates only--cf. Eq. (2.3)--and the wave function $f(\omega)$ can be reduced to a functional form containing ζ and γ only.[2.13] Hence we use $f(\zeta,\gamma)$ in Eq. (2.34) rather than $f(\omega)$ as in Eq. (2.19) for convenince.) Substituting Eq. (2.34) into Eq. (2.31), we obtained for small ζ and γ

$$Q(\rho) = \frac{C}{w\rho^5(u_1)^{\mu}(u_2)^{\nu}}\ , \tag{2.35}$$

where

$$\mu = 1 + \lim_{\zeta\to 0}\lim_{\gamma\to 0}\frac{2\zeta}{f}\frac{\partial f}{\partial \zeta} \tag{2.36}$$

$$\nu = 2 + \lim_{\zeta\to 0}\lim_{\gamma\to 0}\frac{2\gamma}{f}\frac{\partial f}{\partial \gamma}\ . \tag{2.37}$$

Following Peterkop, we introduce the normalization condition

$$Q \to \rho^{-5} \qquad as \qquad \rho \to \infty\ . \tag{2.38}$$

Using the asymptotic conditions on u_1 and u_2 expressed by Eqs. (2.29) and (2.30) together with the normalization condition expressed in Eq. (2.38), we see that Eqs. (2.35) - (2.37) lead to an energy-dependent behavior for the parameter C given by

$$C \sim E^{\frac{1}{2}-\mu m+\frac{1}{4}\nu}\ . \tag{2.39}$$

To obtain the differential cross sections, we use the matching procedure of Peterkop which assumes that, for ρ greater than a certain value r_0, the WKB wave function should be written as

$$\Psi = F\sqrt{Q(\rho)}f(\zeta,\gamma)exp(\ i(\frac{S}{\hbar}))\ , \tag{2.40}$$

where the matching coefficient F depends only on E. Furthermore, in the limit $E\to 0$, the wave function should be independent of E over a hyperspherical surface

of radius r_0, or

$$\Psi(r_0) \rightarrow \text{constant} \qquad as \quad E \rightarrow 0 . \tag{2.41}$$

It should be noted that the condition expressed by Eq. (2.41) is equivalent to Wannier's ergodic hypothesis. The energy dependence of F then follows from Eqs. (2.35), (2.39) and (2.40):

$$|F|^2 \sim E^{-\frac{1}{2}+\mu m-\frac{1}{4}\nu} . \tag{2.42}$$

As $\rho \rightarrow \infty$, the wave function given by Eq. (2.40) represents an outgoing scattered wave with amplitude $Ff(\zeta,\gamma)$. Now the differential cross section is given by

$$\sigma_d = \frac{(2E)^{\frac{1}{2}}}{k_i} |Ff(\zeta,\gamma)|^2 , \tag{2.43a}$$

where k_i is the momentum of the incident electron, which is almost energy independent near threshold. The energy dependence of the differential cross section thus follows as

$$\sigma_d \sim E^{\mu m-\frac{1}{4}\nu} |f(\zeta,\gamma)|^2 . \tag{2.43b}$$

The total cross section, given by an integration over hyperspherical coordinates, has the form

$$\sigma_T = 2\pi^2 \int \sigma_d \sin^2 2\alpha \sin\theta (d\alpha)(d\theta) . \tag{2.44}$$

If we now make the same assumptions for the angular distribution as in Eqs. (2.15) and (2.16), we can rewrite the integral in Eq. (2.44) and obtain an expression

$$\sigma_T = E^{\mu m-\frac{1}{4}\nu} \int_0^{(\Delta\theta_{1/2})} \sin\gamma (d\gamma) \int_{-\frac{\pi}{4}}^{\frac{\pi}{4}} |f(\zeta,\gamma)|^2 \cos^2 2\zeta (d\zeta) . \tag{2.45}$$

Since γ is assumed small, we expand the function $f(\zeta,\gamma)$ around $\gamma = 0$ and retain only the first order term. If the angular wave function has a node at $\gamma = 0$, $f(\zeta,\gamma)$ can be approximated as $f(\zeta)\gamma$; if it has no node, $F(\zeta,\gamma)$ can be approximated as $f(\zeta)$. In general, we can write

$$f_n(\zeta,\gamma) \sim f(\zeta)\gamma^n . \qquad n = 0 \ \ or \ \ 1 \tag{2.46}$$

Substituting Eq. (2.46) into Eq. (2.37) we find that ν has the value

$$\nu = 2 + 2n . \tag{2.47}$$

Substituting (2.46) into Eq. (2.45), and approximating $\sin\gamma$ as γ, we obtain a γ-integrand of γ^{2n+1}, which, after integration, contributes an energy dependent term $(bE)^{\frac{1}{4}(2n+2)} = (bE)^{\frac{1}{4}\nu}$ to the total cross section. The factor $E^{-\frac{1}{4}\nu}$ outside the integral in (2.45) is thus precisely cancelled and we obtain

$$\sigma_T = \frac{1}{2n+2}(b_m)^{\frac{1}{4}(2n+2)} E^{\mu m} \int_{-\frac{\pi}{4}}^{\frac{\pi}{4}} |f(\zeta)|^2 \cos^2 2\zeta (d\zeta) . \tag{2.48}$$

The form for σ_T given by Eq. (2.48) illustrates that the threshold law depends only on the unstable coordinate ζ and is independent of the angular behavior of the final states whether or not there is a node in the angular part of the wave function. Thus we have proved explicitly the assumption first made by Wannier and later by Rau and Klar that the angular behavior could be discarded. From Eq. (2.48) we see that the energy dependence of the total cross section is simply given by

$$\sigma_T \sim E^{\mu m} , \tag{2.49}$$

where μ, obtained from Eq. (2.36), can be evaluated in a similar way as the parameter n in Eq. (2.24):

$$\mu = \begin{cases} 1 & \text{if } f(\zeta) \text{ is even}, \\ 3 & \text{if } f(\zeta) \text{ is odd}. \end{cases} \tag{2.50}$$

We see that the ${}^1S^e$ and ${}^3P^e$ states which are even under radial interchange follow the Wannier threshold law with the power m = 1.127 for Z = 1, while the states ${}^3S^e$ and ${}^1P^e$ which are odd under radial interchange follow a suppressed threshold law with the power 3m = 3.381 for Z = 1. These results are basically the same as those obtained in Sect. 2.1.2 except that the suppressed power law is now $E^{3.381}$ (3m = 3.381) instead of $E^{3.881}$ (cf. Eq. (2.24)) for atomic hydrogen. It should be noted that Feagin obtained the 3.381 result in 1984 using a different approach.[2.9]

For all other final states we express the function $P(\rho,\zeta,\gamma)$ as a superposition of even and odd terms:

$$P(\rho,\zeta,\gamma) = \sqrt{Q^+(\rho)}\, f^+(\zeta,\gamma) + \sqrt{Q^-(\rho)}\, f^-(\zeta,\gamma)\,, \tag{2.51a}$$

where we have separated the radial and the angular coordinates to show their dependences explicitly. We substitute Eq. (2.51a) into Eq. (2.31), and group terms according to f^+, f^-, and f^+f^- respectively. Symbolically, the resulting equation can be expressed as

$$A_1(\rho)(f^+)^2 + A_2(\rho)(f^-)^2 + A_3(\rho)(f^+f^-) = 0\,, \tag{2.51b}$$

where A_1, A_2 and A_3 represent terms which depend on the radial coordinate only and contain the functions Q^+ or Q^- and their respective derivatives. Since the radial and

angular coordinates are separated completely in Eq. (2.51b), the different symmetry properties of f^+ and f^- under radial interchange lead to the conclusion that A_1, A_2 and A_3 have to be zero separately. The equations which determine Q^+ and Q^- follow immediately (Q^+ from $A_1 = 0$ and Q^- from $A_2 = 0$):

$$Q^+(\rho) = C_+ \left[w\rho^5 u_1{}^m (u_2)^{\nu_+} \right]^{-1} \tag{2.52}$$

$$Q^-(\rho) = C_- \left[w\rho^5 (u_1)^{3m} (u_2)^{\nu_-} \right]^{-1} , \tag{2.53}$$

where μ has been evaluated according to Eq. (2.36) and ν has to be calculated for each final state and for the "+" and "-" configurations separately. The solutions for Q^+ and Q^- given by Eqs. (2.52) and (2.53) automatically guarantee that A_3 will be equal to zero.

We now have to introduce two matching coefficients, F^+ and F^- for the "+" and "-" configurations in Eq. (2.51a) respectively. By using the same normalization as in Eq. (2.38) and the ergodic assumption of Eq. (2.41), we find

$$|F^+|^2 \sim E^{m-\frac{1}{2}-\frac{1}{4}\nu_+} \tag{2.54}$$

$$|F^-|^2 \sim E^{3m-\frac{1}{2}-\frac{1}{4}\nu_-} . \tag{2.55}$$

The differential cross section then takes the form

$$\sigma_d \sim E^{m-\frac{1}{4}\nu_+} |f^+|^2 + E^{3m-\frac{1}{4}\nu_-} |f^-|^2 + E^{2m-\frac{1}{8}(\nu_+ + \nu_-)} f^+ f^- , \tag{2.56}$$

where the last term in the cross section is the result of an "interference" between the "+" and "-" configurations. However, this term will disappear in the total cross section upon integration because, as can be seen from Eq. (2.48), any odd function of ζ

will not contribute to the total cross section. Note also that in accordance with the discussion accompanying Eqs. (2.45) and (2.49), we have shown that σ_T is independent of ν_+ and ν_-. Then the total cross section has the form

$$\sigma_T(LS\pi) = a(LS\pi)E^m + b(LS\pi)E^{3m} , \tag{2.57}$$

where the coefficients a and b are functions only of the symmetry properties of the individual states.

We thus have shown that restricting the problem to the Wannier ridge *automatically* decouples the "+" and "-" configurations in the total cross section, removing the need for Klar's[2.16] reasonable but rather *ad hoc* original assumption. A natural consequence of such an approach, however, is that interferences between the "+" and "-" configurations do appear in the differential cross section, an effect precluded by Klar's assumption of independence. We also note that Eq. (2.56) shows that the scaling of σ_d in energy is different for the individual {LSπ} states. Thus the electron energy partitioning function may be far more complicated than the previous prediction of almost equal probability for energy sharing. Finally we point out that the suppressed states have an exponent of 3m or 3.381 for Z = 1 rather than 3.881, in agreement with Feagin[2.9] and in disagreement with Klar and Schlecht.[2.12]

2.2 The Coulomb-Dipole Model: Temkin's Approach

In the early 1960's, Temkin[2.18] challenged the ionization description in the near threshold region proposed by Wannier. Temkin[2.19] argued that even though the strong electron-electron interaction in the reaction zone makes it plausible that the initial complex is globally insensitive to the small energy changes near threshold, parts of the initial complex may still display dramatically different energy dependences. Since only a small part of the initial complex eventually leads to double escape in the Wannier theory, Temkin argued further that the ergodic hypothesis was extremely dangerous. He also questioned the validity of the description of double escape in terms of classical orbits, which presupposes a one-to-one correspondence between the initial and final state.

As an alternative, Temkin proposed the Coulomb-dipole (CD) model[2.20] for the ionization process. He suggested that threshold ionization takes place predominantly in the part of phase space in which one electron is farther away from the nucleus than the other. Thus one electron experiences a Coulomb potential while the other one experience a dipole potential. In contrast to the Wannier picture where two electrons are at almost equal radial distance from the residual ion; that is, $r_1 \sim r_2$, the relation between the coordinates of the two electrons is now given by $r_1 \geq 2r_2$, and the transition matrix element M is calculated quantum mechanically with this restriction.

Historically, in 1968, Temkin[2.18] identified two types of variational wave functions which can contribute to ionization in the threshold region. One is the Wannier type, and the other is associated with the dipole interaction. By considering the threshold problem as an analytic continuation of inelastic scattering, Temkin[2.21] suggested that an oscillatory feature should be presented in the ionization cross section, presumably due to the dipole interaction. Temkin began a direct calculation of the cross section using a two dimensional model[2.20] in which the two electrons escape exactly back to back in the same plane. In 1982, with the effects of a dynamic dipole moment included, Temkin found that the threshold law assumed the form[2.20]

$$\sigma(E) \sim \left[\frac{E}{(ln(E/5))^2}\right]\left[1 + D\ sin(\alpha lnE + \phi)\right], \qquad (2.58)$$

where D, α and ϕ are constants and where the factor $(lnE)^2$ in the denominator arises from dynamical correlations. Temkin also found that the energy partitioning function had oscillations in it, compared to an essentially constant function predicted by the Wannier theory. The functional form Temkin obtained is given by[2.23]

$$\sigma_E(\varepsilon) \sim \frac{1 + cos[\alpha(R) ln\varepsilon + c]}{(ln\varepsilon)^2}, \qquad (\varepsilon \le \frac{E}{5} \quad or \quad \varepsilon \ge \frac{4E}{5}) \qquad (2.59)$$

where α and c are again constants. It was not until very recently that Temkin and his co-workers[2.24] finally included the mutual angular dependence of the electrons in the Coulomb-dipole theory. When the excess electron energy, E, lies between 0.3

and 250 meV, the form of the threshold law remained the same as in Eq. (2.58). However, in the "true" threshold region, where E is less than 0.3 meV, a region which cannot be reached with today's technology, they found that the threshold law differed from Eq. (2.58) with a logarithmic factor of $(lnE)^4$ substituted for $(lnE)^2$ in the denominator. They also found that the energy partitioning function remained basically the same as that given by Eq. (2.59), but with the denominator again changing for the two energy ranges as in the case of the expression for the total cross section.

In 1984, Temkin[2.23] examined the role of spin and showed that the cross sections for singlet and triplet scattering had the same functional form, but with different constants. Since the asymmetry A is sensitive to the ratio of the triplet and singlet cross sections, as illustrated by Eq. (1.9), the oscillatory behavior can be expected to remain. Given their relative freedom from systematic effects, spin-dependent asymmetry measurements thus provide excellent potential for detecting oscillating structures in the ionization cross section.

We briefly outline the mathematical derivation of the CD predictions[2.24]. The yield, σ, of positive ions during ionization is given by the "golden rule,"

$$\sigma = \int |M|^2 \delta(E - k_1^2 - k_2^2) d\vec{k_1} d\vec{k_2}\,, \tag{2.60}$$

where M is the transition matrix element that Temkin took in the final-state form expressed by

$$M = < \Psi_f^- | V_f | \Phi_i > . \tag{2.61}$$

Here V_f is the interaction potential defined by

$$V_f = -\frac{2}{r_1} + \frac{2}{r_{12}} , \tag{2.62}$$

Φ_i is the initial state wave function taken as the product of the unperturbed ground state wave function for the target electron and a plane wave for the incident electron, and Ψ_f^- is the final-state wave function taken as the exact solution with incoming spherical wave boundary conditions. Temkin approximated the incident plane wave by a spherical Bessel function of zero order and the final state wave function by the product of a dipole wave function for one electron and a Coulombic wave function for the other one at given angular momentum l. The dipole wave function, $F_l^d(r_1)$, satisfies the equation

$$\left[\frac{d^2}{dr_1^2} - V_{CD} - \frac{l(l+1)}{r_1^2} + k_1^2\right] r_1 F_l^d(r_1) = 0 , \tag{2.63}$$

where V_{CD} is the Coulomb-dipole interaction potential deduced from the full interaction potential V_f with the restriction $r_1 \geq 2r_2$. The form of V_{CD} is given by

$$V_{CD} = -\frac{2r_2\cos\theta_{12}}{r_1^2} , \tag{2.64}$$

the numerator, $2r_2\cos\theta_{12}$, reflecting the dynamic influence of the dipole moment.

For the calculation of the transition matrix element, certain limitations are applied to the spatial integration. First, the coordinate of the slower electron, r_2, must be greater than a certain minimum value R, as a consequence of which, r_1 has a lower limit of 2R. Only above this value is the Coulomb-dipole interaction

meaningful. Ssecond, a restriction is necessary to make the highly non-separable Coulomb-dipole equation of Eq. (2.63) ammenable to solution: the dipole potential V_{CD} must be greater than the kinetic energy k_1^2 of the faster electron. Since the dipole potential falls rather rapidly, an upper limit, r_1^{max}, is taken. In summary, the restrictions are expressed by

$$r_1^{max} \geq r_1 \geq 2r_2 \geq 2R \ . \tag{2.65}$$

The difference in the total cross sections for the two energy regions mentioned earlier (E < 0.3 meV and 0.3 meV < E < 250 meV) arises from the approximations used for the $ln(k_1r_1)$ term that appears in the integrand when the integrals imcorporated in Eqs. (2.60) and (2.61) are carried out over momentum and configuration space. In the "true" threshold region, k_1 is very small, and the term is just $\ln(k_1)$, while in the higher energy region, $ln(r_1)$ is used, since k_1 is rather large and r_1 is bounded by r_1^{max}. The total cross section is a summation over all the angular momentum states with each term in the sum having the same functional form given by Eq. (2.58), but with constants that depend upon the angular momentum.

In the CD theory, as suggested by Eq. (2.65), only part of the spatial integration of the transition matrix element in Eq. (2.61) is actually evaluated. As a result, the relative contribution of the dipole interaction to the total cross section may be quite small. Indeed, the lower limit of r_2 has been estimated to be around 400 Bohr radii, implying that the unevaluated contribution from the space inside R may be

quite significant. Temkin has already started to evalute this "inside" contribution which is not strictly dipole in nature.[2.25] The quantum defect calculation of Greene and Rau[2.26] seems to substantiate the need for extending the calculation to the inside region. In their calculation, the parameter D in Eq. (2.58), which reflects the strength of the dipole contribution, is explicitly given as $e^{-\pi\alpha}$, with α the (fixed) dipole moment. Even if one takes the smallest possible value of α (in atomic units) as 1 Bohr radius, $e^{-\pi\alpha}$ is still only 4%. It would therefore appear that the "inside" contribution is dominant, a fact which Temkin has acknowledged in his latest work. He has argued however, that oscillations in the cross section are reflected even in this region.

Chapter 3 Experimental Method

In this chapter, I will present the details of the experimental apparatus used for the spin-tagged near threshold ionization studies, emphasizing in Sects. 3.1 and 3.3 the performance and characteristics of both the polarized electron beam and the polarized hydrogen beam. To demonstrate the high quality of the data obtained, I will also discuss at length the procedures used for data acquisition. The importance of the experimental lifetime of the GaAs crystal used in the polarized electron source will become clear from the description of the energy calibration of the electron beam contained in Sects. 3.2 and 3.3. The great effort paid to the statistical analysis of the data and the search for systematic effects through the analysis of false asymmetries will be covered in Sect. 3.4. Finally, a discussion of possible background effects, due to Rydberg atoms, metastable atoms, hydrogen molecules and photons will be presented in Sect. 3.5.

3.1 Apparatus

3.1.1 Overview

The crossed-beams apparatus for the experimental studies in this thesis is shown schematically in Fig. 3.1. It consists of five major units: a polarized hydrogen source, a polarized electron source, an interaction chamber, computer automation devices, and a hydrogen beam-dump section. Hydrogen molecules (Research Grade, 99.997% purity) were rf dissociated in a Slevin-type source and allowed to effuse through a skimmer-collimator into a pair of high-field hexapole magnets that selectively transmitted the $m_s = +\frac{1}{2}$ atoms and focused them at the crossed-beam interaction point.[3.1] The polarized hydrogen source was differentially pumped, the Slevin source itself being equipped with a diffusion pump (Torr Vacuum, model # R-620, with effective pumping speed of 1160 l/s for air and 2500 l/s for hydrogen molecules, taking into account conductances) and the hexapole magnet section with a turbo-pump (Balzers, type TPU-200, 100 l/s for air and 200 l/s for hydrogen), each backed by an appropriate mechanical pump. Upon emerging from the second magnet, the atoms entered a small solenoidal field which adiabatically rotated the spins into a longitudinal direction either parallel or antiparallel to the direction of the atomic beam depending upon the direction of the solenoidal field. Further dowmstream, a pair of coils ensured that the magnetic field was maintained in the same longitudinal direction with a magnitude of about 100 mG at the interaction

point. A mechanical chopper located between the two magnets permitted "real-time" background subtraction. The hydgrogen beam was sampled in the beam-dump section by a quadrupole mass analyser (QMA) (V/G Supavac, model # 28001), capable of transverse horizontal motion that permitted residual gas backgrounds to be measured when the beam was operating. Both an ion pump (Perkin Elmer, model # 207-0120, 115 l/s for air and 315 l/s for hydrogen) and a cryopump (CTI-Cryogenics, model # 3996086, 1000 l/s for both air and hydrogen) were used in this section to ensure proper temporal behavior monitoring of the beam. A Stern-Gerlach "two-wire-field" magnet originally installed in this section for polarimetry purposes was removed for my experiments to provide more precise intensity monitoring.

Polarized electrons[3.2] were produced by photoemision from a <100> GaAs crystal. A GaAlAs diode laser (Sharp, model # LT021) provided linearly polarized light with wavelengh of 780 nm and maximum power of 15 mW. Circularly polarized light was obtained with the use of a half-wave-plate which rotated the linear polarization and a quarter-wave-plate which provided 90° phase retardation. The circularly polarized light was focused onto the GaAs crystal with a spherical lens. A linear motion feedthrough permitted the crystal to be moved vertically upward from its normal operating position into a location suitable for activation with Cs and O_2 gas. With the crystal in the operating position, the photoelectron beam was

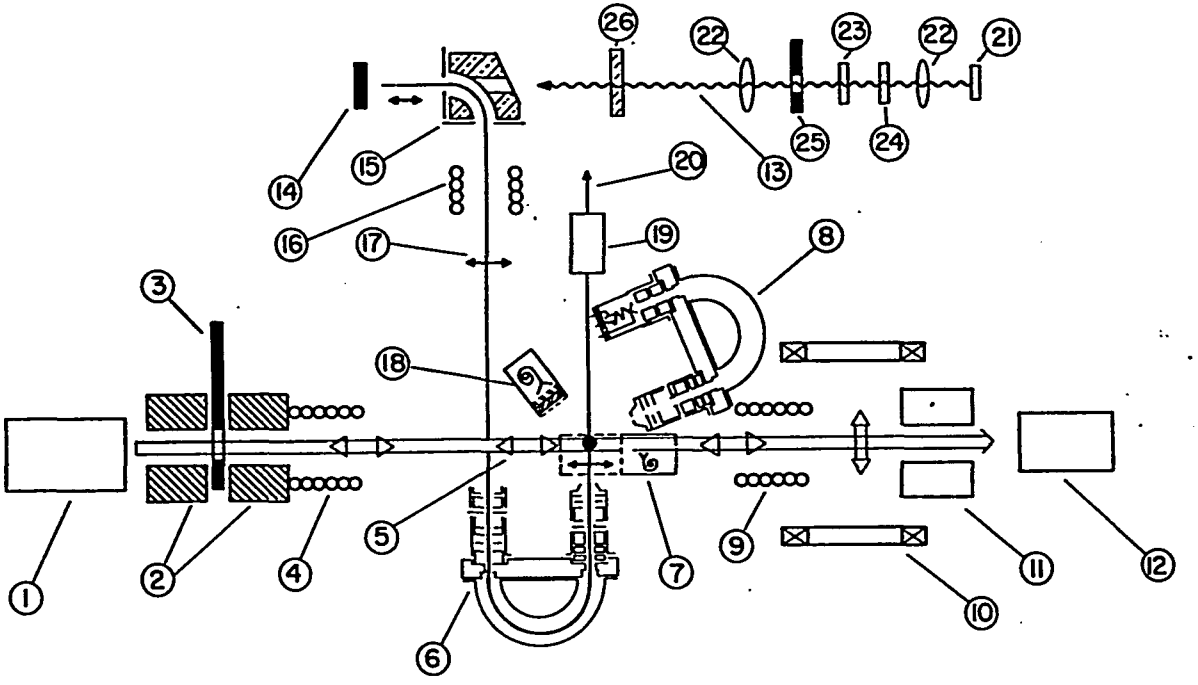

Fig. 3.1. Schematic layout of the experiment showing (1) hydrogen source, (2)hexapole magnets, (3) H-chopper, (4) solenoid, (5) hydrogen polarization vector, (6) electron monochromator, (7) ion detector, (8) electron spectrometer, (9) soleniod, (10) adiabatic spin ratator, (11) Stern-Gerlach magnets, (12) QMA, (13)780 nm laser beam, (14) GaAs crystal, (15) 90° spherical bender, (16) solenoid, (17) electron polarization vector, (18) Lyman-α detector, (19) Faraday cup, (20) exit to Mott polarimeter, (21)diode laser, (22) lenses, (23) $\frac{\lambda}{4}$ plate, (24) $\frac{\lambda}{2}$ plate, (25) laser beam flag, (26) vacuum window. Items (8), (18) and (20) were not used in the studies in this thesis.

extracted horizontally and then deflected downward by a 90° electrostatic bender. The beam was transmitted by a series of electron-optical elements into the interaction chamber, where a 180° hemispherical monochromator was used to limit the energy spread at the interaction site.[3.5] A Faraday cup located beyond the interaction region was used to monitor the electron current.

To reduce the influence of unwanted magnetic fields, the whole interaction chamber was shielded with a Mu-metal cylinder capped at top and bottom but with appropriate ports for beam passage, pumping capabilities and feedthrough access. Magnetic fields at the interaction site were monitored with a Hall probe (Bell, model 620) inserted into an OFHC copper tubing finger that extended into the chamber. In this way the resultant magnetic field vector could be held to within about 3° with respect to the direction of the hydrogen beam line, corresponding to a mean cosine factor of about 0.99. The region where collisions take place was electrostatically shielded by a stainless steel mesh containing two 90° transparent meshes downstream of the interaction region for additional shielding. A channel electron multiplier (CEM), preceded by a grid to prevent electrons or negative ions from reaching the CEM cone, served as an ion detector. The CEM was also shielded by the stainless steel box that extended downstream from the interaction region and had dimensions sufficient for 4π-srad ion collection for incident electron energies up to 1 keV. With the voltages at the grid and cone set at -650, and -700

volts respectively, the ion detection efficiency was about 10% (a compromise between rejection of negative particles and positive ion counting efficiency). After baking for a few days, the base pressure in this chamber reached about 2×10^{-9} Torr. With the hydrogen beam chopper open during data taking, the pressure rose to about 5×10^{-9} Torr.

The whole data taking procedure was computer automated once the initial settings were entered. The acquisition and control electronics consisted of a PDP - 11 microcomputer, several analog to digital converters (ADC) for data recording, and digital to analog convertors (DAC) for automatic controlling of the apparatus through interfacing I/O modules. The H-beam status (chopper open and closed), the $\frac{\lambda}{2}$ plate and the $\frac{\lambda}{4}$ plate orientations, and the QMA signals (H or H_2) were monitored along with the horizontal position of the QMA set and recorded by the computer in accordance with programmed sequencing. Fortran IV with assembler subroutines were combined to control the data taking procedure. Data were recorded in 8 inches diskettes, and then transferred to a VAX 780 for off-line analysis and storage on magnetic tape.

3.1.2 Polarized Electron Beam

In Fig. 3.2, a detailed picture of the GaAs polarized electron source is presented.[3.2] The six-way stainless-steel cross chamber was pumped by a 150 l/s conventional diode-type ion pump (Perkin Elmer, model # 207-0160) located on one of the side port (out of the plane of the paper). The circularly polarized laser beam shown incident from the right side in the figure, passed through a hole in the 90° electrostatic bender and impinged on the GaAs crystal with an estimated spot size of about 1.5 mm x 1 mm. Two SAES Getters (model St 101-Cs) cesiators, suspended above the bender, were used for activating the crystal which was lifted upward by a linear motion feedthrough located on the top flange. An electrical feedthrough provided all the connections to the electron-optical elements inside the GaAs source chamber as well as to all elements used for activation (ohmic-heating of the crystal, heating currents for the cesiators, bias voltages, and photocurrent monitor). The GaAs crystal used in this experiment was Zn-doped to a carrier concentration of 10^{19} cm^{-3}. It was clamped to a sapphire holder for insulation by a pair of tantalum clamps, which served as electrodes for both heating of the crystal during cleaning and biasing of the crystal during normal operation. The oxygen line (port out of the plane of paper in Fig. 3.2) was equipped with a leak valve (Granville Phillips, series 203) to control the flow of O_2 gas into the chamber. The whole system was bakable to 250°C which produced an ultrahigh vacuum pressure of

5×10^{-10} Torr in approximately a week.

Essential to the success of this experiment was the extended lifetime of the GaAs crystal, which was achieved through the use of an *in-situ* cesiator embedded in the extraction anode.[3.3] The detailed design is shown in Fig. 3.3. A circular molybdenum disk, 0.635 mm thick with an aperture 4 mm in diameter served as the anode. About 10 mm from its center, a slot measuring 2 mm x 2 mm x 38.1 mm permitted the *in-situ* cesiator to be mounted flush with the anode surface. The cesiator was crimped into OFHC cooper blocks at its ends and insulated from the anode by Macor insulating pads. To reduce the influence of the electric field of the cesiator on the electron beam, the cesiator was biased at the same voltage as that of the anode. Thus during normal operation, with the voltage across the cesiator maintained at about 3.8 volts and the current through it at about 4 A, the central region of the cesiator remained at the potential of the anode. However the passage of the current through the cesiator created a magnetic field that had a significant effect on the tuning of electron optics. To compensate for this as well as for the earth's magnetic field, three pairs of quasi-Helmholtz coils were installed. Two of them were placed to produce magnetic field components in the horizontal plane, with their coils wound around the flanges of the GaAs source chamber. The third one, which consisted of two big coils surrounding the entire electron beam line, produced a vertical component. In the cooled polarized electron source, which I will discuss in

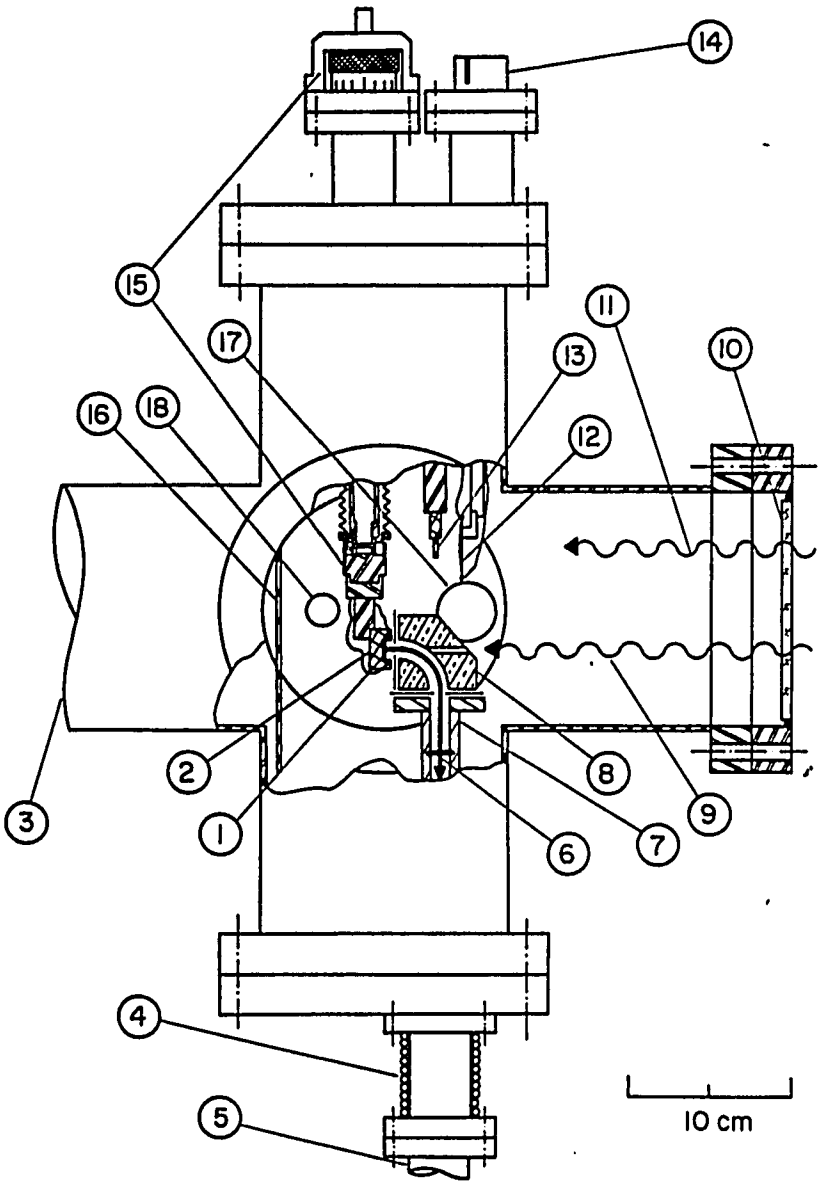

Fig. 3.2. Schematic drawing of the electron source showing (1)GaAs crystal, (2) sapphire mounting block, (3) titanium sublimation pump port, (4) solenoidal electron spin precessor, (5) beam pipe to interaction chamber, (6) transversely polarized electron beam, (7) electron transport optics, (8) 90° spherical bender, (9) *in situ* GaAlAs laser beam, (10) vacuum window, (11) activation HeNe laser beam, (12) cesium dispensor, (13) electron collector, (14) electrical feedthrough, (15)linear motion feedthrough for lifting GaAs crystal, (16) sublimation pump baffle, (17) roughing line port, and (18) oxygen line port. Not shown is the 150-l/s conventional ion pump.

the last chapter, two cesiators were placed symmetrically on either side of the anode aperture and opposing currents were used in order to null the magnetic field.

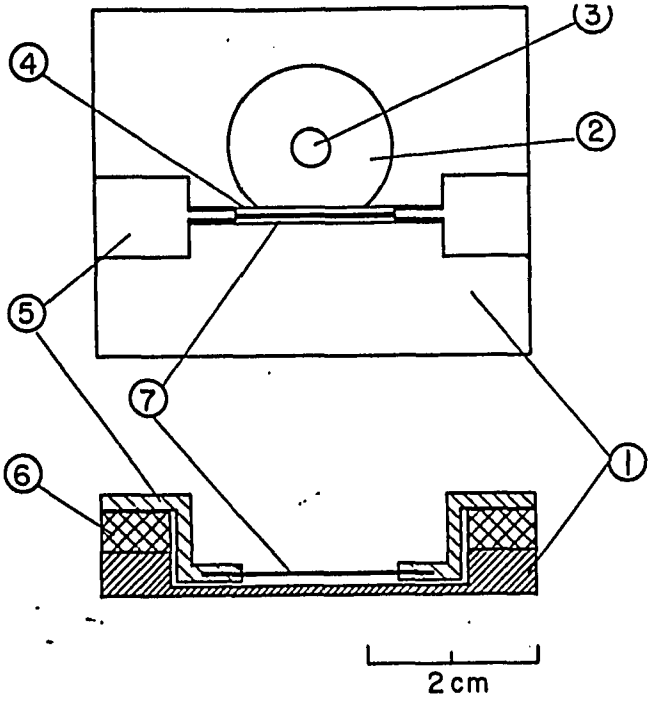

Fig. 3.3. Scale drawing of anode extractor with embedded cesium dispenser showing (1) stainless-steel plate, (2) molybdenum anode, (3) anode aperture, (4) cesiator mounting slot, (5) Macor supports, (6) OFHC cooper, (7) and SAES Getters cesiator

A 90° electrostatic bender, fabricated from OFHC copper, and a series of transport electrostatic lenses, fabricated from Arcap, were used to provide a focused beam at the entrance plane of the "input optics" of a 180° monochromator in the interaction region.[3.4] The transport optics[3.5,3.6] consisted of a two-cylinder immersion lens with acceleration, a three-cylinder einzel lens, and a three-cylinder immersion lens with deceleration. The monochromator, fabricated from molybdenum, consisted of an input aperture-lens, two concentric hemispheres, an output

lens, and a zoom lens. The input optics, which incorporated 1.8 mm diameter apertures as spatial limiters, was used to focus the beam at the aperture (also 1.8 mm in diameter) at the entrance plane of the two hemispheres. Another aperture, also 1.8 mm in diameter, located in the exit plane of the hemispheres served as a dispersive stop at the object plane of the final section of the transport optics. The final section of the transport system was the "output optics" of the monochrometor, which was designed to focus the beam at the intersection point over a wide energy range (0 - 1000 volts) with the use of a zoom lens. To provide a wide operational energy range, the first section of the output optics could be run either as a two-element lens for both high energies ($E > 100$ eV, with deceleration) and for low energies ($E < 10$ eV, with acceleration), or as three-elements lens for intermediate energies range ($10 \text{ eV} < E < 100$ eV). The zoom lens was a three-element aperture lens. The potential of the first aperture was the same as that of the final element of the first section of the output optics. The potential on the second aperture was variable according to the electron energy, and the potential of the last aperture was held at ground, as was the shielding cylinder and cone which surrounded the "input optics." The electron beam diameter at the intersection point was calculated to be about 3 mm.

All the voltages applied to the elements of the transport optics were referenced to the bias of the GaAs crystal. The latter determined the norminal electron beam

energy at the grounded intersection point. (The determination of the precise collision energy will be discussed in Sect. 3.3.) These voltages were obtained from voltage dividers connected across a 2 kV high voltage power supply (Bertan, model # 210-03R). The negative bias on the crystal was provided by two power supplies in series, one which provided coarse tuning between 0 and 1 kV (Kepco, model APH 1000M) and the other which provided fine tuning between 0 and 7.5 V (Lamda, model LDS-X-01). Steering plates in the transport optics were biased symmetrically with respect to the local beam voltage with the use of floating power supplies and potentiometers. The voltages applied to each element was monitored by an digital multimeter (Fluke, model # 8010A).

Operation of the electron optics proved to be more difficult than expected. Since the crystal mount was fixed, small errors in the crystal position with respect to the anode could not be corrected. (It should be noted that the physical position of the GaAs crystal was not the effective object position of the electron beam. A point object was actually formed twice as far away from the anode as the position of the GaAs crystal due to a uniform electric field between the crystal and the anode.[3.7]) It was found in practice that the voltages on the three-cylinder immmersion lens in front of the input optics for the monochromator had to be changed from set {750, 150, 37.5} (voltages on each element in sequence) to the empirical set {715, 185, 51}. Despite these difficulties, an 85% transmission efficiency was

obtained for the beam transported to the entrance plane of the input optics of the monochromator.

The monochromator operation also proved to be more difficult than expected. The path length of the electrons inside the monochromator was 50.8 mm. Thus a magnetic field of 50 mG could deflect an electron beam with 3 eV pass energy by 4^0. For reasons described in Sect. 3.1.3, the magnetic field produced by the several coils used for guiding the atomic hydrogen spins, had to be increased beyound their design values and could have produced stray fields as large as 100 mG in parts of the monochromator. These fields could well have been responsible for the difficulties encountered in the operation of the monochromator. A more detailed discussion of the performance of the monochromator is included in the Appendix 1.

3.1.3 Polarized Hydrogen Beam

Since the general features of the hydrogen source were discussed in Sect. 3.1.1, I will concentrate in this section on some of the design detail, shown in the Fig. 3.4.[3.1] The far left side of figure shows the nozzle of the rf discharge tube. As indicated, it was 1 mm in diameter and was fabricated with a kink in the output end that effectively eliminated the emission of any discharge radiation. The effusing atoms were formed into a beam by a stainless steel skimmer 1.4 mm in diameter having a 30^0 cone angle and mounted 16.5 mm away from the exit of the nozzle. Located 25.4 mm further downstream from the skimmer was the entrance to a pair of high-field (0.85 T pole-tip field strength) hexapole magnets each 152 mm long and having a pole gap of 6.4 mm. The two state-selecting magnet sections were separated by a 19 mm space to improve pumping.

The state-selected beam passed through a gate valve which could isolate the polarized hydrogen source from the ineteraction chamber. Upon entering the interaction chamber, the beam was collimated by a conductance-limiting aperture and tube around which a spin-guiding solenoid was wound. This solenoid, together with two additional coils mounted near the interaction region, ensured that spins of the atoms transported to the interaction region were adiabatically rotated and were maintained either parallel or antiparallel to the direction of the hydrogen beam. The coils provided a 100 mG longitudinal magnetic field at the center of the interaction

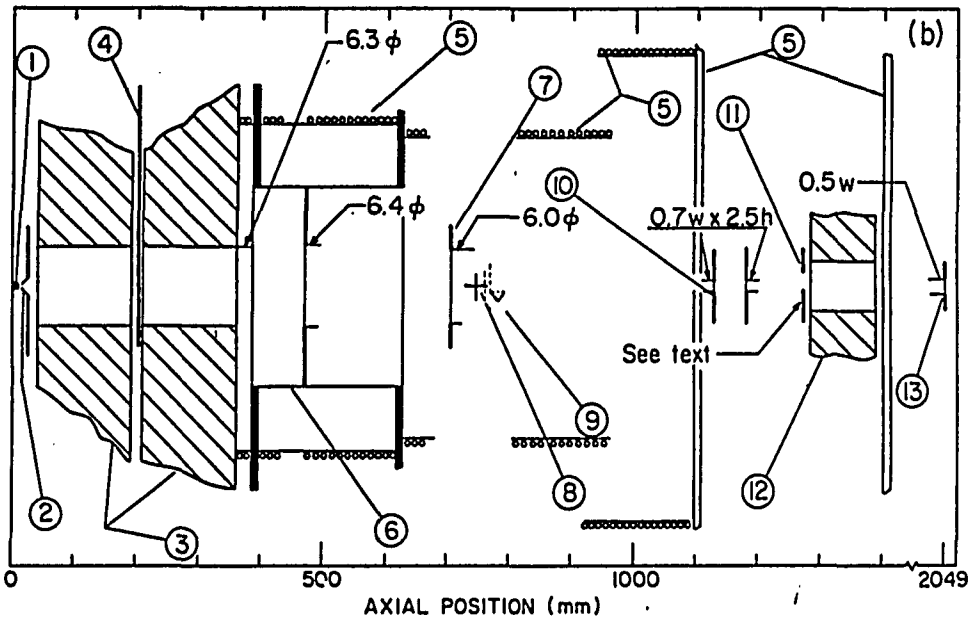

Fig. 3.4. Schematic diagram of the hydrogen beam line showing (1) nozzle, (2) skimmer, (3) hexapole magnet, (4) chopper, (5) guiding field coils, (6) tube and aperture, (7) interaction region beam collimator, (8) crossed-beam intersection point, (9) channel electron multiplier (CEM), (10) polarimeter slit, (11) Stern-Gerlach entrance aperture, (12) Stern-Gerlach magnet, and (13) QMA entrance slit. All dimensions are in mm.

region. (Originally, a weaker field was planned, but penetration of external fields through the Mu-metal shielding surrounding the interation chamber led to a ~ 20(±10) mG vertical field component. A 100 mG longitudinal field was thus required to maintain the atomic polarization as essentially longitudinal.) A circular aperture 6.0 mm in diameter and located 38 mm upstream from the center of the interaction region served to define the dimension of the beam

After leaving the interaction chamber, the atoms and molecules were detected by a quadrupole mass analyser (QMA) located about 1.4 meters downstream from the interaction region. A closed-loop helium cryopump with high pumping speed (1000 l/s for both air and hydrogen molecules) was used to minimize ion backgrounds. The QMA could be moved transversely in the horizontal plane by a motor for accurate hydrogen molecular background subtraction and polarimetry measurements. During the actual data taking, a Stern-Gerlach magnet located upstream from the QMA (as shown in Fig. 3.4) and used for the polarimetry studies, was removed from the beam line to increase the beam intensity reaching the QMA.

The determination of the hydrogen beam density, its polarization, and its dissociation fraction could not be made solely by experimental means, since these beam parameters had to be specified at the interaction region, a location at which the measurement devices could not be placed without causing severe disruption to the beam line. Therefore, three theoretical computer modeling approaches were employed:[3.1] (1) a Monte-Carlo ray-tracing analysis; (2) an approach that treated the hexapole state-selector as a thick lens; and (3) a Cartesian phase space calculation. All these techniques relied on the application of standard kinetic gas theory to establish the operating density of the source in terms of the ballast volume pressure. Method (1) provided the greatest information and the best accuracy, while the results from methods (2) and (3) provided confidence checks on those of method

(1). The reliability of the modeling results was confirmed in part by the agreement between their predictions and the empirical determination of several experimentally accessible beam quantities. For example, the measured Stern-Gerlach right-left profile asymmetries agreed to within 1% of the Monte-Carlo calculations, and the calculated average density of 9×10^{9} cm^{-3} agreed with the measured ionization yields and the gas load observation.

The density of hydrogen atoms at the interaction site as a function of the transverse radial distance from its center is shown in Fig. 3.5. Although the optical model (dash-dot line) predicts a somewhat higher density than the Monte-Carlo calculations, both methods reveal that over the 3 mm radius of the beam the variation of densities is significant. Therefore, care had to be taken to maintain consistent overlap of the electron beam (radius of 1.5 mm) and the hydrogen beam to avoid false normalization. The overall stability of the rf hydrogen source provided an exceptionally stable hydrogen beam geometry and allowed the emphasis to be placed on maintaining the electron beam characteristics which depended on both the focusing and the steering elements of the transport optics.(The experimental precautions taken to stabilize the overlap geometry will be discussed in Sect. 3.2.)

In Fig. 3.6, the polarization of the atomic hydrogen atoms at the interaction region is presented, as obtained from the Monte-Carlo computation in which the effective magnetic moment μ_{eff} of the atoms was taken as a field-dependent quan-

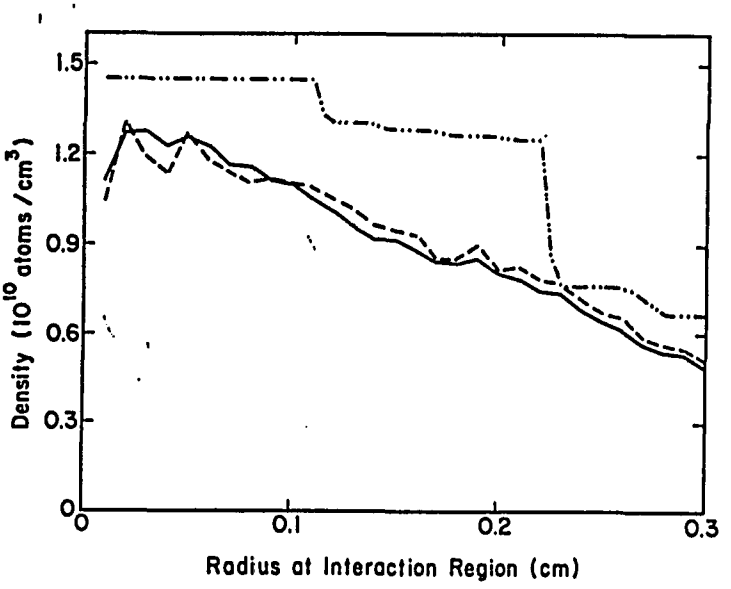

Fig. 3.5. Atomic density at the interaction region as a function of radial position. The solid and dashed lines are the results from the Monte-Carlo analysis for the field-dependent μ_{eff} and constant $\mu_{eff} = \mu_B$ respectively. Also shown is the result from the optical model (dashed line with dots).

tity. As can be seen from the figure, the maximum variation of the polarization across the beam radius in the interaction is no greater than 1%. Thus even when the electron beam is swept from the center to the edge of the atomic beam, the variation in the density-weighted atomic polarization is no more than 0.4%, which is too small to affect appreciably the asymmetry measurements presented in this thesis, given their statistical uncertainties of ±1-2 %. It should be noted for completeness that the polarization of the hydrogen beam averaged over the 3 mm radius was calculated to be 0.515(5). The reduction from the high-field value of unity is caused by the hyperfine coupling, which in the absence of the detailed transmittances of the hexapole magnet for $m_s = +\frac{1}{2}$ and $m_s = -\frac{1}{2}$ atoms would predict a value of

0.5.[3.1] At the entrance plane of the Stern-Gerlach magnet, the polarization of the atoms as a function of horizontal position from the center was also calculated. Then the left-right asymmetries of the beam after passage through the magnet were measured as a function of driving current through the magnet and compared to the Monte Carlo predictions. The measured values agreed to within ± 1% with the calculated values, lending great confidence to the accuracy of the theoretical calculations.

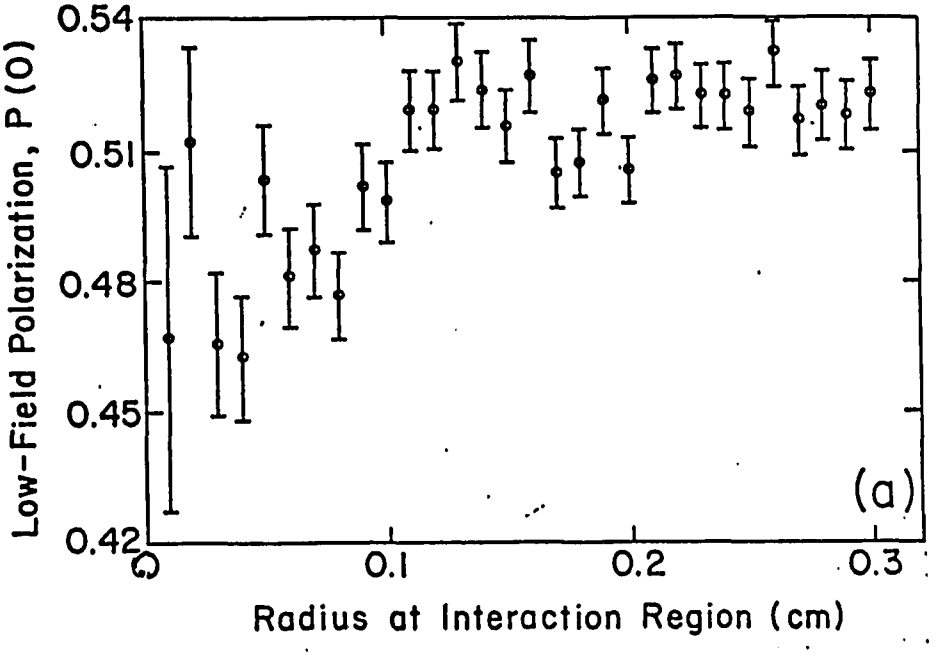

Fig. 3.6. Radial dependence of low-field polarization at the interaction region.

Although not particularly relevent to the measurements presented in this thesis, it is worthwhile noting that the dissociation fraction, F^o, of the beam leaving the source, denoted as F^0, was obtained from the relation

$$F^0 = \frac{2(R_{22} - 1)}{2R_{22} - 1)}, \tag{3.1}$$

where R_{22} is the ratio

$$R_{22} = \frac{(Q_2)^{off}}{(Q_2)^{on}}, \tag{3.2}$$

$(Q_2)^{off}$ and $(Q_2)^{on}$ being the respective mass-two readings of the QMA for the rf power in the hydrogen source off and on. The measured F^0 value was 0.831(4) under typical operating conditions. At the interaction region, the dissociation fraction was considerably higher (~ 0.95), given the selective atomic transmittance of the hexapole magnets. For the near threshold ionization measurements, however, the presence of molecules was irrelevant, since the highest energy explored was 15.27 eV, which is still below the molecular ionization threshold of 15.43 eV.

Although the interaction chamber was equipped with Mu-metal shielding that could be "de-Gaussed" *in-situ*, the residual magnetic field in the interaction site was found to be non-negligible. With the spin-guiding solenoids on, the residual field there still had three components. Along the hydrogen beam line, the magnetic field was measured to be 120(8) mG. The vertical component (parallel to the electron beam) was found to be 22(9) mG and the horizontal component, 7(7) mG. Presumably, the vertical component was large because the shielding at the top of the chamber was less than perfect. The resultant field was thus tilted with respect to the beam line by an angle θ of 10^0 corresponding to a cosine factor of 0.983 (13). When the spin guiding fields were reversed, corresponding to a reversal of the atomic spins, the measured spin-asymmetry at several energies agreed to within ±

1%. Thus it may be assumed that the cosine factor actually exceeded 0.99, which is within the uncertainty of the actual magnetic field measurements. In Table 3.1, some of the important quantities characterizing the hydrogen source are summarized.

Table 3.1 Polarized Hydrogen Beam Characteristics

Atomic polarization	0.515(5)
Density at interaction region	9×10^{9}atoms/(cm^3)
Beam Diameter	6 mm
Variation of P_H over the radius	< 0.4%
Variation of density over beam radius	~ 50%
Molecular fraction	5%
Lifetime	> 2 Years
RF Power in dissociator	14 W
Stability	Very No measurable changes

3.2 Operation and Data Acquisitions

The data acquisition procedure can be summaried as follows:

(1) Activation of the GaAs crystal (if needed).

(2) Adjustment of the hydrogen source and tuning of the electron optics.

(3) Calibration of the electron beam energy.

(4) Entry of parameters needed for computer control of data taking, such as the chopper open/close time, preset ion counts, etc.

(5) Stability check of the system.

Prior to activation, the crystal was raised under vacuum about 50 mm from its normal operating position until it faced a permanently mounted cesium dispenser (see Fig. 3.3). The first step in the activation process involved ohmic-heating of the surface with AC power. To this end, the current was increased in steps of about 0.4 A, each lasting about 5 minutes, until 1.8 A passed through the sample, and then in steps of 0.1 A, each lasting about 10 minutes, until a maximum current of 2.2 A was reached. The highest voltage across the crystal was measured to be 4 V.

A thin Chromel-Alumel thermocouple (0.125 mm in diameter) in contact with the rear surface of the crystal was used to monitor its temperature. Since the reading from the thermocouple was imprecise, due to contact problems and possible chromium diffusion in the wire, the thermocouple reading was lower than the actual crystal temperature. Visual inspection of the crystal color proved to be a very reli-

able method for determing the proper heating condition. In a dark room, at the appropriate power, the sample was dark red. If it was heated too much, its color would turn red-orange, at which point, a QMA monitor mounted on the source chamber showed that some Ga atoms had begun to escape into the vacuum at a partial pressure of ~ 10^{-9} Torr. It was found that the longer (more uniformly) the sample was heated, the higher the quantum yield would become. After approximately one hour of heating, the sample was allowed to cool for about 15 minutes, after which time the thermocouple typically read 1/6 of the maximum value obtained during heating. The time allowed for cool-down was restricted to prevent surface contamination prior to activation.

Activation proceeded with the use of the same GaAlAs diode laser employed during actual operation. The "yo-yo" method[1.17] was adopted, in which alternative layers of Cs and O_2 were applied while the emission current monitored by a positively biased collector (about 60 mm in front of the GaAs crystal) connected to an electrometer. The crystal was first slowly coated with a Cs layer from an SAES Getters dispenser mounted about 50 mm from the GaAs crystal surface and through which a current of 5.5A to 6 A was passed. The cesiator was turned off after the photocurrent had fallen to 50% of its maximum value. Oxygen gas (Matheson, Research Grade, minimum purity 99.997%) was then admitted to the chamber through a variable leak valve, the chamber pressure always being kept at 5×10^{-9} Torr

or lower. During successive applications of Cs and O_2, the oscillation amplitude in the current peak was gradually decreased, from 50% at the first few cycles to less than 10% in the last few cycles. Activation was usually stopped after approximastely 15 cycles when the total current extracted started to decrease slightly. The last cycle ended with an oxygen layer.

While the cystal was still raised in its activation position, the current through the cesiator was set to about 4.5 A, and the photocurrent was monitored on a chart-recorder. Constant monitoring and tuning of the cesiator current was needed during this period as the residual oxygen gas was pumped out of the system. After several hours, the crystal was lowered to its normal position, at which time the activation cesiator was turned off and the *in-situ* cesiator mounted in the anode was turned on. The use of low-level *in-situ* cesiation increased the life time of the crystal from 12 hours to about 400 hours. At the conclusion of the activation process, the typical quantum yield was about 2%; after 400 hours of operation it had dropped to 1/e of its initial value.

The polarized hydrogen source generally required much less attention. The cold trap on the hydrogen source chamber was filled with LN_2, and after about one hour of pumping, a base pressure of about 3×10^{-8} Torr was achieved. The 35 MHz rf power was set at 14 W, and the H_2 molecular pressure in the gas ballast connected to the discharge tube was set to 390 mTorr through the adjustment of the

heating current (about 2 A) passing through a palladium finger. Special care was taken to ensure that no air bubbles were present in the water used to cool the Pyrex discharge tube. Such bubbles, often present after the replacement of a water filter, produced instabilities in the rf power and ultimately in the hydrogen beam intensity.

A digitally controlled output voltage (DAC) from the computer system was used to select either H_1 or H_2 species for monitoring by the QMA. To minimize the effects of noise on the (low) output voltage of the DAC, a high voltage was produced and a 10:1 voltage divider was used at the input of the QMA mass selector. A program was developed to allow manual entry of numbers to select the QMA mass readings. For atomic hydrogen, this mumber ranged from 70 to 80, the variation due to the drifts in the electronics of the QMA. A number, which corresponded to the best sensitivity, or maximum mass one reading, was determined at the beginning of each data run which corresponded to the maximum mass one reading on the meter of the QMA at that time. The drift in the sensitivity of the QMA manifested itself in the data analysis, as will be discussed in Sect. 3.4.

In spite of the difficulties encounted in the intital tuning of the electron optics, as mentioned in Sect. 3.1.2, once tuned, the electron optics needed little attention. Particular care was taken to leave the elements undisturbed in order to avoid changes in the overlap between the electron and the hydrogen beams. In most cases, the complete electron optics system, including the high voltage power supply

and the voltage dividers, remained totally untouched during an entire 400-hour crystal lifetime. (Although the electron beam could be modulated by a mechanical chopper in the laser beam line, in practice, the chopper was not used since it produced instabilities in the electron beam, possibly due to the charging and discharging of a suspected "floating" element in the transport electron optics.) The electron optics control electronics was relatively sensitive to changes in the room temperature. In spite of the use of laboratory air conditioning, some very slight tuning of the output or zoom optics of the monochromator was often needed at the begining of a data run. It should be noted that if the electron beam became unstable, data taking was interrupted.

During any run, the $\frac{\lambda}{4}$ plate in the laser beam line was rotated through 4 steps, 90^0 apart, and the $\frac{\lambda}{2}$ plate was rotated through 8 steps, 45^0 apart, yielding 32 combinations in total. Regarding the spin-reversal pattern, during any specific measurement at a given energy, the $\frac{\lambda}{4}$ and $\frac{\lambda}{2}$ plates were always started from the same positions, denoted as (0,0). Then the position of the $\frac{\lambda}{2}$ plate was fixed while the $\frac{\lambda}{4}$ plate was allowed to rotate a full cycle, resulting in four spin antiparallel-parallel combinations (denoted as (n,0) where n = 0, 3), which constituted a data set. After the $\frac{\lambda}{4}$ plate returned to its original position, the $\frac{\lambda}{2}$ plate was rotated through one 45^o step and the $\frac{\lambda}{4}$ plate was again rotated through its 4-step sequence

(corresponding to (n,1) where n = 0, 3), resulting in another data set. After the $\frac{\lambda}{2}$ plate was rotated a full cycle, a complete data run was obtained. The hydrogen beam chopper was repeatedly cycled through open and close positions, each lasting one second (Since the time constant of QMA was about 300 ms, the frequency of chopper could not be increased.) After every three cycles, the accumulated ion counts for both open and closed positions were recorded, and their difference, the net number of ion counts was calculated and added to its previous value. Once the total net number of ion counts exceeded the preset value, chosen at the start of the run, one of the retardation plates would be rotated in accordance with the selected spin-reversal pattern, and the data taking procedure was repeated until all 32 orientations were completed.

The energies of the incident electron beam were chosen in a quasi-random order. At each energy, the approximate net counting rate was first determined from a manual measurement of the net ion number of counts in a given time period. The preset net number of ion counts was then determined from the product of that rate and the total time allotted for data taking at a given orientation. The time allotted was chosen to be 2-5 minutes to reduce the influence of any instabilities in the apparatus, predominantly changes in the beam overlap geometries and the drift in the QMA.

Since there were no in-line polarimeters present for this experiment, the asymmetry at the energy 15.07 eV was measured very often, 24 times in total. The consistancy among these measurements served as an indicator that there were no significant systematic changes during the data taking period. As a further check, measurements were repeated at energies 13.67, 14.62 and 15.07 eV with the spin of the hydrogen atoms reversed. Since the asymmetry displayed a minimum at 14.62 eV, 22 runs were performed at this energy, the consistency of these measurements serving as a further systematic check. In fact for both the 15.07 and 14.62 eV results, no systematic effects were observed at the level of 1%, the statistical limit of the measurements. More details about systematic effects will be presented in Sect. 3.3.

3.3 Calibration Procedure and Electron Beam Characteristics

As stated in Sect. 3.1.2, the nominal energy of the polarized electron beam was determined by the (negative) voltage applied to the crystal. Due to the work function difference between the GaAS cathode and the stainless steel interaction region enclosure, and more importantly, because of the possible energy shift of the electron beam,[3.9,3.10] the electron energy calibration had to be done very carefully.

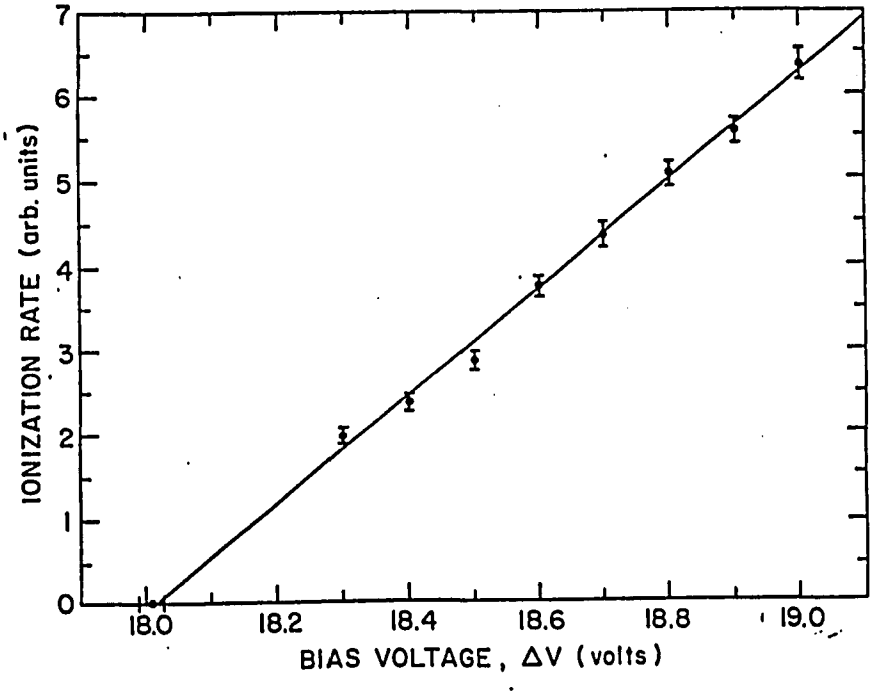

Fig. 3.7 Example of H_2 ionization energy calibration. The intercept occuring at 18.010(25) eV corresponds to an energy of 15.500(10) eV in Fig. 3.8.

To this end a purely molecular hydrogen beam was employed. With the rf power off, the characteristics of the beam depended on ballast pressure and the pressure difference between the source and the interaction chamber, both of which were

highly stable. The ionization rate for molecular hydrogen close to the ionization threshold (15.43 eV) was then measured as a function of the voltage applied to the crystal. Fig. 3.7 shows an example of such a measurement for bias voltages from -18.3 to -19.0 V, the interaction region always remaining at ground.

A linear extrapolation to zero was used to obtain an apparant threshold value which could be compared to the cross section measurements of McGowan *et al.*[3.2] As will be seen later, the electron beam was characterized by a Gaussian energy half width of 75 meV. When the ionization cross section measurements of McGowan *et al.* were convoluted with such an energy spread, the autoionization and vibrational structures disappeared, and the cross section assumed a linear form at energies between 0.3 and 1.3 eV above threshold, as shown in Fig. 3.8. Since the full-width-half-maximum (FWHM) energy spread of the data of McGowan *et al.* was 60 meV, compared to the corresponding value of 180 meV in this experiment, and since detailed knowledge of the energy profile of the electron beam used by McGowan *et al.* is absent, the data points, 10 meV per step, were convoluted directly by a Gaussian with Gaussian half width of 75 meV. The linear extrapolation to zero of the convoluted data of McGowan *et al.* yields an apparant threshold of 15.50(1) eV, which is 70 meV above the spectroscopic value. It should be noted that although the results of McGowan *et al.* were convoluted twice (once by them and once by us) to obtain the apparent threshold, the error introduced by this double

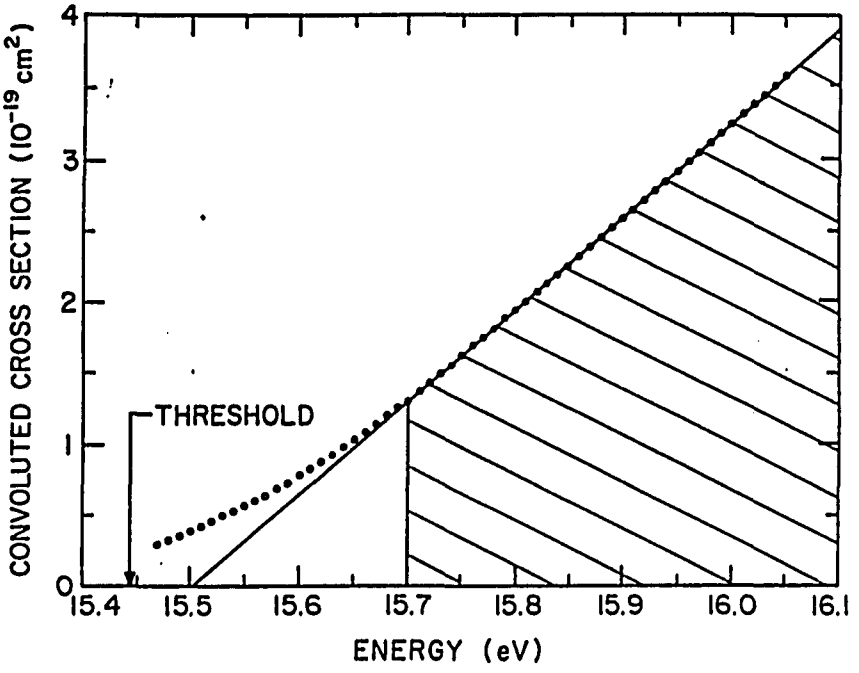

Fig. 3.8. Ionization cross section data of McGowan *et al.* for H_2 molecules convoluted with a Gaussian half width of 75 meV. The spectroscopic threshold at 15.43 eV is shown by the arrow. The linear extrapolation to an intercept of 15.50 eV is also shown

convolution is estimated to be less than 10 meV, considerably smaller than the ± 30 meV uncertainty associated with the extropolation of the calibration measurements of the present experiment. In general, the energy offset (difference between the energy calculated from the applied voltage and that obtained from the experiment) varied between 2.5 and 2.7 eV, depending on the crystal activation process and the surface contamination.

To increase the accuracy of the energy calibration, the molecular ionization measurements were also carried out under computer control. Voltages applied to the crystal were manually entered, and the data collecting time was set at 2

minutes per energy. (The preset net ion counts procedure was not adopted for reasons of efficiency and consequential stability in beam overlap.) Eight voltage settings between 18.3 to 19.0 V were selected for each of the calibrations. The net number of ion counts was recorded and normalized to the electron and hydrogen molecule signals to find the ionization rate at each energy. The eight data points so obtained were fitted to a linear function and extrapolated to zero. The uncertainty in the intercept, as calculated from the uncertainties of the linear fitting parameters, was taken as the uncertainty in the electron energy calibration. Calibrations were performed every one or two days with about two to four energy scans taken each time to ensure reproducibility.

As already noted, with the use of the *in-situ* cesiator, the lifetime (the time it takes for the current to drop to 1/e of its original value) of the GaAs crystal was increased from about 12 hours to more than 400 hours.[3.3] The extended lifetime not only increased the available time for data taking, but also permitted the energy of the electrons to be known more precisely. As shown in Fig. 3.9, the energy offset value decreased during one lifetime by as much as 50 -70 meV, occasionally even more. Equivalently, the average energy of the electron beam increased by 50-70 meV during a period of 400 hours. The decreasing trend is shown by the straight line fit in Fig. 3.9, for which a chi-square value of 0.8 was obtained for 10 degrees of freedom, corresponding to a confidence level of 77%. The associated linear

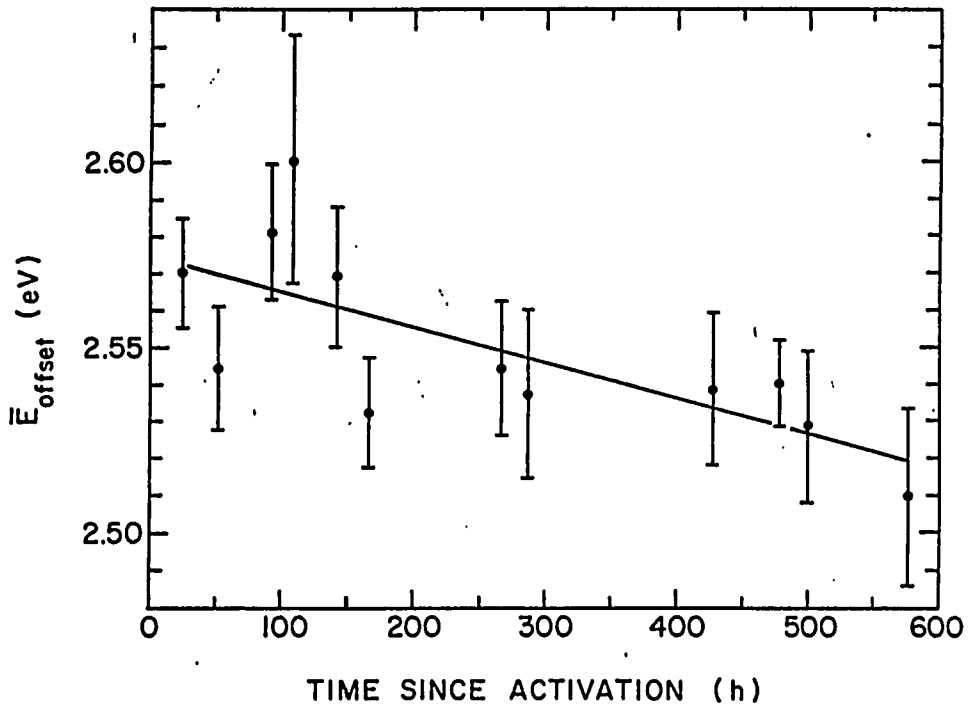

Fig. 3.9. Energy offset $\bar{E}_{offset} = e(\Delta V) - \bar{E}$ as a function of the time following a typical activation. The data points were obtained from the H_2 ionization threshold extrapolation as illustrated in Fig. 3.7. The straight line is the result of a linear fit to the data.

correlation coefficient of 0.677 corresponds to correlation probability of 97%. For searches of structure in the near threshold measurements, it is desirable for adjacent data points to differ by no more than 100 meV. Therefore, a long lifetime and a frequent energy calibration are necessary to provide maximum sensitivity.

Since a comprehensive picture of the surface chemistry of a GaAs photoemitter is not fully developed, the precise origin of the energy shift is not known. Based on present knowledge, however, we can understand the effect qualitatively with the aid of the energy level diagram depicted in Fig. 3.10. After absorbing a

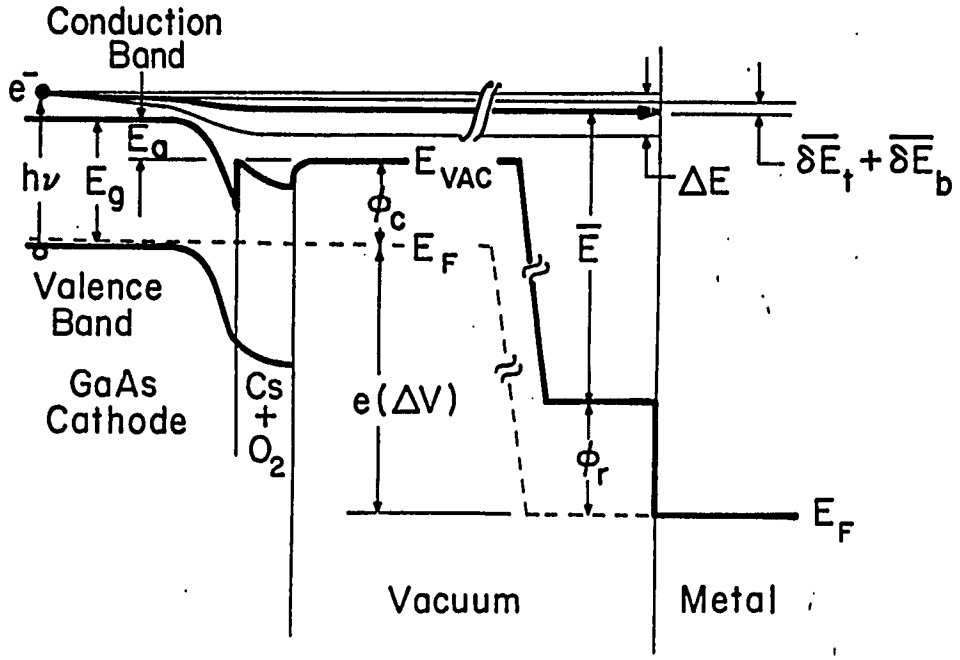

Fig. 3.10 Schematic drawing of the energy levels of the activated GaAs photoemitter. The symbols are $h\nu$ for photon excitation energy, E_g for band gap energy, E_a for effective electron affinity, ϕ_c for cathode work function, ΔV for accelerating potential, E_{VAC} for vacuum energy level, E_F for Fermi energy level, ϕ_r for work function for region of use, and $\overline{\delta E_t}$ and $\overline{\delta E_b}$ for thermalization in the bulk and energy loss in the band bending region respectively.

GaAlAs laser photon of energy 1.59 eV, a valence band electron is excited into the conduction band. Since the band gap is 1.42 eV at room temperature,[3.11] the excited electron does not lie at the bottom of the conduction band immediately after it has absorbed the photon. As it migrates to the surface, a thermalization process takes place which results in a mean energy loss δE_t of about 120 meV.[3.10] A further energy loss, $\overline{\delta E_b}$, occurs in the surface band bending region, which amounts to approximately 130 meV.[3.10] These two processes broaden the energy distribution of the beam as well as decrease its mean energy. As the electrons escape from the activated surface, the photoemitted electrons see a surface barrier, the height of

which lies below the mean energy of the electrons but above the low-energy tail. Just after activation, this barrier prevents only electrons in the extremely low-energy end of the tail from escaping from the surface. As the crystal ages, however, the barrier increases in height, cutting off more of the low energy tail as well as reducing the number of electrons emitted for a given intensity of incident light. Therefore, the mean energy of the electron beam increases as the photocurrent decreases. Quantitatively, we can express the mean energy E_e of the electron beam at the interaction region as

$$E_e = eV_c + h\nu - \delta E - \phi_r + \varepsilon(t)\,, \tag{3.6}$$

where ϕ_r is the work function of stainless steel (about 4.3 eV in the presence of hydrogen gas [3.12]), δE is the combined mean electron energy loss (250 meV) in the bulk and band-bending region, V_c is the applied voltage between the cathode and the interaction region, $h\nu$ is the photon energy (1.59 eV), and ε is a function characterizing the mean energy shift due to the aging of the crystal with time. The initial ($\varepsilon = 0$) offset value, $eV_c - E_e$, thus obtained is about 2.9 eV, which is in reasonable agreement with the observed values, considering the uncertainty in ϕ_r (±0.15 eV) and the uncertainties in $\varepsilon(t)$ at the time the initial offset measurements were made.

To characterize the energy spread of the electron beam in the interaction region, the relative ionization rate for atomic hydrogen was measured for several energies lying within 300 meV of threshold,[3.3] as shown in Fig. 3.11. With the

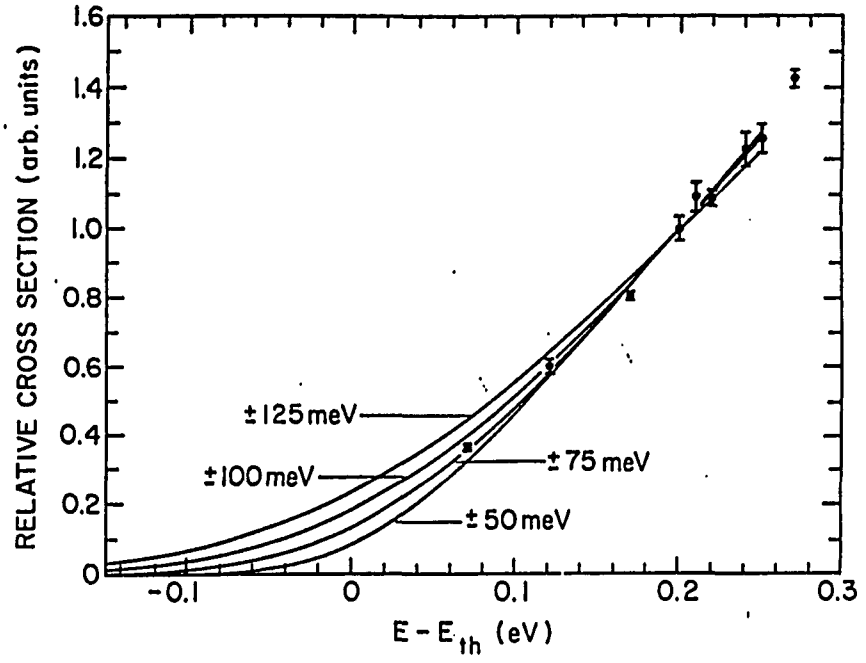

Fig. 3.11. Ionization cross section measurements for atomic hydrogen as a function of energy near threshold. The curves shown are derived from the Wannier threshold law convoluted with assumed Gaussian energy spreads. The results presented are for Gaussian half width of 50, 75, 100 and 125 meV as indicated. All curves are normalized to the data point at 13.707 eV.

energy distribution of the beam taken as a Gaussian, the Wannier threshold law $E^{1.127}$ was convoluted by a Gaussian function with a half-width varying between 50 and 125 meV. By comparing the convoluted theoretical ionization curve with the measured data points, as shown in Fig. 3.11, it was found that the best fit was obtained for a Gaussian half-width of 75 meV, corresponding to a FWHM value of 180 meV. In order to minimize systematic effects due to beam shifts, each data point was measured for a relatively short time (about 1 minute), with the results of several runs averaged and normalized to the same energy data point at 13.707 eV.

Although not crucial to the measurement of the relative asymmetries, which form the basis for this thesis, it is worthwhile noting for completeness that in the absence of an in-line electron polarimeter, the electron polarization was obtained by normalizing the asymmetries measured at higher energies to the earlier data of Fletcher *et al.*[3.13] Since the energy resolution of the earlier experiment was 2.5 eV (FWHM), compared to 180 meV in the present experiment, the measured asymmetries were convoluted by a distribution function corresponding to 2.5 eV FWHM with electron polarization P_e taken as a free parameter to optimize the fit between the two results. The polarization thus obtained was 0.27(2). The large error in P_e came largely from the uncertainty in determining the electron polarization of the earlier work by Mott scattering.[3.6] The characteristics of the polarized electron source are summarized in Table 3.2, together with some properties of the electron beam line discussed in Sect. 3.1.2.

Table 3.2 Polarized Electron Source Characteristics

Electron polarization	0.27(2)
Source life time	> 400 hours
Quantum yield	~ 2%
Current at the interaction region	150 nA
Gaussian half-width at interaction region	75 meV
Energy spread from crystal	< 230 meV FWHM
Accuracy of energy calibration	±30 meV
Beam energy shift	50 - 75 meV in 400 hrs.
Emittance	25 (mrad cm $eV^{1/4}$)
Beam diameter	~ 3 mm
Polarization reversal	Optical
Available electron energy range	0 - 1000 eV
Source vacuum	2×10^{-10} Torr

3.4 Data Reduction and Statistical Analysis

The raw data recorded by the PDP - 11 computer were transmitted via the Kermit program to the VAX 780 whenever a PDP-11 diskette was filled. The format of the data was in a matrix form with seven columns. The first column was a code containing information such as the positions of the $\frac{\lambda}{2}$ and $\frac{\lambda}{4}$ plates, the status of the rf power (on or off), the direction of the atomic polarization vector (magnetic field direction), and the QMA mass-tuning status (hydrogen molecules or atoms). For the near threshold measurements, where molecular ionization was energetically impossible, the relevant information was actually only the positions of the retardation plates and the direction of atomic polarization vector. Since the retardation plates were always started from the same initial position, the sequence of the codes in all the data files was the same. The next three colunms were digital recordings of ion, electron and hydrogen intensities respectively when the H-chopper was open. The last three were the corresponding counts when the H-chopper was closed. Each line in the data file corresponded to 3 cycles of H-chopper motion (6 seconds plus some small delay time between each chopper cycle). Only the accumulated counts were written and stored. For each orientation of the $\frac{\lambda}{2}$ and $\frac{\lambda}{4}$ plate, the number of data lines depended on the preset net number of ion counts. The data corresponding to the same orientation were grouped into "blocks," each line of the block carrying the same code number in the first column. A set of 32 data blocks,

comprising a complete file, constituted a "data run."

To generate the normalized ionization rate within each data block (orientation), the counts in each of the six columns were summed line by line, thus forming the six total quantities comprising ion open counts, denoted by *io*; electron open counts, denoted by *eo*; H_1 open counts, denoted by *qo*; and the corresponding closed counts denoted by *ic*, *ec*, and *qc*. The ionization rate for a data block was then calculated from the expression

$$R_k = \frac{[io - ic]_k}{[3(eo + ec)(qo - qc)]_k}, \tag{3.7}$$

where k is the block number (1 to 32). Fig. 3.12 shows an example of normalized ionization rates for all 32 orientations at the electron energy 14.82 eV. The higher rate data points correspond to those orientations where the electron and atomic spins were antiparallel, and the lower ones to those where the spins were parallel. It should be noted that the summation procedure averaged the random counting errors for each line. In principle, the ionization rate could have been calculated line by line. The ionization rate for a block would then have been the statistical weighted average of each line in that block and its associated uncertainty would have been the weighted combination of the uncertainties for each line. With uncertainties in the rate dominated by counting statistics, both methods yield the same result.

To guarantee the quality of the data, histograms were plotted for each run showing each of the intensities (ion, electron, and hydrogen counts) as a function

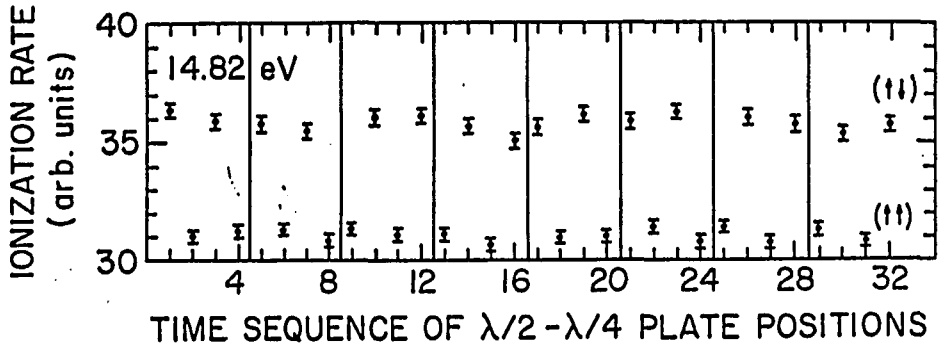

Fig. 3.12. Data acquisition binning. The 32 $(\frac{\lambda}{2},\frac{\lambda}{4})$ combinations are divided into 8 groups, each corresponding to a data set. The higher-rate data points are those for the configuration of electron and atom spins antiparallel and the lower-rate points for spins parallel, as indicated.

of time (or equivalently line number) in a given data file. The stability in any signal during one run could thus be viewed very clearly. If a sudden jump of counts for any signal was detected by eye, that line was manually deleted from the data file. If such a change lasted for many lines in a particular block (orientation), perhaps reflecting a sudden change in sensitivity of the electronics, the whole block was rejected. When any signal (usually the electron counts) displayed a great deal of jitter, a judgment had to be made. Jitter was characterized by both its amplitude and frequence, and in the case of the electron signal, data were rejected if the amplitude of jitter exceded 20% and its frequency did not correspond to a "smooth" curve over many lines of the file. It was assumed that such jitter could have been caused by

slit scraping accompanied by a loss in polarization.

At the outset of the experiment the hydrogen intensity histograms reflected substantial instabilities that were traced to DAC noise on the mass selecting signal sent to the QMA. Once the voltage divider was installed, as described in Sect. 3.2, the problem disappeared, and the hydrogen signal became stable. The data rejected during the early stages of the experiment constituted 10% of all the data ultimately obtained, while the number of data runs in that period comprised about 25% of all the data runs. For the remainder of the experiment, corresponding to 14 of the 22 weeks of data acquisition, most of the data runs reflected stable electron intensities, drift-free (<5% during 2 hours) QMA hydrogen signals, and generally the absence of sudden changes in all signals. Thus only 10% of the data obtained during the entire experiment failed to pass visual inspection of the histograms.

The 32 $\frac{\lambda}{4}$-plate and $\frac{\lambda}{2}$-plate configurations shown in Fig. 3.12 were divided into 8 data sets with each set having four configurations (corresponding to a complete rotation of the $\frac{\lambda}{2}$ plate). For each data set, denoted by i, within a given data run, denoted by j, the two rates, with spins parallel (1) or antiparallel (2), were summed, and the "real" experimental asymmetry for that set was calculated from the equation

$$(\Delta_R^i)_j = \frac{(R(\uparrow\downarrow)_1^i + R(\uparrow\downarrow)_2^i) - (R(\uparrow\uparrow)_1^i + R(\uparrow\uparrow)_2^i)}{(R(\uparrow\downarrow)_1^i + R(\uparrow\downarrow)_2^i) + (R(\uparrow\uparrow)_1^i + R(\uparrow\uparrow)_2^i)} \quad , \quad i = 1,\ldots, 8 \, , \tag{3.8}$$

where the arrows for the configurations of the spins are the same as in Chap. 1. The asymmetry for a particular run $(\Delta_R)_j$ was obtained by statistically averaging the data sets for that run, normally 8, except in cases where sets were removed by the rejection criteria discussed. On the average, there were about 7 data runs for each energy. The real asymmetry for each energy was thus obtained from the average of all the data runs, j, for that energy.

Since the ionization rate for the identical spin configuration should be the same within any data set, a non-zero difference in the rates reflects the presence of systematic effects. Two such differences, one for spins parallel and the other for spins antiparallel were formed for each data set and were then either added or subtracted to form the two "false" asymmetries, $\Delta^i_{F_+}$ and $\Delta^i_{F_-}$, according to the relation

$$(\Delta^i_{F_\pm})_j = \frac{(R(\uparrow\downarrow)^i_1 - R(\uparrow\downarrow)^i_2) \pm (R(\uparrow\uparrow)^i_1 - R(\uparrow\uparrow)^i_2)}{(R(\uparrow\downarrow)^i_1 + R(\uparrow\downarrow)^i_2) + (R(\uparrow\uparrow)^i_1 + R(\uparrow\uparrow)^i_1)} \quad , \quad i = 1,\ldots, 8 \, . \tag{3.9}$$

By definition, Δ_{F_+} is most sensitive to quasilinear drifts while Δ_{F_-} is most sensitive to quasiquadratic drifts. In order to assure the quality of the data used for the determination of the real asymmetry, a cut was applied to remove any data set for which either the "+" or the "-" false asymmetry exceeded 2.5 standard deviations from the assumed value of zero. More than 90% of the data passed this cut. (It should be noted that the application of the original noise rejection criteria occasionally required the removal of a complete data set if the noise extended throughout one complete $(\frac{\lambda}{4}, \frac{\lambda}{2})$ configuration in that data set.)

Statistically, the distribution of any measured quantity relative to its averaged value should be Gaussian, with the Gaussian half-width equalling one standard deviation. If the normalized residuals are plotted, the resulting histogram should thus be represented by a Gaussian centered at 0 and with a half-width of 1.0. Data taking extended for more than five months and resulted in more than 1300 usable data sets, among which about one quarter were taken at energies higher than 15.27 eV. While these higher energy results lie outside the domain of this thesis, the associated residuals were included in the histogramming search for non-Gaussian behavior. Normalized residuals were calculated for the "+" and "-" false asymmetries with respect to zero, and for the real asymmetries with respect to the corresponding average value at each data run. Since there is no apparent energy dependence in the false asymmetries, as seen from Fig. 3.13, and since there is no apparent orientation dependence, as seen from Fig. 3.14, all the residuals corresponding to each asymetry type, "+" false, "-" false, and real, were combined irrespective of energy and orientation. For histogramming purposes, the normalized residuals were binned in intervals of 0.2, a compromise between the number of events in each group (or the overall shape of the curve) and the resolution in spacing. (The binning error of ± 0.1 was ultimately incorporated into the final reduced chi-squares which characterized the Gaussian fits to the distributions.) In Fig. 3.15, the residuals (solid histograms) are denoted by $(x^i)_j$, and the number of residuals

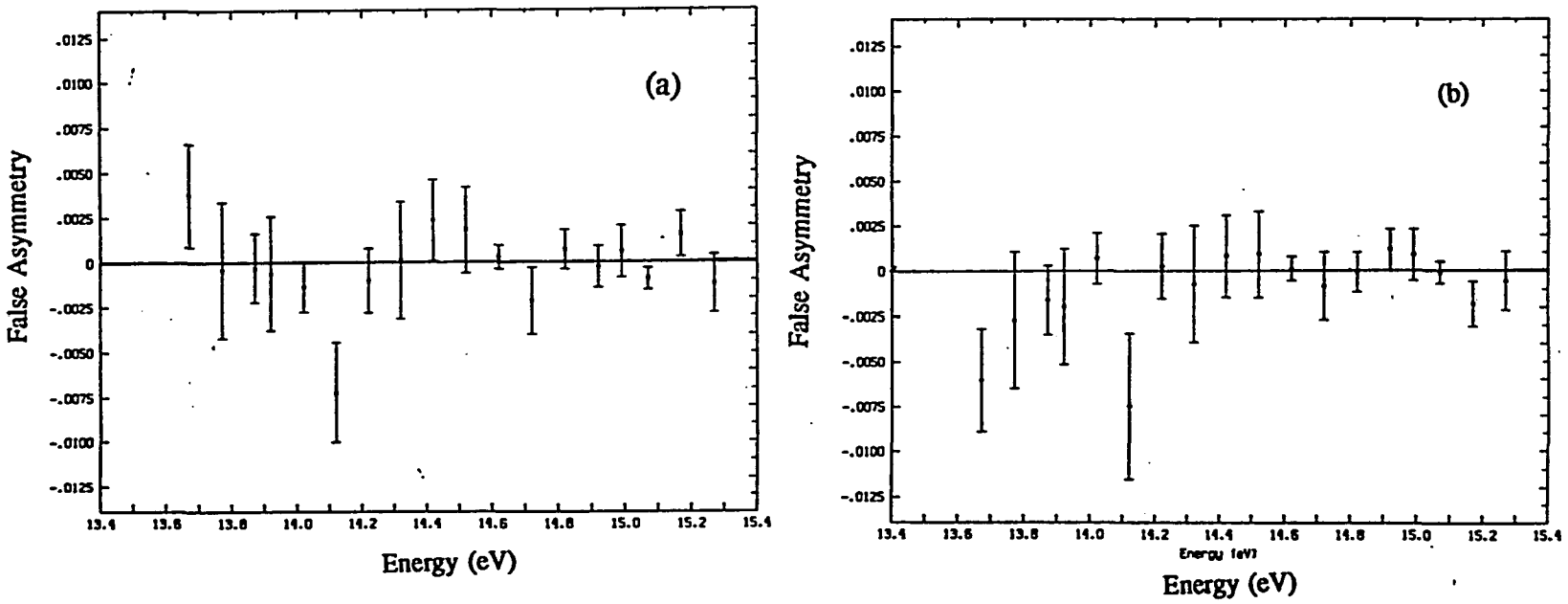

Fig. 3.13 False asymmetries vs. incident electron energy showing the sum of all "+" false asymmetries in (a) and the sum of all the "-" false asymmetries in (b).

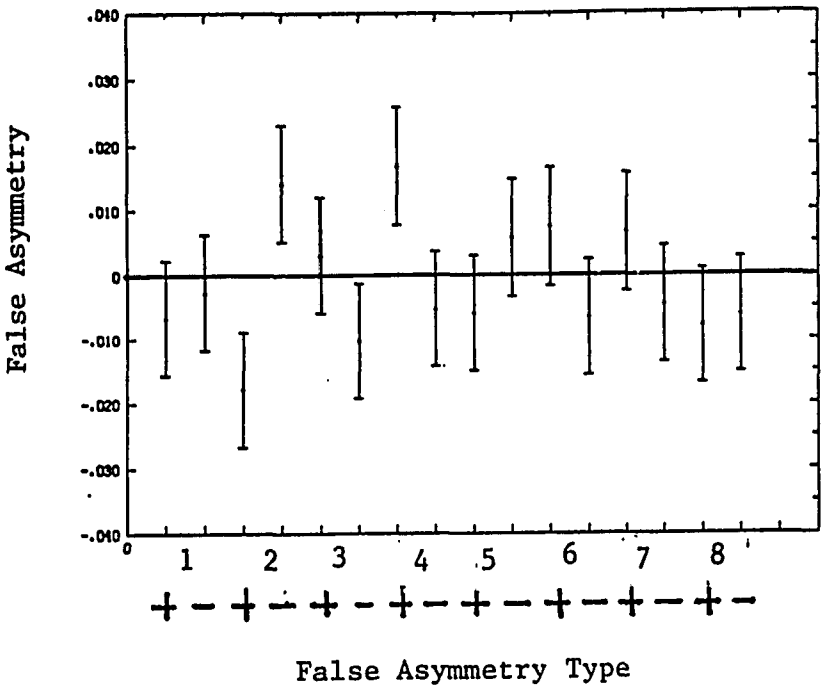

Fig. 3.14. Summary of false asymmetries for all data runs at incident electron energy of 13.92 eV.

(frequency) falling within $(x^i)_j \pm 0.1$ is plotted on the vertical axis. Visual inspection suggests that all three histograms have an approximate Gaussian appearance centered at zero with tails terminating at about 5 standard deviations. (It should be noted that without the application of the original noise rejection criteria, the histograms would have very long tails extending to more than 10 standard deviations and would lose their Gaussian character.)

From a quantitative analysis it was found that all three histograms were represented very well by the sum of two Gaussian distributions, shown in Fig. 3.15, as solid lines. In each case, one Gaussian, labeled (1) in Fig. 3.15 and having a

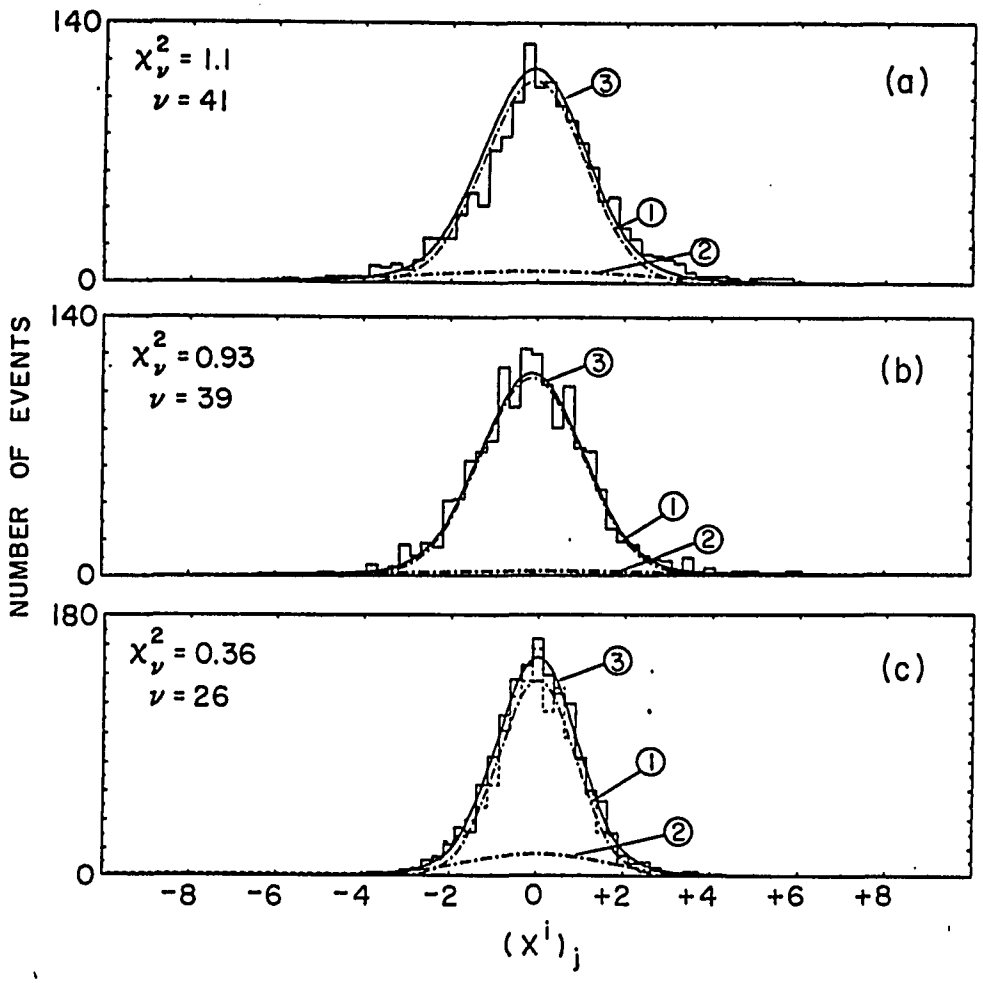

Fig. 3.15. Analysis of statistical errors showing (a) histogram of normalized false asymmetries, $(x^i)_j=(\Delta^i_{F_+})_j / (\sigma^i_{F_+})_j$, for all data sets i and all runs j, irrespective of energy and $(\frac{\lambda}{2},\frac{\lambda}{4})$ orientations, where $(\sigma^i_{F_+})_j$ is the statistical uncertainty for false asymetry $(\Delta^i_{F_+})_j$, (b) histogram analogous to that in (a) for (Δ_{F_-}) false asymmetries, (c) histogram (solid) of normalized real-asymmetry residuals, $(x^i)_j= [(\Delta_k)_j - (\bar{\Delta}_R)_j]/ (\sigma^i_R)_j$, where $(\bar{\Delta}_R)_j$ is the weighted mean of the real asymmetry for the j-th data run, and histogram (dashed) of real asymmetry rsidauls for truncated data set as explained in the text. In each case the curve labeled 3 is obtained from a fit of the data by the sum of two Gaussian labeled 1 and 2.

slightly narrower width than the original distribution, dominates, while the other, labeled (2) in Fig. 3.15 and having a much broader width, contributes at much smaller level. The former represents "drift free" operation while the latter represents "drift hindered" operation. By comparing the height of the broader distribution for the two false asymmetry curves, it is clear that when drifts occured, quasilinear drifts ("+" false asymmetry) were more prevalent than quasiquadratic drifts ("-" false asymmetry). One possible explanation is that the mass tune of the QMA occasionally drifted, and empirically, it was found that this drift was largely quasilinear. Drifts might also have been caused by changes in beam overlap or changes in the sensitivities of the electronics, both of which apparently were determined by quasilinear effects, at least on the time scale of data set. By construction, the real asymmetries are contaminated by both types of drifts. Thus in Fig. 3.15 the broad distribution is greater in height for the real asymmetry than it is for either of the false asymmetries.

The presence of the broad distribution, albeit at a relatively low level, gives impetus to the application of the false asymmetry cut at 2.5 standard deviations. It is clear that such a precaution was necessary, since although the presence of the broad distribution had a small effect on the histogram of the data in aggregate, it could have had a potentially significant effect on the data for any one particular energy. Limited data sets precluded the search for such an effect at each energy.

The 2.5-sigma cut on the false asymmetries removed only 3% of the data from the narrower distribution, but 35% of the data from the broader one. Since the central region of the two distributions cannot be separated, however, the presence of the broad Gaussian effectively increases the uncertainty of the measurements, as can be seen from the following analysis, which takes into account the 2.5-sigma truncation. The distribution represented by the sum of the two Gaussians can be expressed as

$$y = y_1 e^{-\frac{x^2}{2\sigma_1^2}} + y_2 e^{-\frac{x^2}{2\sigma_2^2}}, \tag{3.10}$$

where y_1 and y_2 are the heights of the individaul Gaussians, and σ_1 and σ_2 are the corresponding widths. The variance, $(\sigma^*)^2$, of the combined distribution is then calculated to be

$$(\sigma^*)^2 = \frac{y_1\sigma_1^3\left[A_G(z_1) - z_1(\frac{2}{\pi})^{1/2}e^{-\frac{1}{2}z_1^2}\right] + y_2\sigma_2^3\left[A_G(z_2) - z_2(\frac{2}{\pi})^{1/2}e^{-\frac{1}{2}z_2^2}\right]}{y_1\sigma_1 A_G(z_1) + y_2\sigma_2 A_G(z_2)}, \tag{3.11}$$

where A_G is the normal error distribution function with arguments z_1 and z_2 which are defined by

$$z_1 = \frac{z}{\sigma_1} \quad \text{and} \quad z_2 = \frac{z}{\sigma_2}, \tag{3.12}$$

with $\pm z$ being the truncation points of the distribution. For the "+" and "-" false asymmetries remaining after the application of the 2.5 sigma cut, the combined standard deviations were calculated in accordance with Eq. (3.12). It was found from this procedure that the uncertainties for the false asymmtries, calculated solely

on the basis of counting statistics, must be increased by a factor of 1.08 in order to take into account the effect of drifts.

The effect on the histogram of the real asymmetries produced by the 2.5-sigma cut on the false asymmetries is illustrated by the dashed histogram in Fig. 3.15(c). Close inspection shows a slight narrowing in the distribution and no change of the centroid to within the binning accuracy of ± 0.1 standard deviations. This consistancy provides great confidence in the unbiased effect of the application of the 2.5-sigma false asymmetry cuts. Since the resulting real asymmetry distribution (dashed histogram) is no longer expected to be Gaussian, however, a variance must be calculated directly from the (dashed) histogram with Poisson statistics for the frequency (y axis). The resulting value of 1.10, obtained in this manner for the variance, would correspond to a standard deviation of 1.05 for a normal distribution. However, since the distribution is not Gaussian, prudence dictates that the accepted standard deviation be increased slightly and to this end a value of 1.07 was used. (The increase also took into account the ± 0.1 binning error.) The uncertainties for the real asymmetries calculated solely on the basis of counting statistics thus had to be increased by a factor of 1.07.

The false asymmetry summaries for the truncated data are shown in Fig. 3.16, demonstrating to extremely high confidence the absence of systematic effects. The consistency of the false asymmetries with zero is further demonstrated by the

respective x_ν^2 values of 1.04 and 0.96 with respect to zero for ν = 1048 degrees of freedom. Taken as a group, the "+" false asymmetries average to $+32(24)\times10^{-5}$ and the "-" false asymmetries average to $-57(24)\times10^{-5}$. Therefore, the truncated data may be assumed to be free from systematic effects at the level of approximately $\pm5\times10^{-4}$. For an average real spin asymmetry of 0.07, systematic effects are thus suppressed to below 1%.

The stability of the experiment is illustrated by the results for the real asymmetries at the energy 15.07 eV. As shown by Fig. 3.17, all the measurements are consistent with each other, the reduced chi-square about their average being given by x_ν^2 = 1.08 for ν = 23 degrees of freedom which corresponds to a confidence level of 37%. For the 15.07 eV data point, the average value of the asymmetry obtained from the 24 runs shown in Fig. 3.17 is 0.683(6), corresponding to a fractional standard uncertainty of ± 1%, about the same level as the limit on the systematic uncertainty.

In order to handle the large number of data sets included in the analysis, a series of computer programs were developed to make the computation easy and error free. The data reduction program which handled the raw data files described at the beginning of this section, produced files containing the "+" and "-" false asymmetries and the real asymmetries, as well as the corresponding standard deviations for the eight data sets in a given run. These files were labeled according to the for-

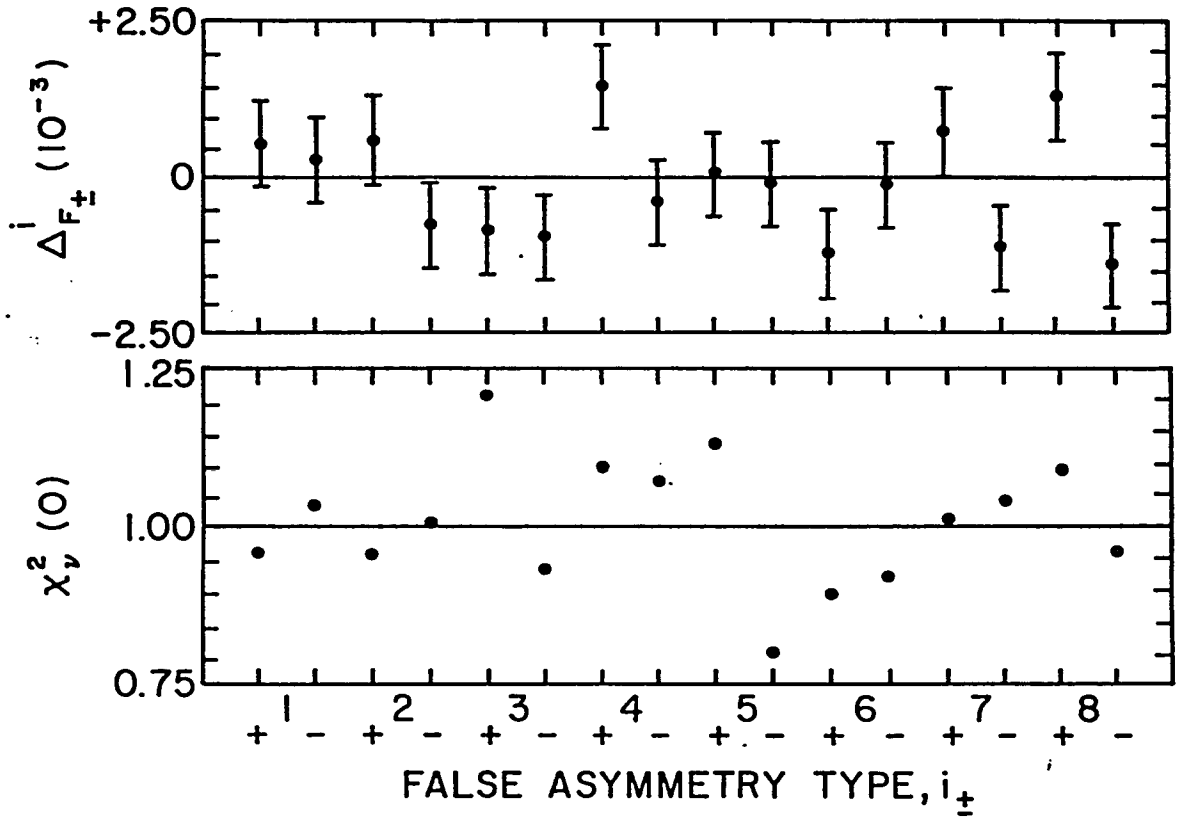

Fig. 3.16. (a) Summary of the sixteen false asymmetries ($\Delta^{i}_{F_{\pm}}$), each averaged over all runs irrespective of energy. (b) Corresponding set of reduced chi-square $\chi^2_\nu(0)$ for assumed average of zero. The number of degrees of freedom ν varies between 143 and 159.

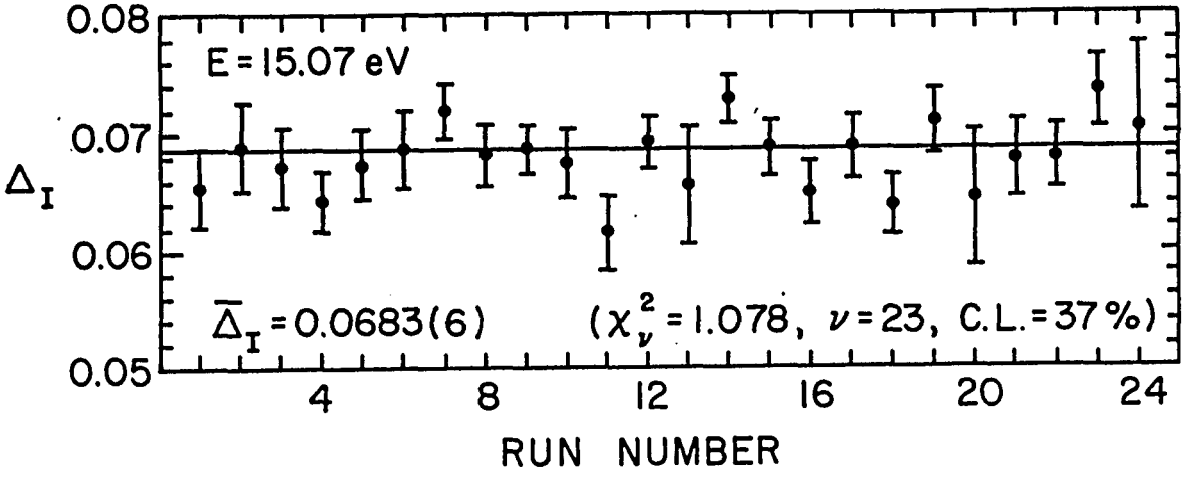

Fig. 3.17. Stability check showing 24 separate measurements of real asymmetry Δ_I at 15.07 eV.

mat xxxxx.f0y and xxxxx.D0y, where the five digits x indicated the date the data were taken, y indicated the file number on that date, and "f" and "D" signified respectively false (both "+" and "-") and real asymmetries. The first cuts based upon the noise criteria were carried out on these files manually, after which some files contained fewer than 8 data sets. An additional file was created which contained only the labels of the f and D files, and a subroutine paired each of the f and D files with the electron energy to which it corresponded. To generate the histograms, a program read information from the "f" and "D" files and calculated the normalized residuals. A subroutine then scanned the f files and flagged the data sets within each file which failed the 2.5-sigma cut. Another subroutine, which calculated the real asymmetry, searched for these flags and skipped the corresponding

data set in the "D" file. Once the asymmetries (both real and false) and their normalized residauls were calculated, the results were stored in appropriate output files. Also contained in the output files were chi-square values calculated for the asymmetries obtained at each energy, and in the case of the false asymmetries, at each orientation. The information in the output files was used by a plotting subroutine for the presentation of the results in a variety of displays.

3.5 Rydberg Contribution and Photon Contamination

The ionization cross section is very small close to threshold, while the cross section for excitation to high quantum states (Rydberg states) can be quite appreciable. Thus electric field ionization of Rydberg atoms has to be examined carefully. The electric field strength needed to field ionize a Rydberg atom with principle quatum number n is given by[3.15]

$$F = \frac{5.14x10^9}{(9n^4)} \text{ (V/cm)} . \tag{3.13}$$

Since the interaction region is well shielded electrostatically, only the electric field produced in the vicinity of the ion detector need be considered. As stated before, the voltage applied to the grid in front of the CEM ion detector was -650 V. Since the distance between the grid and the wall of the mesh was about 3 cm, the electric field in the interaction region was about 200 V/cm. At such a field strength, only Rydberg states with n greater than 40 could be field ionized according to Eq. (3.13), which is about 8 meV below the ionization threshold.

The cross sections for excitation to high lying states of atomic hydrogen have not been calculated very well and no experimental results are available. If the first Born approximation is applied, for example, the excitation cross sections for $n \gg 1$ follow a scaling law given by [3.16]

$$\sigma_n = \frac{\sigma_o(E_i)}{n^3} , \tag{3.14}$$

where

$$\sigma_o = \left(\frac{2^{11}\pi}{3k_o^2}\right)\int_{q_2}^{q_1} \frac{1+3q^2}{q(1+q^2)^6}\, dq\ , \tag{3.15a}$$

the limits on the integral being

$$q_1 = k_o - \sqrt{(k_o^2 - 1)}$$
$$q_2 = k_o + \sqrt{(k_o^2 - 1)} \tag{3.15b}$$

with $E_i = \frac{1}{2}k_o^2$ the incident electron energy. In the present problem, only contributions from states with $n \geq 40$ need to be taken into account. The total excitation cross section σ_R, which is the summation (actually replaced by an integral) of the excitation cross sections for Rydberg states of quantum number $n = 40$ to $n = \infty$, is proportional to n^{-2} :

$$\sigma_R = \sigma_o(E_i)/2n^2\ , \tag{3.16}$$

where σ_o is calculated from Eq (3.15a). According to this analysis, however, as E_i approaches 1/2 (13.6 eV); that is, the ionization threshold, Eq. (3.15a) predicts that σ_o approaches zero, a result that does not appear to agree with reality. In fact, the excitation cross sections for the low lying states are rather smooth functions in the ionization threshold region. A similiar behavior should hold for higher states.[3.17]–[3.19]

We must therefore adopt an alternate approach. Since the n^{-3} scaling law is considered to be a good approximation when n is large,[3.19] we apply it and use the calculated Born cross section of Omidvar[3.17] for E_i = 1/2 and n = 10. This is the

only available quantum mechanical calculation for $n > 5$. Using Omidvar's value of $0.001\pi a_o^2$ (a_0 being the Bohr radius) for n = 10 at E_i = 13.6 eV, we find with the use of Eq. (3.12) that σ_0 at 13.6 eV is $1.0\pi a_o^2$. For the energy range of interest in this discussion, within 0.5 eV of the ionization threshold, we can take σ_o to be a constant, assuming the excitation cross sections are rather smooth over this narrow energy region. The total excitation cross section is then given by

$$\sigma_R = 3x10^{-4}\pi a_o^2 , \tag{3.17}$$

in accordance with Eq. (3.16).

Now from the experimental work of McGowen *et al.*,[1.32] the ionization cross section for atomic hydrogen within 0.5 eV of threshold can be written as

$$\sigma_e = 0.08(\pi a_o^2)E^{1.127} , \tag{3.18}$$

where E is the excess energy expressed in eV. Then at the lowest incident energy investigated above threshold (E_i = 13.67 eV, or E = 73 meV) application of Eq. (3.18) with an assumed Gaussian distribution for the electron beam of half-width of 75 meV yields a convoluted ionization cross section of $4.7\times10^{-3}\pi a_0^2$. By contrast, for Rydberg field ionization, Eq. (3.17) yields a convoluted cross section of $2.5\times10^{-4}\pi a_o^2$. Thus the relative contribution of Rydberg atoms to the total cross section (ionization cross section plus field ionization contribution) is only 5% at an electron energy 13.67 eV, assuming equal detection efficiencies for both processes.

From the experimental results shown in Fig. 3.11, where the ionization cross

section near threshold is observed to follow the Wannier threshold law approximately, the maximum Rydberg contribution is estimated to be no more than 5% of the total events at 13.67 eV, in agreement with previous calculations. In fact, the actual Rydberg contribution is probably smaller than 5%. First, from geometric considerations, the capture probability of the CEM detector may be slightly smaller for field-stripped Rydberg atoms than it is for thermal ions leaving the interaction region. Second, the calculated excitation cross sections of Omidvar for low lying excited states (n = 2, 3) are about 50% higher than the experimental results.[3.20] Thus, the 5% Rydberg contribution at 13.67 eV should be regarded as a generous upper limit.

As the electron energy increases, the ionization cross section grows faster than the excitation cross section, as a consequence of which Rydberg contamination becomes progressively less of a problem. For example, at the next highest energy investigated, E_i = 13.77 eV, the convoluted ionization cross section is $1.1\times10^{-2}\pi a_o^2$, which corresponds to a value of $3\times10^{-4}\pi a_o^2$ for the Rydberg cross section. (Note that at this data point, a small part of the tail in the energy distribution curve still lies below the excitation thrershold of 13.597 eV.) The relative contribution of Rydberg states at 13.77 eV thus has an upper limit of 3%. At energies of 13.87 eV, 13.92 eV and 14.02 eV, the maximum Rydberg contributions are 1.6%, 1% and 0.2% respectively. By contrast, at the lowest energy point measured, a centroid value of

13.57 eV, the contribution can be as large as 10%.

The preceding discussion has only considered the influence of Rydberg contributions on the measured rate. What is the influence of Rydberg atoms on the spin asymmetry? To first order, the combined spin asymmetry, A_c, containing both ionization and Rydberg contributions, can be expressed as

$$A_c = A_I\,(1-\beta) + A_R\beta\,, \tag{3.19}$$

where A_I is the spin asymmetry due to ionization only, and A_R is the asymmetry due to Rydberg atoms only. The parameter β is the ratio of the Rydberg field ionization cross section (sum of of the excitation cross sections for $n \geq 40$) to the electron impact ionization cross section at any given energy. For a Rydberg atom with quantum number $n \geq 40$, the spin asymmetry may be expected to be somewhat greater than zero since as $n \rightarrow \infty$ the Rydberg asymmetry approaches the ionization asymmetry. In Table 3.3, the Rydberg-corrections, β, to the ionization rate are tabulated together with the Rydberg corrected asymmetries, Δ_f^0 and Δ_f^1, for assumed Rydberg asymmetries, A_R, equal to zero and -1/3 respectively. The latter being the lower bound in accordance with Eq. (3.19).

Another possible source of contamination of the measured signal might have been the detection of Lyman-α photons[3.21] originating either from the quenching of excited 2S metastable atoms by the electric field near the CEM or from the hydrogen source itself. In order to investigate the size of the 2S quenching contribution,

Table 3.3 Spin Asymmetries with Rydberg Corrections

Energy (eV)	Δ_f^e (experimental)	Δ_f^{c0} ($A_R = 0$)	Δ_f^{c1} ($A_R = -1/30$)	β (%)
13.57	0.024(16)	0.027	0.032	10
13.67	0.0598(32)	0.0629	0.0654	5
13.77	0.0703(50)	0.0724	0.0739	3
13.87	0.0612(22)	0.0620	0.0629	1.6
13.92	0.0620(32)	0.0626	0.0631	1
14.02	0.0687(14)	0.0687	0.0687	0.3
14.07	0.0659(45)	0.0659	0.0659	~ 0.
14.12	0.0710(39)	0.0710	0.0710	~ 0.

the electron energy was adjusted to a value between 10.2 eV (the threshold of 2S excitation) and 13.6 eV. The bias voltages on the cone and the grid were then scanned over a 1 kV range and the signals from the CEM were recorded. The recorded counts were all consistent with zero within the statistics appropriate to the experiment (< 0.1 count/s). The size of the contribution from the hydrogen source itself was examined by turning off the electron beam and again scanning the cone and grid voltage. No measurable signal was found.

It should also be noted that at the outset of the experiment, a pair of quench plates was installed immediately downstream from the nozzle of the rf discharge tube to test for 2S contamination of the effusing beam. When voltages were applied

to the plates to produce an electrostatic quenching field, no change in the CEM signal was discernable, whether the test was conducted with the electron beam on or off. Thus it may be concluded that the hydrogen beam was free of 2S contamination at the level of experimental interest. For completeness, we also point out that there was no evidence of hydrogen molecule comtamination even at the highest energy point (15.27 eV), since the event rate was much less than 1 count per second when the rf was off, as contrasted with 1000 counts per second when the rf was on.

Chapter 4. Experimental Results and Discussions

The experimental results of the spin-asymmetry measurements for atomic hydrogen in the near threshold region, extending from 13.57 to 15.27 eV, will be presented in Sect. 4.1.1 of this chapter. Detailed comparisions will be made with the predictions of the Wannier threshold law in Sect. 4.1.2 and with the Coulomb-dipole theory in Sect. 4.1.3, both of which will be seen to inadequately represent the measured asymmetries. In Sect. 4.2 some previous experimental results, which had been interpreted as supporting the Wannier theory, will be examined and will be shown to deviate from the Wannier predictions based upon rigorous statistical tests of the published data. In this section a comparison will also be made with the results of spin-asymmetry measurements of alkali atoms. Finally, in Sect. 4.3 an attempt will be made to elucidate the failure of the Wannier theory to predict the results of the hydrogen spin asymmetry results.

4.1 Spin-dependent Asymmetries for Atomic Hydrogen

4.1.1 Experimental Results

Table 4.1 summarizes the real asymmetries which are the principal results of hydrogen experiment. As can be seen there are 24 data points for incident electron energies between 13.57 eV and 15.27 eV. The energy separation between data points varies from 50 meV to 100 meV. In order to place the results on an absolute scale, the physical asymmtries, A(E), were calculated from the experimental asymmetries $\Delta_I(E)$ according to the relation

$$A_I = \frac{\Delta_I}{P_e P_H \cos(\theta)} , \tag{4.1}$$

where the electron polarization P_e was taken as 0.27(2), the atomic hydrogen polarization P_H was taken as 0.515(5), and the cosine of the angle between the electron and hydrogen polarization vectors, was taken as 0.99(1). The large uncertainties in A_I are dominated by the uncertainty in the electron polarization (± 7.4%).

For purposes of comparision with threshold laws, however, it is the relative asymmetries, listed under the heading Δ_I in the third column of Table 4.1, that are significant. The statistical quality of the relative asymmetry measurements is reflected by the reduced chi-square values, χ^2_ν, and degrees of freedom, ν, for the Δ_I results at each energy, each data set having been treated as an independent measurement. The last column presents the statistical confidence level for the reduced chi-square values, 50% being the expected average value. Although the limited set of

Table 4.1 Spin Asymmetries from 13.57 eV to 15.27 eV

Energy(eV)	A_1	Δ_1	χ^2_ν	ν	CL(%)
13.57	0.17(12)	0.024(16)	0.937	23	55
13.67	0.434(40)	0.0598(32)	0.744	141	99
13.77	0.511(53)	0.0703(50)	0.587	13	88
13.87	0.445(37)	0.0612(22)	0.862	54	75
13.92	0.450(41)	0.0620(32)	1.291	7	25
14.02	0.499(39)	0.0687(14)	1.263	25	17
14.07	0.479(49)	0.0659(45)	0.209	4	96
14.12	0.516(48)	0.0710(39)		0	
14.22	0.505(39)	0.0695(14)	0.939	14	52
14.27	0.446(52)	0.0661(54)	0.616	7	76
14.32	0.540(45)	0.0743(25)	1.859	6	8
14.42	0.530(41)	0.0729(15)	1.354	8	30
14.47	0.474(55)	0.0623(57)	0.654	5	69
14.52	0.469(37)	0.0645(15)	1.403	28	8
14.57	0.500(46)	0.0698(37)	0.996	16	46
14.62	0.480(36)	0.06607(61)	0.889	140	82
14.67	0.479(45)	0.0660(37)	0.236	7	98
14.72	0.478(38)	0.0658(16)	1.139	11	32
14.82	0.530(41)	0.0730(11)	0.581	21	94
14.92	0.528(41)	0.0727(11)	0.796	18	72
14.99	0.522(40)	0.0719(12)	1.305	23	14
15.07	0.496(38)	0.06826(54)	1.103	127	20
15.17	0.511(39)	0.0703(12)	1.023	43	43
15.27	0.502(39)	0.0691(15)	0.310	9	98

24 data points makes it impossible to check in detail the distribution of the χ^2_ν values, a visual inspection suggests that they are reasonably distributed. For example, there are 13 χ^2_ν values with a confidence level (CL) greater than 50% and 10 χ^2_ν

values with a CL less than 50%, the data point at 14.12 eV having been excluded since it represents the measurement of only one data set. Such a grouping of CL's is consistant with the statistical meaning of the chi-square value, and demonstrates that the statistical uncertainties calculated for the real asymmetries are appropriate. In another words, if the uncertainties were too large, most of the 23 χ_ν^2 values would correspond to CL's greater than 50%; if they were too small, or if they were plagued by systematic effects, they would correspond to CL's smaller than 50%.

Fig. 4.1 displays graphically 20 of the experimental data points listed in Table 4.1. Four of the data points, all having rather large error bars compared to those of their neighbors and all in agreement with them, have been omitted for clarity of presentation. (Their statistical significance is so small that their inclusion barely affects the remaining analysis.) The horizontal error bars shown for each data point in the figure represent the uncertainty in the calibration of the incident electron energies (±30 meV). At 13.57 eV, the heavy outer error bar illustrates the Gaussian energy width of ± 75 meV characterizing the electron beam. It should be noted that the real asymmetries calculated without the 2.5 standard deviation false asymmetry cut differ from those shown by a very small fraction of a standard deviation and are visually almost indistinquishable.

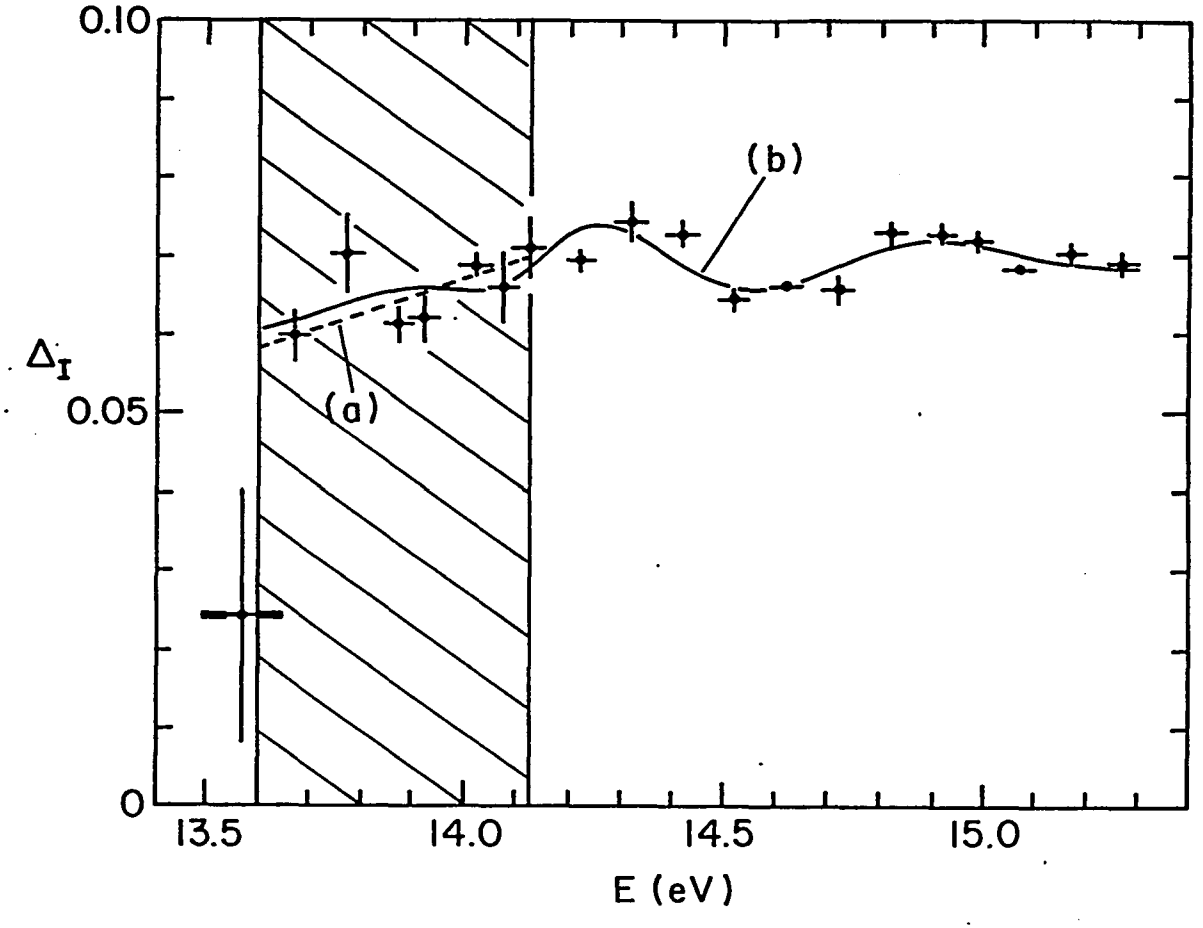

Fig. 4.1. Measured real asymmetries Δ_I (cf. Table 4.1) for incident electron energies between 13.57 and 15.27 eV. The vertical and horizontal error bars represent one-standard-deviation uncertainties. The heavy, outer error bar on the 13.57-eV point illustrates the characteristic energy spread of the electron beam. Curve (a) is a linear fit in the restricted (hatched) region while curve (b) is an example of a fit (see text) of the Coulomb dipole theory

4.1.2 Comparision with the Wannier Theory

In Sect. 2.1, we saw that the Wannier theory predicts that the ionization spin-asymmetry should be constant in the vicinity of threshold, if contributions from the suppressed states ($E^{3.381}$ or $E^{3.881}$) can be neglected. Over the full region investigated (13.67 - 15.27 eV), the experimental results shown in Fig. 4.1 are clearly not consistent with a constant function. Even allowing for a possible slope with a linear fit we find a very poor reduced chi-square value, χ^2_ν, of 4.82 for $\nu = 17$ degrees of freedom, corresponding to an exceedingly low confidence level of 5×10^{-10}. (Note that for all the functional fits, we used the final fitted function to convert the horizontal error bars into vertical errors which we added in quadrature with the vertical uncertainties shown in figures. The quoted χ^2_ν values, somewhat smaller than those that would otherwise be obtained, reflect this procedure.) The presence of structure is thus evident.

Let us now concentrate on the energy range from 0 to 0.5 eV above the ionization threshold (hatched region in Fig. 4.1) where the Wannier theory was found to be valid by McGowan *et al.*[1.32] from the total ionization cross section measurements for H atoms. When a constant function is fitted from 13.57 to 14.12 eV, the resulting chi-square is $\chi^2_\nu = 2.84$ for $\nu = 7$ degrees of freedom, corresponding to a confidence level of 0.76%. If the 13.57 data point is removed, the result is $\chi^2_\nu = 2.32$ for $\nu = 6$, corresponding to a confidence level of 3%. The Wannier prediction

of a constant function is thus clearly violated. Although the energy spread of ± 30 meV precludes a search for structure in this region, the general trend of the 6 data points from 13.67 to 14.12 eV can be investigated. In fact, these data points are well characterized by a linear function that increases with energy. The result of a linear fit is given by

$$\Delta_I = 0.059 + 0.0225\, E\ , \tag{4.2}$$

where E is in eV, and the uncertainties in both parameters are approximately 50%. The χ^2_ν value is 0.78 for $\nu = 5$, corresponding to a confidence level of 56%. The conclusion that the spin-asymmetry decreases as the ionization threshold is approached from above is further substantiated by the 13.57 eV data point which has a value more than 2 standard deviations lower than the asymmetry at 13.67 eV.

We now turn to a discussion of the contribution of the field-ionized Rydberg atoms, which has major effect very close to threshold, as we noted in Sect. 3.5. Specifically we wish to see whether the Rydberg contributions can reduce the positive slope in the hatched region to the point where it is consistent with a constant function. To this end, when we apply Eq. (3.19) we use the lower bound of -1/3 for the spin-asymmetry of Rydberg atoms. (The upper bound of +1 would have the effect of enhancing the positive slope already found from the linear fit.) The resulting corrected spin asymmetries, Δ_f^1 are tabulated in the fourth column of Table 3.3. Using these values, which provide the greatest possible shift in the slope, we find

that the fit of a constant function from 13.57 to 14.12 eV results in a χ_ν^2 value of 1.89 for $\nu = 7$ corresponding to a CL value of 7%. By comparision, the result for an assumed Rydberg asymmetry, A_R, of zero (Δ_f^0 in the third column of Table 3.3) is $\chi_\nu^2 = 2.384$ for $\nu = 7$, corresponding to a CL level of 2%. (It should be noted that with the correction having been made for the Rydberg contribution, there is no longer any justification for eliminating the 13.57 eV data point.) Thus, even in the "worst" case (A_R = -1/3), the constant fit is still very poor. It should be reemphasized that the Rydberg contribution may not affect the experimental data even to the extent assumed if the excitation cross sections are actually lower than those given by Eq. (3.16), as we have already suggested is probably the case.

The fit of a linear function is unaffected by the energy spread of the electron beam. For a function that rises nonlinearly, however, the finite spread does produce an effect. For example, for a function that first rises linearly and then approaches a peak, the spread causes the measured slope to be smaller than the actual one at the upper end of the linear region, if the rate at which the linear function rises is faster than that of the nonlinear function. The result can be seen clearly from the application of a convolution to the true function. Thus for the data shown in Fig. 4.1, the finite energy spread of the electron beam only makes the positive slope of the asymmetry in the hatched region appear smaller than it really is. A similiar convolution analysis shows that for the data in Fig. 4.1, the energy spread of the electron

beam is insufficient to produce the observed slope on the hatched region from a function that is actually constant in the region and only begins to rise outside the region.

Based upon the foregoing analysis, we conclude that the probability that the ionization spin asymmtry in the (hatched) 0.5 eV region above threshold is actually a constant function of energy is exceedingly remote. It follows, therefore, that to a high level of confidence the Wannier threshold law does not adequately describe the results obtained for the ionization of atomic hydrogen in the threshold region. If it is assumed that the Wannier law requires the inclusion of higher terms ($E^{3.381}$), which in principle admit the possibility of a non-constant asymmetry, the analysis becomes more complicated. Appendix 2 presents the details of such an analysis from which it is concluded that the slope of the asymmetry in the hatched region should be negative within the constraints of the Wannier theory. Thus the data shown in Fig. 4.1 contradict the Wannier predictions.

4.1.3 Comparision with the Temkin Model

The Coulomb-dipole model discussed in Sect. 2.2 predicts that the ionization cross section near threshold is a rapidly oscillating function which cannot be reduced to a simple power law. Although the underlying principles of the theory have remained largely unchanged since Temkin first introduce them, the functional form for the threshold law has experienced substantial evolution. At the time the hydrogen experiment described in this thesis was completed, the suggested form for the singlet and triplet ionization cross section was[4.1]

$$\sigma_{s,t} = \frac{C_{s,t}\, E}{\chi_{s,t} - ln(E)} \left[1 + E\alpha_{s,t} \cos\left(\frac{\beta_{s,t}}{E^{1/2}}\right) \right], \tag{4.6}$$

where the subscripts s and t refer to singlet and triplet states, and C, χ, α and β are parameters to be determined from fits to the experimental data. Temkin, however, provided some estimates for the expected size of these parameters: $\chi \approx 55$, $\alpha \approx 0.01$ and $\beta \approx 4$.

The rapid oscillation of the function near threshold requires that the theoretical cross section be convoluted with the finite energy spread of the electron beam before a comparision can be made with the experimental results. With f(E) denoting the normalized energy distribution function for the electron beam, we calculated the convoluted singlet and triplet cross sections and the spin asymmetry from the expressions

$$\sigma_s^c = \int \sigma_s\,(E-E')f(E-E')dE' \tag{4.7a}$$

$$\sigma_t^c = \int \sigma_t\,(E-E')f(E-E')dE' \tag{4.7b}$$

$$A^c = \frac{\int A(E-E')\sigma(E-E')f(E-E')dE'}{\int f(E-E')\sigma(E-E')dE'}, \tag{4.7c}$$

which satisfy the relations

$$A^c = \frac{1-r^c}{1+3r^c} \qquad \text{and} \qquad r^c = \frac{\sigma_t^c}{\sigma_s^c} \tag{4.8}$$

For calculational purposes, f(E) was taken as a Gaussian function with a half width of 75 meV, as justified in Sect. 3.3. The convolution was performed over a range of 2.5 standard deviations from the centroid and in steps of 2 meV.

The fitting was carried out by a chi-square minimization procedure using 19 data points (the 13.57 eV point being excluded) over the full 1.7 eV energy range. Although the CD theory may not be valid over such a wide energy range, the limited number of data points available and the number of free parameters prevents any restriction of the range. For purposes of the fit, eight free parameters were used: a polarization factor $f_p = \frac{\Delta_I}{A^c}$, the ratio of proportionality constants $f_c = \frac{C_t}{C_s}$, and the six remaining parameters $\chi_{s,t}$, $\alpha_{s,t}$ and $\beta_{s,t}$ given in Eq. (4.6) for the singlet (s) and triplet (t) states respectively. The initial value for f_p was set at 0.135, which was just the product of electron and hydrogen polarizations, $P_e P_H$, in this experiment, and f_c was set at approximately 0.2 (the observed threshold value of r in Eq. (4.8) is used for guidance). The initial values $\chi_{s,t}$ were then chosen to provide a positive slope in the hatched region. The initial values for the remaining paremeters were set

according to Temkin's theoretical estimates.

The fitting routine ran in the following manner. After the initial values of 8 parameters were entered, the convoluted theoretical spin asymmetries were compared with the experimental values and a χ_ν^2 value was calculated. Then one parameter was allowed to change and a new χ_ν^2 was calculated. If the new χ_ν^2 value was smaller than the previous one, that parameter was again increased or decreased in accordance with the previous change until a minimum χ_ν^2 value was obtained. The first parameter was then fixed, and the second parameter was allowed to vary until another minimum in χ_ν^2 was reached. The process was repeated for all eight parameters and then iterated until the difference between successive χ_ν^2 values differed only by 10^{-5}.

The best fit of the CD model function of Eq. (4.6) to the experimental data is plotted in Fig. 4.1 as a solid line over the whole energy range. The reduced chi-square value is 1.88 for 11 degrees of freedom, corresponding to a confidence level of 3%. By contrast, we note that a linear (structureless) fit over this same region produced a fit with a confidence level of 5×10^{-10}. By absolute standards, however, the confidence level for the CD theory is rather low and the fitting parameters ($f_p = 0.098$, $f_e = 0.587$, $\chi_s = 3.33$, $\chi_t = 22.9$, $\alpha_s = 0.293$, $\alpha_t = 0.281$, $\beta_s = 10.3$, and $\beta_t = 17.6$) are far from those expected, based upon Temkin's theoretical estimates.

Attempts were made to fit two other CD threshold functions,

$$\sigma_{s,t} = \frac{C_{s,t}E}{(ln(E)-\chi_{s,t})^n}\left[1 + \frac{D}{\alpha}sin(\alpha\ ln(E) + \phi_{s,t})\right], \qquad n = 2\ \ or\ \ 4 \tag{4.9}$$

but in neither case was an adequate chi-square value obtained. It should be noted that, in accordance with the discussion in Sect. 2.2, the functions given by Eq. (4.9) are now considered to be the best representations of the CD theory. The value of n = 2 is believed to apply to the region of 0.3 meV < E < 250 meV and the value of n = 4, to E < 0.3meV.

The poor χ^2_ν values may be indicative of the deficiencies in the specific model functions used or of the inappropriateness of the 1.7 eV range to which it was applied. Additionally, it may reflect the inability to determine an absolute chi-square minimum given the pathology of the function and the limitation of the 19 point data set available. A true test of the CD theory will require far better energy resolution than was available in the electron hydrogen studies and a much larger set of data points. Such an experimental program will undoubtedly be extremely difficult, time consuming and costly.

4.2 Comparison with Other Experiments

In this section, we first examine the results of four previous experiments which claimed consistency with the predictions of the Wannier theory. Two of these are experiments that measured the total cross section for double photodetachment of negative ions, and two are experiments that measured the energy partitioning between the two escaping electrons in electron impact ionization of helium.

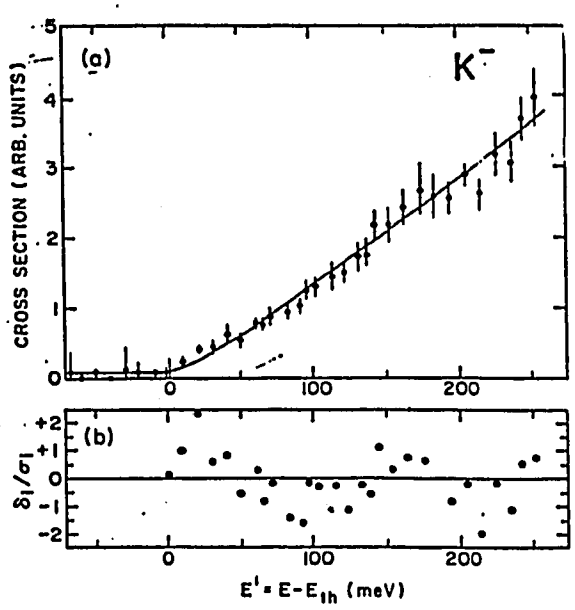

Fig. 4.2 (a) Cross section for double photodetachment of the K^- ion as a function of excess photon energy. (b) Normalized residuals corresponding to the data points in (a).

Fig. 4.2(a) shows the K^- experimental results of Bae and Peterson[4.2] for double photodetachment of K^-. The solid curve shown is the result of a fit of a power law, for which Bae and Peterson obtained an exponent of 1.16(5) with $\chi^2_\nu = 0.69$

for $\nu = 34$ degree of freedoms, corresponding to a 91% confidence level. (The low value of χ^2_ν suggests that the uncertainties might have been overestimated.) Fig. 4.3(a) shows the results of Donahue *et al.*[4.3] for double photodetachment of H^-. Again the solid curve is the result of a fit of power law, for which Donahue *et al.* obtained an exponent of 1.15(4) with $\chi^2_\nu = 1.15$ for $\nu = 66$, corresponding to a confidence level of 19%. Both experimental groups, relying solely on the χ^2_ν values, drew the conclusion that their data agreed with the Wannier prediction of a power law with an exponent of 1.127. We note, however, that although it can rule out a fit, a chi-square analysis alone is insufficient to validate a fit. If a fitted function is correct, it must not only produce a χ^2_ν close to unity, but it must also produce random ordering of the normalized residuals for the experimental data points. In Fig. 4.2(b) and Fig. 4.3(b), we have plotted the normalized residuals $\frac{\delta_i}{\sigma_i}$ for the K^- and H^- experiments, respectively. A visual examination of the K^- results clearly show that the residuals are not randomly ordered. A similiar visual inspection of the H^- results does not yield such a clear conclusion. In order to place these observations in a quantitative context, we carried out four different statistical tests. First, we used a "runs test"[4.4] in which we counted the number of groups in which the succession of residuals were either greater or less than the mean values of all the residuals. For the K^- experiment, the mean value of the residuals is 0.02 with 14 residual lying below the mean and 15 lying above. The 29 residuals lie in only 4

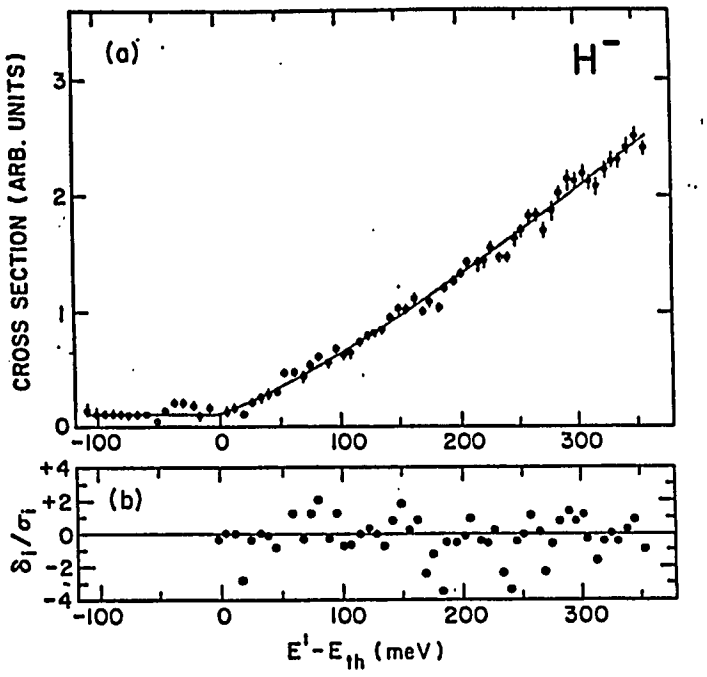

Fig. 4.3 (a) Cross section for double photodetachment of the H^- ion as a function of excess energy. (b) Normalized residuals corresponding to the data points in (a)

groups. However, at the rejection level of 5%, there should be at least 9 groups. The probability that the data are randomly distributed is then less than 5% (actually 0.025%). For the H^- experiment, the same runs test gives an inconclusive result.

As a second statistical measure of non-random ordering, we used the Durbin-Watson statistic,[4,5] in which a parameter d is defined by the relation

$$d = \frac{\sum_{i=2}^{n} (s_i - s_{i-1})^2}{\sum_{i=1}^{n} (s_i^2)}, \tag{4.10}$$

where $s_i = \frac{\delta_i}{\sigma_i}$ is the standarized residual for the ith data point and n is the number of the data points used in the analysis. For the K^- experiment, with n = 29, we

calculated a value for d of 1.26. If there is random ordering, however, the d value should be close 2. In fact, for d = 1.26, the probability that the residuals are ordering non-randomly is 95%. Therefore, there is actually structure inherent in the original curve, which is sufficiently masked by the large error bars to permit the reduced chi-square value to be less than 1. In another words, if the uncertainties of the data points were reduced, then the structure should appear clearly just from visual inspection. For the H^- experiment, with n =54, we calculated a d value of 1.48 for which the probability that the data are ordered non-randomly is again 95%. In both experiments, the residuals are thus positively autocorrelated. (Since the calculated value of d is less than the value for random ordering.)

We used two additional methods to search for autocorrelation.[4.3] In the first test, one residual is expressed as a function of the others according to the linear relation

$$\delta_i = b_i \delta_{i-j} + c_j \ , \tag{4.11}$$

where j = 1 means that the first prior residual, j = 2 the second prior residual, and so on. For both the K^- and H^- experiments, the maximum j was taken as 16. Then, for each experiment, we used a standard linear fit to determine 16 $\{b_i\}$ values and a set of their corresponding statistical uncertainties $\{\sigma_{b_j}\}$. The values so determined are expected to follow a normal statistical distribution. The probability for the occurrence of these values in the distribution is thus the probability that the residu-

als are not autocorrelated. For the K^- experiment, the 16 probabilities range from 1% to 8% with an average of 4%; that is, even back to 16th prior residual, the autocorrelation probability is still extremely high. For the H^- experiment, when j = 1, the non-autocorrelation probability is 6%, and when j=2, it is 17%. Although the correlation is not as apparent as in the K^- experiment, as expected from the plots of residuals, it is still significant at the level of 95%.

In the final test for autocorrelation, we first calculated the difference of successive residuals g_i ($g_i = \delta_i - \delta_{i-1}$), and then used the relation

$$g_i = b_j g_{i-j} + c_j \tag{4.12}$$

in a manner similiar to that applied to Eq. (4.11). For the K^- experiment, the autocorrelated probability is generally greater than 99 %, while for the H^- experiment, the autocorrelation probabilities are 95 and 92% for j=1 and j=2 respectively.

Based upon the four statitical tests of the ordering of the residuals, we therefore conclude that both the K^- and H^- double photodetachment experiments contain structure in the cross section, contradicting the predictions of the Wannier theory. Quantitatively, taking the two experiment together, we can conclude that the probability for random ordering and hence the validation of the Wannier power law is less than 2.5×10^{-3}.

We now consider the two energy partitioning measurements carried out for ionization of helium. In 1978, when the energy partitioning measurement was

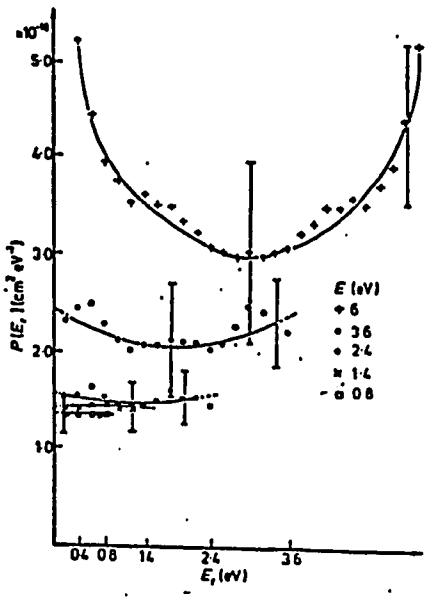

Fig. 4.4. The energy partitioning function of Helium at energies 0.8, 1.4, 2.4, 3.6 and 6 eV above threshold respectively. The size of the uncertainties, according to Pichou *et al.* ranges between 29% to 45%.

reported by Pichou *et al.*,[4.7] the Wannier theory was understood to predict a uniform energy distribution for each of the outgoing electrons. The results of the work of Pichou *et al.* are are shown in Fig. 4.4. At the lowest energy, 0.8 eV above threshold, it can be seen that within the ± 15% uncertainties, the distribution is indeed a constant, consistant with the pioneering work of Cvejanovic and Read that had been reported 4 years earlier. However, the precision of the measurement is clearly rather poor. Moreover, at energies 1.4, 2.4, and 3.6 eV above threshold, Pichou *et al.* also claimed that their results were consistent with a flat distribution within the quoted uncertainties. However, a quick look at the experimental data points reveals that the reduced chi-square values for the three curves are unbelievably small, since the error bars shown are so large. If the data points are accurately

given, then the error bars presented must be overestimated. The authors in fact realized that their uncertainties were rather pessimistic when they commented on the good reproducibility of the results they obtained regardless of experimental conditions. The uncertainties may have been determined correctly for absolute measurements, but for the relative behavior of the data, which was the object of the experiment, they are certainly too large. Thus, the conclusion that the distributions are flat is not valid. If one looks at the data points closely, one sees that the experimental curves are similiar to each other, each having two subsidiary peaks close to both ends of the curve, suggesting that, in the absence of some bizarre systematic effect, some structure is present.

In 1984, by using a computer integration of the Wanner equations, Read[4.8] derived an energy partitioning function which contained a 5% nonuniformity, as shown in Fig. (4.5a). In 1985, Hammond *et al.*[4.9] reported on the results of another helium experiment claiming to validate the Wannier-Read prediction. In one study, the results of which are shown in Figs. 4.5(a) and (b), an electron energy analyzer was set at constant pass energy and the incident electron energy was varied, thus effectively changing the ratio of the scattered electron energy, ε_1, to the total excess energy E. This experiment has been considered as a reasonably precise test of the Wannier theory, since the agreement between theory and experiment was claimed to be (visually) quite good. Although for a high incident electron energy, correspond-

ing to low x ($x = \frac{\varepsilon_1}{E}$) values in Fig. 4.5(a), the experimental data points fall below the theoretical curve, the authors argue that the deviations might be related to systematic problems, which caused the data to shift along x, making the data set asymmetric with respect to x = 0.5. (Symmetry about this point must be occur since the two electrons are indistinquishable.) The claim of an asymmetry is not warranted, however, since as shown by the solid line in Fig. 4.5(b), the experimental data points can be fitted very well by quartic function with an almost ideal χ_ν^2 of 1.02 for 12 degrees of freedom, corresponding to a confidence level of 51%. By comparision, Read's function, which of course is also symmetric, yields a χ_ν^2 value greater than 4, with a corresponding confidence level much less than 1%. Therefore, the data points are symmetric around x = 0.5, contrary to what the authors surmised, and the claimed agreement between the theory and experiment is on tenuous footing. For completeness, we show in Fig. 4.5(c) the results obtained from a second study of Hammond *et al.*, in which the incident electron energy was fixed and the pass energy of the energy analyzer was scanned. The error bars are so large that effectively no conclusion can be drawn from the data.

Although most previous experiments have claimed to be consistent with the Wannier theory, there are a few that reveal disagreements to some extent. Very recently, the spin asymmetry of electron-cesium ionization was reported by Baum *et al.*.[4.10] The results of their recent work, along with asymmetry measurements on

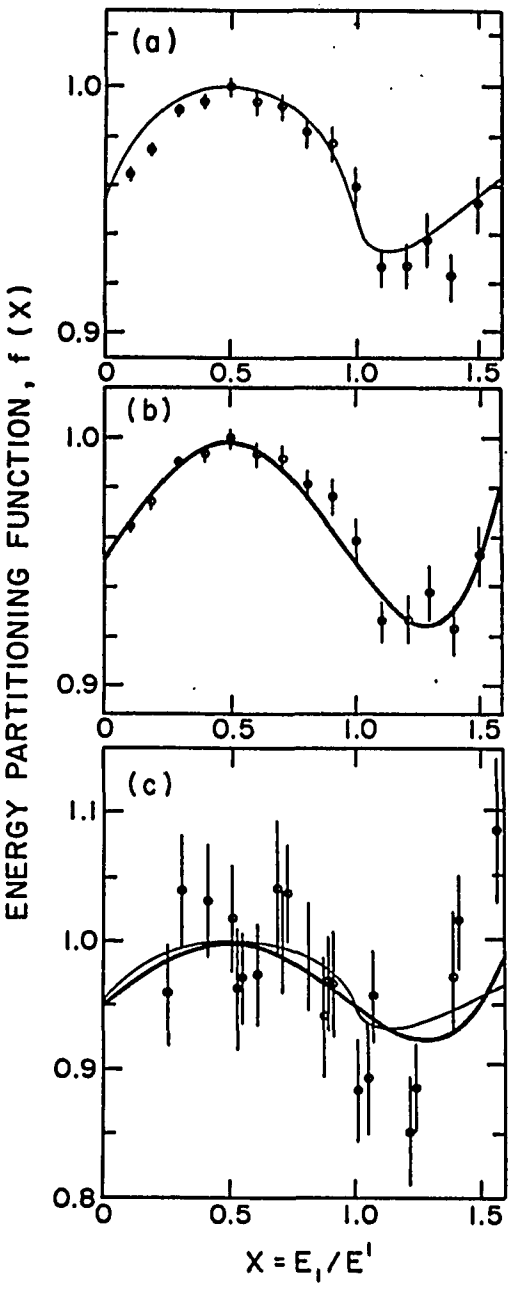

Fig. 4.5. Study of energy partitioning function f(x) showing in (a) the data obtained by the constant residual energy mode (CRE) of the electron energy analyser along with the theoretical Wannier prediction developed by Read, in (b) the data of (a) along with a quartic fit $[f(x) = 0.191(x-0.5)^4 - 0.237(x-0.5)^2 + 0.998]$ illustrating the symmetry of the data with respect to x = 0.5, in (c) the data obtained by the electron energy mode along with Read's theory (thin line) and quartic fit to the (CRE) data (heavy line).

other alkali atoms, are shown in Fig. 4.6.[4.10] Although the data points are generally not very close to the threshold--the energy is expressed in units of the ionization potential, I, (3.894 eV for Cs)--it is very clear that the spin asymmetry is a rising function of energy. The first two data points, which lie very close to threshold and have distinctly different asymmetries, are consistent with this behavior. Similiar results were observed earlier for lithium,[4.10] but the energy resolution in that experiment was worse. It should be noted, however, that experiments on sodium and potassium did not reveal any slope in the asymmetry.[4.11]

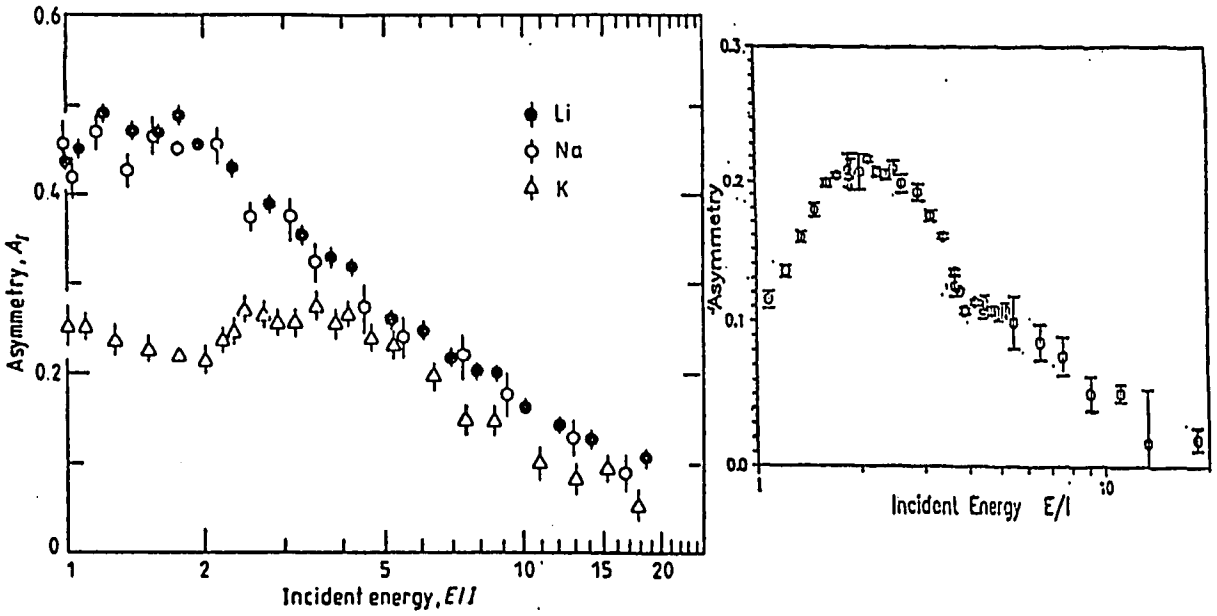

Fig. 4.6. Ionization spin asymmetries for alkali atoms showing (a) the results for Li, Na, and K as a function of incident electron energy in units of the ionization potential energy, (b) the results for Cs as a function of incident electron energy in units of ionization potential (3.89 eV).

The triple differential cross section for electron impact ionization of atomic hydrogen at an energy of E = 2 eV was recently measured.[4.12] The observed

angular distribution of the electrons differed substantially from the distribution obtained in a similiar experiment carried out on helium. The authors, Schlemmer *et al.*, and Rosel *et al.*, pointed out that this difference suggested that the dynamics of the interaction was already very important at this incident energy, contradicting the assumptions inherent in the Wannier theory. Subsequent to the publication of the above results, however, Pan and Starace[4.13] pointed out that the difference could be accounted for within the context of the Wannier picture. Even more recently, Madison[4.14] has challenged the theoretical calculation of Pan and Starace. At present this issue seems unresolved.

The technological difficulties in the experimental work on near-threshold experiments has led to very few high precision tests of the Wannier theory. The study of spin-dependence, angular distribution, and energy partitioning in recent years, however, has opened up new windows through which the Wannier theory can be viewed. In the light of the spin asymmetry results for atomic hydrogen, it seems that more high precision measurements are now in order. One such proposed study, high precision H^- double photodetachment experiment, will be reviewed briefly in Chap. 6.

4.3 Theoretical Insight into the Deviation from the Wannier Theory

In Chap. 2, we discussed the three most important features of the Wannier picture for near threshold ionization--the ergodic hypothsis for the reaction zone, the back to back departure of the two electrons in the Coulomb zone, and the near equality of the radial coordinates for the electrons in the Coulomb interaction zone. These three key points will be discussed separately in this section with reference to the experimental results for the spin asymmetries observed with atomic hydrogen.

It is true that the interaction in the inner zone is very strong. The probability that two electrons will occupy one point in phase space may therefore not differ too much from the probability that they will occupy another point. The evolution of the system in the reaction zone thus has features similiar to those of chaotic motion. From the study of quantum chaos,[4.15] it well known (at least for one and two dimensional systems) that there are still some classical orbits which are particularly favored, as evidenced from the general calculation of the probability density. This bahavior may be even more important for the double escape process because it samples only restricted parts of the phase space. Therefore, dynamic interactions may play a role in the near threshold region, since the phase space leading to double escape changes as the incident electron energy is changed. In another words, the preparation of the initial state during the reaction may well be important for double escape, in contrast to the quantum mechanical extensions of the Wannier theory in

which only the final-state wave function is used to derive the threshold law.

To qualitatively understand the positive slope of the spin asymmetry in the near threshold region and its return to zero when E is very large (500 eV for hydrogen), we somewhat imprecisely divide the ionizing collision into two separate processes, one involving the dynamic reaction of the atom to the incident electron and the other involving momentum transfer from the incident electron to the bound electron resulting in ionization. In the case of the first process, where the incident electron energy is very close to threshold, the two electrons are very similar in their momentum space properties. The angular momentum and configuration space behavior thus become dominant factors in determining the singlet and triplet character of the two-electron system. During the collision, the atom reacts by becoming polarized, the degree of which depends upon the atomic polarizability and the time-averaged electric field the atom experiences during the collision. If the polarization is large, the two electrons will have only a small probability of sharing the same configuration space when ionization occurs. If, however, the polarization is reduced, the probability of similar configuration space properties will be enhanced, and the two-electron spinor will have to display an increasingly antisymmetric or singlet character. (The precise nature of this enhancement, of course, will depend on the angular momentum character of the two-electron system, as we have seen previously.) It is precisely such a reduced polarization that occurs when the energy of

the incident electron is raised. Under these circumstances, the collision time shrinks and the time averaged electric field becomes smaller. Thus, as the incident electron energy rises in the region just above threshold, the probability of singlet scattering grows faster relative to that of triplet scattering, and the asymmetry is an increasing function of energy illustrated by the following equation

$$\frac{dA}{dE} = \frac{3r}{(1+3r)^2}\left[\frac{1}{\sigma_s}\frac{d\sigma_s}{dE} - \frac{1}{\sigma_t}\frac{d\sigma_t}{dE}\right]. \tag{4.13}$$

Far from threshold, when the incident electron energy is very large, the second process, momentum transfer, dominates. As the incident energy rises beyond the threshold region, the momentum transfer from the incident to the atomic electorn has a steadily decreasing probability of providing the same configuration space character for the two final-state electrons, leading ultimately to the equality of σ_s and σ_t at high energies and a value of zero for the asymmetry. The structure presented in Fig. 4.1 when E > 0.5 eV, of course, can not be explained in this way and will be addressed later.

We now turn to the question of the mutual opening angle, θ_{12}, between the escaping electrons. At any finite energy above threshold, it can be shown from the equations in the appendix of the Wannier's[4.18] original paper that the mutual angle between the two electrons is asymptotically finite. Thus we can express γ in the asymptotic form

$$\gamma = \pi - \theta_{12} = A\ cos(B + C)\ , \tag{4.14}$$

where A, B, abnd C are constants. The similarity principle, used in Wannier's derivation states that at some energy E_1, all the orbits are similar to those at another energy E_2. Thus, electrons with smaller excess energies will escape from the residual ions through orbits that have small cone angles in γ. The cone angle shrinks to zero when the excess energy is zero. In his original work, Wannier ignored the behavior of this angular correlation and assumed that it had no effect on the threshold law.

Peterkop,[4.16] however, showed that Eq. (4.14) has a semiclassical equivalent given by

$$\gamma = u_2 \ , \tag{4.15a}$$

where u_2 is the hypergeometric function in Eq. (2.8). It can be shown that as $\rho \rightarrow \infty$, u_2 takes the form

$$\lim_{\rho\to\infty} \zeta = \lim_{\rho\to\infty} u_2 \rightarrow DE^{\frac{1}{4}} \sin(\phi + \tfrac{1}{2}|\mu_2| \ln(E)) \ , \tag{4.15b}$$

where D and ϕ are constants specifying each orbit and the remaining parameters are the same as those used in Chap. 2. As $E \rightarrow 0$, ln(E) will be very large, thus giving rise to an infinite number of zeros in γ. The rapidly oscillating term in Eq. (4.15b) was neglected in Peterkop's original derivation, where he used the form expressed in Eq. (2.30). Physically, Eq. (4.15b) suggests that for a certain trajectory {D, ϕ}, the cone angles with which the two electrons escape depends upon the electron energy E. At some energy, the two electrons have to escape back to back ($\gamma = 0$), while at

other energies, they are only confined to a certain cone angle. (The complex behavior for θ_{12} and hence of the orbits leading to double escape may be physically related to the requirement that $r_1 \sim r_2$ regardless of the energy partitioning.) This behavior shows directly the break-down of the similarity principle used in the classical Wannier derivation. Such a complicated behavior in the angular correlation also calls into question the derivations of Rau and others[4.19] who solved the Schrodinger equation at E = 0, and extrapolated their results to finite energy E, ignoring the energy dependence in θ_{12}.

A more direct consequence of Eq. (4.15) is the question that how valid the $E^{\frac{1}{4}}$ power law is for the width, $\Delta\theta_{1/4}$, of the angular distribution. Although the observed angular distribution of the two electrons includes contributions from all the trajectories, as discussed by Gailitis and Peterkop,[4.17] it appears that they did not take into account the sinusoidal behavior contained in Eq. (4.15). The inclusion of such a sine term in the denominator of their derived expression would result in many singularities, and the resulting $E^{\frac{1}{4}}$ power law for the angular width thus becomes suspect. The classical derivation and the quantum mechanical derivation of Rau fail to reveal such behavior because it can only be observed when E > 0. (In Feagin's derivation,[4.20] the same behavior is not apparent probability due to the different coordinate system he used.) Experimentally, the width of the angular distribution was measured in only one study, that of Cvejanovic and Read, which contained

only 5 data points at modest precision. The best fit yielded an exponent of 1/5 instead of 1/4 with 3 degrees of freedom. Clearly a search for oscillations is precluded by the paucity of the data. More extensive and precise measurements are obviously in order.

Whether or not a power law is the correct representation for the width of angular distribution is only one issue. A second issue is whether the size predicted by the $E^{1/4}$ law is correct. The coefficient in front of the power law, denoted as b in Eq. (2.16), is 39^o from the experiment of Cvejanovic and Read. All of the theoretical calculations result in higher values, with the smallest of them being Feagin's prediction of 68^o. The size of the theoretical prediction, moreover, introduces an inconsistency in the calculation. Using Feagin's value of 68^o for b, for example, we find an angular width of 38^o for E as low as 100 meV, in apparent contradiction of the small angle assumption made in all the theoretical derivations. As a final comment on the angular correlation, we note that intuitively it would seem that the angular correlation should really be less tight than the radial correlation, because the former mostly affects the mutual repulsion between the two electrons which occurs at distances that are larger than that the distances between the electron and and residual ion.

Based on the foregoing discussion of the angular correlation, we argue that the angular behavior of the two electron system may be a very complicated function of

the incident electron energy. Such behavior calls into qustion the derivations of the threshold law which either neglect its role or use extrapolations from E = 0 to finite values of E. For a correct derivation of threshold behavior for E > 0, we believe that the angular distribution of the two electrons must be taken into account. Whether a simple power law is satisfactory remains a question for both theory and experiment to address.

We turn finally to the strong radial correlation implied by the statement $r_1 \sim r_2$ in the Wannier theory. While such a correlation may be strong, the large angular distribution, even in hatched ionization region (Fig. 4.1), taken together with a coupling between the radial and angular motions, weak though it may be, creates the possibility of superimposing structure on the cross section function which still may have an envelope given by the Wannier power law. As the incident electron energy rises above the hatched region (E > 0.5 eV), the increasingly energetic electrons experience radial correlations that become less tight. The coupling between the angular and radial motion grows correspondingly, thus giving rise to the possible appearance of complicated structures.

Chapter 5. Future Possibilities

In Sect. 5.1 of this chapter, I will discuss the first stages of the development of a cooled polarized electron source, which has as its objective the production of a polarized electron beam with an energy spread narrower than the ~ 180 meV value that characterized the beam used in the present studies. In order to effectively reveal any spin-asymmetry structure in the hatched (Fig. 4.1) threshold region ($E \leq 0.5$ eV), a beam with an energy spread of 50 - 100 meV is required. To this end, a polarized electron source has been built in which the GaAs crystal can be cooled by liquid nitrogen and the energy spread of the beam can be analyzed by a retarding potential analyzer. As we have seen, the success of threshold asymmetry studies strongly depends upon long life time of the GaAs crystal. Therefore, another purpose of the cooled source development is the determination of whether one can obtain an enhanced life time at low temperatures by the same *in-situ* cesiation technique, that proved successful at room temperature. A low-temperature also provides the advantage of higher polarization.[5.1]

In Sect. 5.2, I will briefly describe the proposed high precision measurement of double photodetachment of the negative hydrogen ion which should be able to provide another decisive test of the Wannier threshold law. In the ten years that have passed since the original H^- studies were carried out, advances in laser technologies

and improvements in the negative-ion beam-line at the Los Alamos Meson Physics Facility (LAMPF) have taken place, which now make such high precision measurements possible. In Sect. 5.3, the last section of the thesis I will suggest some other future experiments which I believe can contribute to a better understanding of the threshold problem.

5.1 Cooled GaAs Polarized Electron Source

5.1.1 Layout of Apparatus

The overall layout of the apparatus of the new GaAs polarized electron source is shown in Fig. 5.1. A combination of a turbo-pump (Varian, model Turbo-V) and a mechanical pump (Varian, model CD-300) can pump the system down from atmosphere to about 1×10^{-8} Torr in about 8 hours. The Mott scattering chamber, shown schematically in Fig. 5.1(b), is for future usage. It can be isolated from the electron source chamber by a bakeable in-line valve (Varian, model # 951-5052). The vacuum chambers are typically baked at 200 °C into the Turbo pump for approximately three days, after which the source and the Mott chamber are isolated from each other, with the source chamber now pumped by a 150-l/s conventional ion pump (Perkin Elmer, model # 207-0160). A base pressure in the low 10^{-10} Torr range is achievable after about 3 days. Cooling of the crystal is provided by a liquid nitrogen (LN_2) reservoir in the shape of a hollow stainless steel cylinder 127 mm in outer diameter and 69.9 mm long, having a 2.4 mm thick wall, a 2.4 mm "back" end cap, and a 6.4 mm "front" end cap. This rather large container size was chosen to reduce the consumption of LN_2 and to provide a large surface area for the condensation of residual gases which would otherwise contaminate the GaAs crystal and thereby shorten the lifetime of the source. The crystal and the reservior are connected with the use of an OFHC copper block and a Macor mounting plate, as will

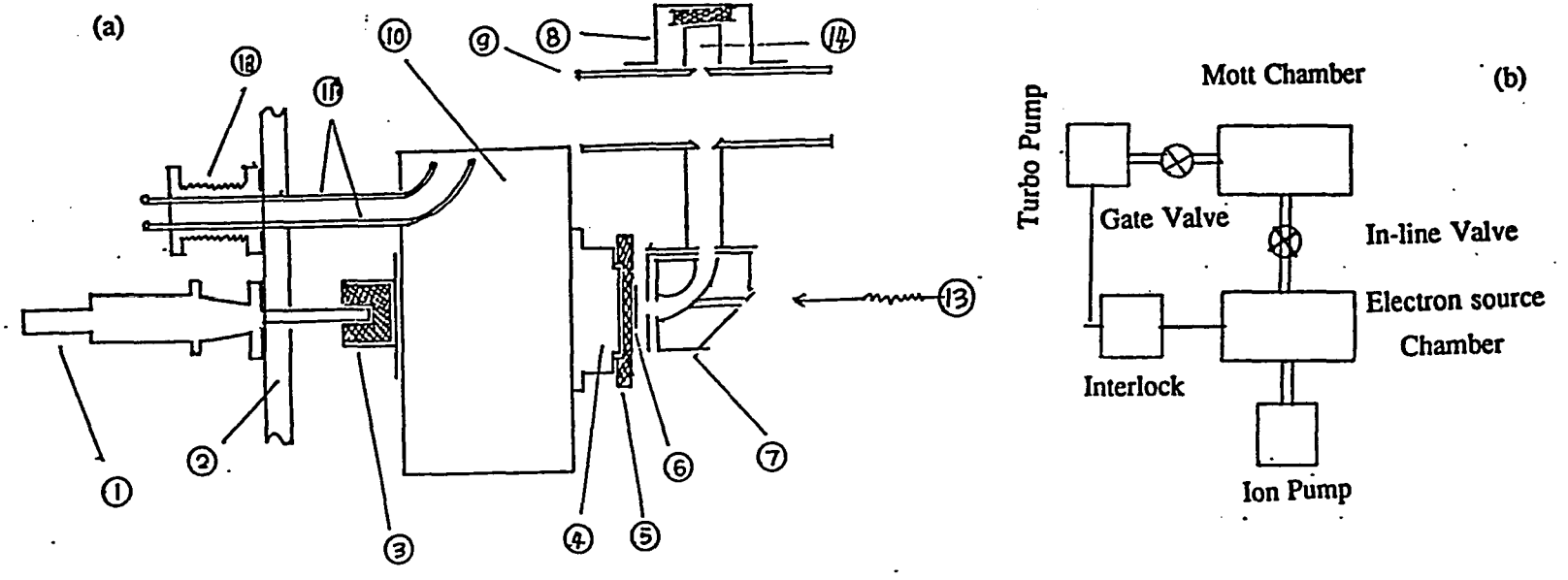

Fig. 5.1 Scale drawing of the cooled polarized electron source showing (1) manipulator, (2) flange of the six-way cross, (3) manipulator coupling, (4) OFHC copper bloack, (5) Macor mounting block, (6) GaAs crystal, (7) 90° electrostatic bender, (8) gounded shield, (9) retarding plate, (10) LN_2 reservoir, (11) LN_2 inlet and gas release tubes, (12) welded bellow, (13) laser beam, (14) Faraday cup; (b) block diagram of the vacuum system.

be discussed in more detail shortly. Two cesiators (SAES Getters, model St 101-Cs) embedded in an anode extraction plate, are symmetrically positioned to reduce the size of magnetic and electric field created by the heating currents passing through them (cf. Fig. 3.3). A 90° electrostatic bender, of the same design as the one used in the hydrogen asymmetry studies, separates the electron beam from the incident laser beam-line and provides a transverse polarization vector suitable for Mott polarimetry. To avoid any confusion in the measurement of the electron energy spread introduced by the long transport of the beam, a retarding field analyzer is installed immediately after the exit plane of the bender. The electron beam, after it passes through the bender, is imaged at an aperture, 2 mm in diameter, that is contained in a molybdenum insert mounted in a 100 mm diameter stainless steel disk, which serves as the entrance to the analyzer. This entrance disk is held at the same potential as the mean potential of the centriod of the bender. The retarding disk, also 100 mm in diameter, has a molybdenum insert with a 5 mm diameter aperture. The retarding disk is covered with a molybdenum mesh characterized by 85% transmmision (900 mesh units per 627 cm^2 with wire diameter of 0.1 mm). The mesh ensures that the equipotential lines remain planar across the retarding aperture, a condition that must be met if the energy resolution of the analyzer be strickly dependent on the aperture size. The electrons passing through the retarding plane are detected by a simple Faraday cup.

Experience gained from the hydrogen asymmetry studies strongly suggested that the crystal position, which determines the object position of the electron optics, should be adjustable along the horizontal direction. To this end, a linear motion feedthrough is coupled to the back end of the LN_2 container, allowing the container and crystal to be moved as a single unit. (The container and the feedthrough are thermally isolated by a thick wall, hollow Macor cylinder.) Using this arrangement, the crystal can be moved a total distance of about 12 mm, sufficient to permit the use of a separate cesiator for activation if so desired. The LN_2 filling system utilizes one stainless-steel welded bellows, 3.18 mm in diameter and 25.4 mm long, that is welded to Conflat "mini-flanges" on each end: one of the mini flanges couples to the large end flange of the vacuum chamber and the other to a mating mini flange through which two small stainless steel tubes (3.2 mm in diameter) pass as welded lead-throughs. Each of these tubes is welded to the end cap of the LN_2 container, as shown in Fig. 5.1(a), one serving to feed LN_2 to the reservior and the other permitting the release of gas from the reservior.

A detailed design of the Macor insulating plate for the GaAs sample is dipicted in Fig. 5.2. The plate is in the shape of a rectangular solid, 6.4 mm thick, which is milled out in the central section of its back surface to a thickness of 2.4 mm to improve the thermal conduction between the LN_2 reservior and the GaAs crystal. The GaAs sample, measuring 10 mm x 15 mm, resides in the center of the

front surface of the Macor plate which is milled out further to create a thickness of only 1.7 mm between the crystal and the OFHC cooper block attached to the LN_2 container. A fine gauge thermocouple (127 μm wire-diameter) is placed beneath the sample for temperature monitoring when the sample is cooled or heated. Since the temperature ranges from 80 to 870 K, a K-type Chromel-Alumel thermocouple is used. A pair of tantalum clamps, attached to the ends of the Macor plate, holds the sample and permits it to be ohmically heated and biased. For better contact, both clamps are pressed by a molybdenum key.

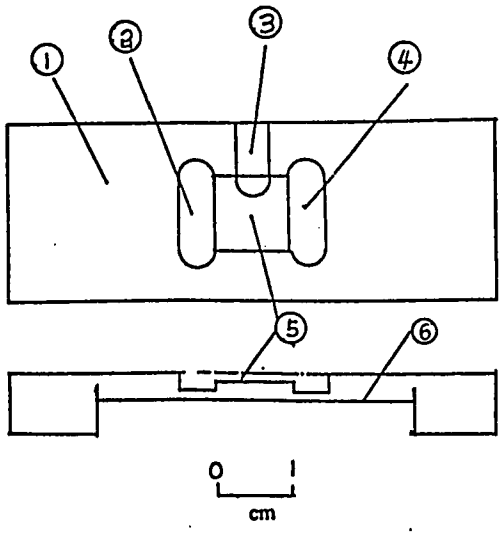

Fig. 5.2. Scale drawing of the macor mounting plate showing (1) Macor mounting plate, (2) slot for tantalum clamp, (3) location of thermocouple, (4) slot for tantalum clamp, (5) location of the GaAs crystal, (6) "back" surface of the plate which is in close contact with an OFHC copper block.

Although its thermal conductivity at low temperatures is somewhat less than that of sapphire--the insulating material used in the room temperature source (cf.

Fig. 3.2)--Macor was chosen for the present low-temperature source because it is much easier to machine and costs far less than sapphire. We can estimate the operating temperature of the GaAs sample when the Macor mount is used in the following way. From the manufacture's technical report[5.1], the thermal conductivity k, of Macor at 20 K is 6.5×10^{-4} W mm^{-1} K^{-1} and is a rapidly increasing function of temperature between 3 and 20 K. From about 280 K to 470 K, however, the thermal conductivity is almost a constant with a value of 13×10^{-4} W mm^{-1} K^{-1} . Since a temperature of ~ 100 K is the operating goal for the low-temperature source, we take k as 10×10^{-4} W mm^{-1} K^{-1}, noting that this value is probably rather conservative. The temperature difference, ΔT, across the Macor mount is calculated from the standard one dimensional heat flow equation

$$\Delta T = \frac{Q\ \Delta L}{k\ A}, \tag{5.1}$$

where A is the area of the Macor plate, Q the heat through the plate, and ΔL the thickness of the plate. The heat, Q, is taken as the heat radiated from the two cesiators embedded in the anode plate. Using a temperature of 800°C for the cesiators, corresponding to a heating current of 7 A, we calculate that the total heat radiated to the Macor plate is about 1 W, assuming the upper limit of unity for the emissivity of the cesiators and an emitting area of 10^{-5} m^2. For mechanical reasons, the thickness of the Macor plate was chosen as 2.4 mm and its dimension such that its total area is 600 mm^2. The temperature gradient across the sample, as calculated

from Eq. (5.1) for the values of Q, ΔL, k and A just given, is 4 K. Thus with the LN_2 reservior having a temperature of 77 K, the sample should reach a temperature of 81 K, if the small temperature gradient across the OFHC cooper block is neglected. The calculated value of ΔT and hence that of the crystal is slightly high because immediately behind the sample, the thickness of the Macor is only 1.6 mm. However, we have neglected the effects of the radiation from the wall and the anode plate to the GaAs crystal as well as the imperfect thermal contact between the OFHC cooper block and the Macor plate, both of which will contribute to a higher temperature during LN_2 operation. We thus use 100 K as a calculated estimate of the crystal temperature.

5.1.2 Electron Energy Analyzer

If the GaAs crystal is located a distance d from the anode plate, the finite size of the laser spot effectively produces a real point-like electron source at a distance 2d from the anode.[5.2] With the anode treated as an aperture lens of focal length -4d,[5.3] a virtual image is formed at a location 4d/3 from the anode. Now the exit plane of the 90° bender contains a rather large aperture (2 mm in diameter) which permits beams with energy spreads as large as 500 meV (FWHM) to pass through the dispersive bender without attenuation. (A detailed calculation of the characteristics of the 90° bender is presented in Appendix 3.)

The rather large exit-plane aperture dictates that the retarding plane of the energy analyzer be located far away in order that the finite size of the image of the electron beam not be a problem for the calculation of the energy resolution of the analyzer. As a result, the separation, D, between the exit aperture and the retarding plane is chosen to be 50.8 mm.

To make the electric field rather uniform, the diameter of the retarding disk has to be large. Thus as we already stated, the diameter of the disk was chosen to be 100 mm. The radius, r, of the aperture on the retarding plane was 2.5 mm. The acceptance of the energy analyzer is then determined by the trajectories of those electrons that can travel a longitudinal distance greater than or equal to D, and with a transverse displacement smaller than $r + R_2$, where R_2 is the radius of the beam at

the 2-mm diameter exit-plane aperture. From a classical trajectory analysis, the maximum cone angle, α_m, that the electrons may have initially and still pass through the retarding plane aperture is given by

$$\alpha_m = \frac{r + R_2}{2D}. \tag{5.2}$$

assuming a uniform decelerating field (parabolic electron trajectories). The analysing power, $\frac{\Delta E_a}{E}$, of the energy analyzer, usually taken as the sqaure of this angle,[5.4] is then

$$\frac{\Delta E_a}{E} \approx \left[\frac{r + R_2}{2D}\right]^2 \approx 1.2\times10^{-3}, \tag{5.3}$$

where R_2 has been taken as its maximum value of 1 mm. At an average energy of 50 eV, the energy resolution of the analyzer is thus 60 meV. As we have noted, the influence of the fringe electric field should be small since the diameter of the disk, 100 mm, is far bigger than the nominal diameter of the electron beam, which is less than 2 mm. Preliminary results obtained with a thermal cathode will be discussed in Sect. 5.1.3.

5.1.3 Experimental Results

The electron energy analyser was first tested with a BaO thermal cathode. The cathode was placed in the same location as that intended for the GaAs crystal. In practice, it was found that in order to keep the collection efficiency of the Faraday cup constant, the voltage across the retarding plate and the Faraday cup had to be constant as the retarding potential was scanned. A battery-operated power supply was used to meet this requirement.

Fig. 5.3 shows a typical experimental retarding curve. The energy distribution curve, from which the FWHM value follows, was obtained by differentiating the retarding curve numerically. If the energy distribution curve is a Gaussian with width $\pm \sigma$, however, the slope of the retarding function at its midpoint can be shown to be $\frac{1}{\sigma \sqrt{2\pi}}$. Thus σ can be determined from the experimental retarding curve directly if a straight line is drawn through the midpoint tangent to the curve. The characteristics of a Gaussian permit an even greater analytical simplification. Consider two horizontal lines drawn at 10% and 90% of the maximum value of the experimental retarding curve. Then it can be shown that the difference, $\Delta E_{90\text{-}10}$, between the two horizontal energy coordinates associated with the 10% and 90% intercepts of the straight lines follows the relation

$$\Delta E_{90\text{-}10} = 2.005\sigma . \tag{5.4}$$

The FWHM value, ΔE_{FWHM}, for the energy spread of a Gaussian distribution is thus

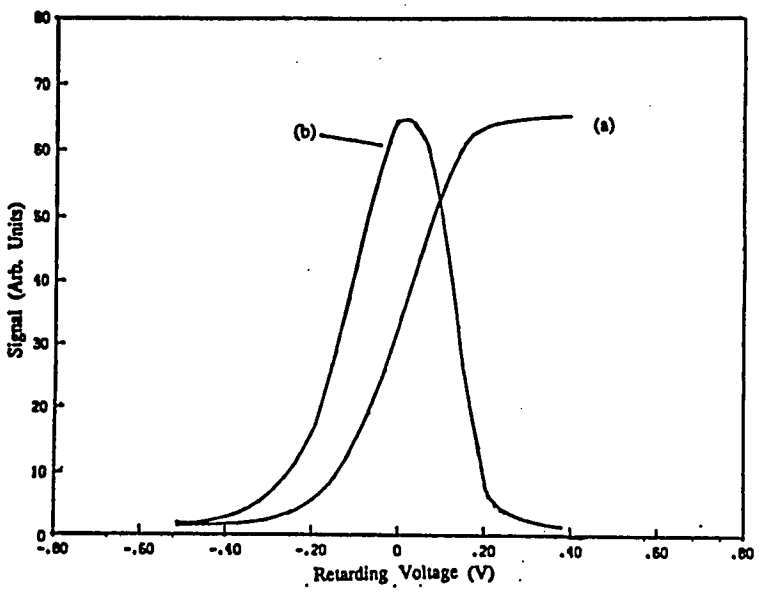

Fig. 5.3 The experimental energy distribution of a BeO thermal crystal. The retarding curve, labeled (a), was numerically differentiated to obtain the energy distribution shown in (b).

given by

$$\Delta E_{FWHM} = 1.18\Delta E_{90-10} . \tag{5.5}$$

Although the electron energy distribution in our case is not exactly Gaussian, the values of ΔE_{FWHM} obtained from Eq. (5.5) and from differatiation of the experimental retarding curve agree with each other within the experimental uncertainties, which are about ± 10 meV under typical operating condition.

In order to examine the influence of stray magnetic fields on the performance of the analyzer, 25 experimental retarding curves were recorded at a 90°-bender-pass-energy of 83.3 eV, each curve corresponding to a different set of magnetic

field components produced by three mutually orthogonal pairs of field coils. With the stray field component allowed to vary between 0 and about 1 Gauss at the retarding plate, and with all other operating parameters held fixed, it was observed that the values of $\Delta E_{90\text{-}10}$ remained constant to within ± 10 meV. Values of ΔE_{FWHM} obtained for different settings of the extracted beam current, however, demonstrated that the measured energy spread could vary greatly (by about 50 meV) when the extracted current exceeded 5 μA, a behavior that is consistent with space charge effects. For extraction energies between 20 and 130 eV, ΔE_{FWHM} remained constant within ± 10 meV, provided the beam current remained below 1 μA.

The validity of the calculated energy resolution, ΔE_a, of the retarding potential analyzer obtained in Sect. 5.1.2 can be demonstrated from the thermal cathode measurements. We first divide the value of ΔE_a by 2.36 to obtain the corresponding Gaussian width σ_a. Then within the framework of Gaussian distribution, we can express the true width of the electron beam, σ_e, in terms of σ_a and the measured width σ_m, in accordance with the relation

$$\sigma_e^2 = \sigma_m^2 - \sigma_a^2 . \tag{5.6}$$

In writing Eq. (5.6) we have assumed that the corresponding Gaussian width for the 90° bender acting as an energy analyzer is much larger than σ_e. Thus the energy distribution of the electron beam passing through the 90° bender is left unchanged, a situation that is experimentally realized, as can been seen from the discussion in

Appendix 3. For three pass energies 33.3, 60 and 83.3 eV, with corresponding σ_a values of 17, 25.4, and 42.4 meV, as calculated from Eqs. (5.3), (5.5), and (5.4), we measured resultant widths, σ_m, of 87.5, 90 and 105 meV respectively. Then according to Eq. (5.6), the corresponding calculated values of the true electron energy Gaussian width, σ_e, are 85.8, 86.3, and 96 meV, rerspectively, which agree within the estimated uncertainty of ± 10 meV. (We note that at low pass energies, the electron beam is easily deflected by a stray magnetic field or stray electric field, resulting in an extrodinarily broad energy distribution curve. Thus at 33.3 and 60.0 eV, only the smallest values of σ_m displayed excellent consistency and their averaged value was used.)

Having experimentally established the performance and characteristics of the retarding field analyzer, we began studies with the GaAs crystal. With the GaAs sample installed and the pressure of the chamber at about 5×10^{-8} Torr, we allowed the LN_2 container to fill in order to test the thermal contact between the crystal and the container. With the chamber thermally insulated and 6 hours allowed for complete thermalization, the thermocouple indicated a temperature of 200 K, a value that is much higher than expected presumably due to diffusion of the chromium atoms in the thermocouple wire under vacuum.[5.13] With the LN_2 container unfilled, a maximum power of 7 W was used to ohmically heat the sample (as discussed in Sect. 3.2) during which time the thermocouple indicated a maximum temperature of

300 K, again suggesting diffusion problems. For future measurements, an iron-constantan thermocouple, which does not suffer from diffusion problems, would be more appropriate. The first activation of the GaAs crystal in these preliminary stages yielded a maximum photocurrent of 2 μA at incident laser power of about 10 mW. Better quantum yield for the GaAs crystal should be obtainable in the future, based upon past experience.

5.2 Double Photodetachment of the Negative Hydrogen Ion

The study of double photodetachment of the negative hydrogen ion provides an excellent technique for testing the Wannier threshold law for several reasons. First, the negative hydrogen ion has a simple atomic structure. Second, the use of a laser to create the double continuium final state results in an energy resolution that is one to two orders of magnitude better than that achievable with an electron beam. (In the first H^- study, Donohue *et al.*[5,6] obtained a resolution of 7 meV, for example.) Thus the region very close to threshold can be probed in detail. Last, the dipole selection rule restricts the final state to a $^1P^o$ configuration, making the experiment potentially much more sensitive to deviations from the Wannier predictions than the electron-impact ionization counterpart in which a multiplicity of spin and angular momentum final state configurations contribute the total cross section.

As noted in Sects. 1.3 and 4.3, the original H^- experiment of Donohue *et al.* used a relativistic negative hydrogen ion beam produced at the Los Alamos Meson Physics Facility (LAMPF) with an 800 MeV nominal energy. A frequency quadrupled pulsed Nd:YAG laser provided photons with a lab-frame energy of 4.66 eV (corresponding to a wavelengh of 266 nm). In the rest frame of the ions, the photon energy was Doppler shifted to values between 1.63 and 15.6 eV, depending upon the intersection angle between the laser beam and the ion beam. In the experiment of Donohue *et al.*, background signals due to residual gas stripping of the pri-

mary negative ion beam and field ionization of excited Rydberg atoms by motional electric fields posed significant problems. The experimental data were also degraded by instabilities in both the laser beam and the ion beam. Therefore, the results were not of extraordinarily high precision and tests of threshold theories were far from complete.

Eight years have elapsed since the results of the H^- experiment were reported. Since then, there have been many advances in laser technology and in the LAMPF beam characteristics. These combine to provide the possibility of repeating the H^- experiment at high precision ($\pm$ 10^{-2}-10^{-3} in relative uncertainties).[5.2] Such a precision together with the very fine energy resolution (~ 2 meV) should provide a decisive test of threshold theories.

One of the greatest problems encountered in the first LAMPF investigation was the low repitition rate (10 Hz) combined with the narrow pulse width (10 ns) of the Nd:YAG laser which resulted in a temporal mismatch with the ion beam that was characterized by a pulse structure consisting a 120 macropulses/sec, each macropulse having 10^5 micropulses 0.2 ns wide separated in time by 5 ns. In order to shorten the data taking time, the laser had to be operated at high peak power which precluded the use of electron coincidence techniques to provide the signature for double photodetachment. The reliance on proton detection resulted in an increased sensitivity to a background due to Rydberg atoms. Moreoever, the tem-

poral jitter in the laser and the poor trigging conditions created significant deviations from normal counting statistics.

One of the most intriguing options for a new investigation of H^- double photodetachment is provided by a uv Kr-ion laser,[5.7] which by virtue of its cw operating condition, introduces the possibility of individual particle counting of electrons to create an almost unambiguous double-detachment signal through coincidence techniques. The magnetic field needed to separate the two escaping electrons from the primary beam is much smaller than that required for the high energy protons, which were detected in the previous experiment. Thus, the Rydberg contamination will be essentially eliminated. The residual gas stripping background will also be minimized through better definition of the interaction region and improved vacuum characteristics.

The precision measurement of double photodetachment utilize the High Resolution Atomic Beam (HiRAB) Facility which was constructed at LAMPF subsequent to the first H^- experiment and which provides improved user access to the experimental equipment as well as improved beam characteristics. With smaller ion-beam divergence and the use of newly developed momentum-bunching techniques--the relative momentum spread of the H^- beam can be reduced from 5×10^{-4} to 1×10^{-4} at the slight expense in reduction of beam energy from 800 to 716 MeV--the energy resolution of the experiment will be improved from 7-8 meV to

1-2 meV. Such an improvement will be important for a search for structure in the immediate vicinity of threshold. A new LAMPF H^- double photodetachment experiment is currently in the planning stage with anticipated running in 1993.[5.7]

5.3 Other Experimental Investigations

In addition to the previous H^- experiment discussed in Sect. 5.2, another useful future study would be the measurement of the angular width of the two escaping electrons as a function of excess energy. Such a study would test the $E^{1/4}$ power law for the angular distribution, which plays a central role in the Wannier threshold theory, as indicated in Chap. 2. Since the $E^{1/4}$ law is a small angle solution, any deviation from it does not neccessarily imply that the Wannier *ansatz* for the theory is incorrect. Neverthless a detailed study of the angular distribution should greatly improve our understanding of the nature of double escape . Since the triple differential cross section near threshold depends on the atomic target, this proposed experiment should idealy be done with atomic hydrogen. The experimental setup could be similar to that used for helium by Cevejanovic and Read[5.8] or by Pichou *et al.*,[5.9] both of which employed coincidence measurements of the two escaping electrons. The most severe problem in the previous experiments was the variation in detection efficiency when the angular position of the detectors was changed. The use of position-sensitive-detectors (PSD) in a new experiment should help alleviate this problem. The effeciency of a PSD is easily determined from a direct measurement with an electron beam of known intensity. Since collection of data at different angles can be carried out simultaneously, changes in experimental conditions will be minimized. Cross checks on angle-dependent systematic effects will also be faciliated and the data taking time will be

reduced significantly, thus improving the reliability of the results obtained.

The measurement of the electron energy partitioning funciton is yet another intersting experiment to consider. From a theoretical standpoint, only for the $^1S^e$ state have numerical calculations been carried out within the frame work of the Wannier model. Since it is known that the P and D states are also important near threshold, contributions from such states should be considered. The failure of the results of Hammond *et al.*[5.10] to reproduce the $^1S^e$ calculation could conceivably be caused by the omission of the P and D state contributions in the theory. Additional experiments of the kind performed by Hammond *et al.* on helium are quite difficult and should be repeated with care. Moreover, they should be extended to atomic hydrogen for comparative purposes.

Finally, since the experimental results presented in this thesis deal with spin-asymmetries in the ionization threshold region, it may well be that the deviation observed from the Wannier theory will reveal itself most prominently through spin dependence in the ionization process. Therefore, the natural extension of this experiment is the measurement of threshold ionzation for other atomic systems, such as lithium, potassium, rubidium and cesium. Although sodium experiment of Kelly *et al.*[5.11] failed to reveal any deviation from the Wannier theory, prudance dictates that it too should be the subject of reinvestigation. If indeed the Wannier theory is incorrect, as recent theoretical work[5.12] has suggested for doubly excited states of helium and H^-,

the energy dependence of the ionization spin-asymmetry may well be a function of the atomic system used. Thus future work on a variety of atomic systems should prove fruitful for furthering our understanding of one of the most basic problems in atomic physics.

Appendix 1. Performance of the Monochromator

In Sect. 3.1.2, we observed that the electrostatic monochromator did not operate at its design voltages. We provide some insight into the probable cause of this deficiency and its corollary effects on the energy resolution of the device. In the absence of magnetic fields, the energy, E_0, with which electrons can pass through a hemispherical monochromator can be derived by considering an electron moving in a circular path under electrostatic force. If V_{in} and V_{out} are voltages and R_{in} and R_{out} are the radii of the monochromator with the subscripts "in" and "out" refering to the inner and the outer hemispheres respectively, E_0 satisfies the relation

$$E_0 = \frac{e(V_{in} - V_{out})}{(\frac{R_{out}}{R_{in}} - \frac{R_{in}}{R_{out}})}, \tag{A1.1}$$

The energy of the electron beam can also be expressed in terms of the potential along the mean radius of the monochromator and the energy offset, $\Delta\phi$, determined by the work function in that region and the characteristics of the cathode as discussed in Sect. 3.3. It is easily shown that E_0 obeys the relation

$$E_0 = \frac{e(V_{in}R_{in} + V_{out}R_{out})}{R_{in} + R_{out}} - \Delta\phi, \tag{A1.2}$$

where for the purpose of this analysis, we take $\Delta\phi$ to be 2.6 eV, the same value we obtained for the beam at the interaction region in accordance with the electron energy calibration procedures detailed in Sect. 3.3. (It should be noted that this value of $\Delta\phi$ is not precisely correct since the monochromator was fabricated from

molybdenum and the interaction region, from stainless steel. The difference in the respected $\Delta\phi$ values, however, should be within 0.5 eV.)

Now the pass energy of the electrons is related to the FWHM value, $\Delta E_{1/2}$, of the electron beam after passing through the monochromator by the expression[A.1]

$$\frac{\Delta E_{1/2}}{E_0} = \frac{W}{2R_0}, \qquad \text{(A1.3)}$$

where W (1.8 mm) is the diameter of the angular stop, and R_0 (25.4 mm) is the mean radius of the electron path inside the monochromator. The inner and outer hemispheres of the monochromator are characterized by the radii R_{in} = 19.0 mm and R_{out} = 31.75 mm respectively, with applied operating voltages V_{in} = 12.9 V and V_{out} = 6 V. Then Eq. (A1.1) gives a pass energy E_0 of 6.5 eV. while Eq. (A1.2) yields a value of 5.98 eV. Such a big difference is an indication that the monochromator did not operate under the assumed conditions. This conclusion is reinforced by the disagreement between the experimentally determined energy spread of the beam and the value calculated predicted by Eqs. (A1.1) and (A1.3). The predicted values of the FWHM are 210 meV and 230 meV for pass energies of 5.98 eV and 6.5 eV respectively, as opposed to the measured FWHM value of 175 meV.

If the pass energy, E_0, in Eq. (A1.3) is taken as an unknown and $\Delta E_{1/2}$ is taken as the measured value of 175 meV, the electrons should pass through the monochromator with a nominal energy of 4.94 eV, a value that is lower than that associated with the path along the mean radius. Thus the electron trajectories through the

monochromator were probably not circular and indeed were characterized by coordinates that generally had radial components greater than the mean radius. Such a path distortion is probably attributable to stray magnetic fields emanating from the solenoids along the hydrogen beam line that had to be operated at higher currents than planned. For future experimental work, the monochromator should be enclosed by separate magnetic shielding to alleviate this problem.

Appendix 2. Inclusion of Contributions from Suppressed States

In Sects. 2.1.2 and 4.1.1, where the energy dependence of the spin asymmetry was considered as a function of excess energy, contributions to the total cross section from the suppressed states (for example, the $^1S^e$, $^1P^e$ states) were neglected because their cross sections follow a power law, E^n, with a higher exponent (n = 3.381 or 3.881 for atomic hydrogen) and are thus vanishingly small as E approaches zero in the near threshold region. For completeness, we consider the case when the contributions of the suppressed states are included to see the effects on the conclusions we have drawn in this thesis.

According to Eq. (2.57), the singlet and triplet ionization cross sections can be expressed as

$$\sigma_s = a_s E^m + b_s E^{3m} \tag{A2.1}$$

$$\sigma_t = a_t E^m + b_t E^{3m} , \tag{A2.2}$$

where a and b are constants with subscripts "s" and "t" refering to singlet and triplet configurations respectively. The slope of the spin asymmetry, $\frac{dA}{dE}$, follows from Eq. (1.9) or Eq. (4.13) and has the form

$$\frac{dA}{dE} = \frac{6m}{(1+3r)^2} \frac{a_s b_s E^{2m-1}}{(a_t+b_t E^{2m})^2} \left[\frac{a_t}{a_s} - \frac{b_t}{b_s} \right], \tag{A2.3}$$

where as before r is the ratio of the triplet cross section to the singlet cross section. When both b_s and b_t are zero, the slope is clearly zero. However, if b_s and b_t are non-zero, a positive slope (consistent with the experimental observations shown in

the hatched region of Fig. 4.1) requires that $a_{s,t}$ and $b_{s,t}$ satisfy the inequality

$$\frac{a_t}{a_s} > \frac{b_t}{b_s}. \tag{A2.4}$$

In the Wannier theory, the constants in front of the power law are unknown. However, since it is only their ratios that are relevant in Eq. (A2.4), we will show that it is possible to place constrains on the relative magnitudes of $a_{s,t}$ and $b_{s,t}$ within the context of the Wannier theory such that inequality in Eq. (A2.4) cannot be met. Since the spin asymmetry, A, at threshold is about 0.5, as seen from Fig. 4.1 with $P_e = 0.27$ and $P_H = 0.515$, we deduce from Eq. (1.9) that r ≈ 0.2. It follows that a_s must be greater than a_t, because the Wannier threshold term, E^m, has to be dominant as $E \rightarrow 0$. We can explain this result qualitatively from the behavior of the final-state wavefunctions that are known to be important for the near threshold ionization; namely, the S, P, and D states.

Table (A.1) summarizes the properties of these final states that are relevant to our discussion. (Note that the P^e and D^o states are excluded because they are not accessible due to conservation of parity and angular momentum.) The first column in Table (A.1) lists the quantum states; the second column contains the asymptotic wave functions for each final state along the Wannier ridge ($\zeta \sim 0$ and $\gamma \sim 0$) with the c_j (j = 1,...,10) being arbitrary constants;[A.2] the third column contains expressions for the total cross sections for each individual state with f_i (i = 1,...,10) being unknown coefficients in front of the two exponential energy terms. If the wave

function has a node in its angular coordinate γ, its contribution to the total cross section must be small because the amplitude of wavefunction is small and hence its assocaited transition matrix element, calculated from Eq. (2.1), must be small. The corresponding f_i coefficients in Table (A.1) that are small are identified by the superscipt γ. For example, in the case of the $^1P^o$ state, the wave function has the asymptotic form $c_2\gamma + c_3\zeta$, which is a superposition of even and odd wave functions under two electron radial interchange, since $\zeta \rightarrow -\zeta$ and $\gamma \rightarrow \gamma$ when $(r_1,r_2) \rightarrow (r_2,r_1)$. As indicated by Eq. (2.24), wave functions that are even under radial interchange obey the Wannier law with the exponent m, while wave functions that are odd have the exponent 3m. Thus the even wave function, $c_2\gamma$, results in a contribution to the total cross section with the Wannier power form $f_2^{\gamma} E^m$, while the odd wave function $c_3\,\zeta$ rersults in a contribution with the suppressed power form, $f_3\,E^{3m}$. The f_i coefficents without the γ superscripts are relatively large.

From Table (A.1), it is clear that a_s and a_t can be expressed in terms of the f_i coefficients as

$$a_s = f_1 + f_2^{\gamma} + f_4 \tag{A2.5}$$

$$a_t = f_7 + f_9^{\gamma} . \tag{A2.6}$$

Comparing Eq. (A2.5) with Eq. (A2.6) shows that a_s is greater than a_t, since the former has an additional contribution from the $^1S^e$ state, as represented by the coefficient f_1, and since S-states contribute strongly to the total cross section, as shown by Pan and Starrace.[A.3] This result is consistent with the experimental observation

of r ≈ 0.2. The relative magnitudes of b_s and b_t can be obtained in a similiar way. In terms of the f_i coefficients, we have

$$b_s = f_3 + f_5 \tag{A2.7}$$

$$b_t = f_6 + f_8^{\gamma} + f_{10} . \tag{A2.8}$$

Now the cross section for the triplet state, b_t, has a relatively large contribution from the $^3S^e$ state, as represented by the coefficient f_6. Moreover, it has an additional term, as represented by the coefficient f_8^{γ} compared to the singlet state. This is the reverse of the situation we had for "a" coefficients. Thus b_t should be larger than b_s. The foregoing arguments are further enhanced by recent theoretical caluclations of Pan and Starrace,[A.4] which show that the cross section for the ^1P state is 10% of that for the ^3P state, and the cross section for the ^3D state is 12.5% of that for the ^1D state. Their results thus require that f_2^{γ} be 10% of f_7^{γ}, and f_3^{γ} be 12.5% of f_4, which can be expected qualitatively from Table (A.1).

In summary, since b_t is greater than b_s, while a_s is greater than a_t, the Wannier theory predicts a negative slope (with unknown magnitude) for the spin asymmetry if contributions from the suppressed states are really observable. This prediction contradicts our experimental results. It should be noted that the conclusion should hold even if higher angular momentum states (F, G etc.) are included, since their relative contributions are predicted to be small.[A.3]

Table A1. Characteristics of S, P and D Final States.

State	Wave function	Cross section
$^1S^e$	$c_1 + 0\cdot\zeta$	$f_1E^m + 0\cdot E^{3m}$
$^1P^o$	$c_2\gamma + c_3\zeta$	$f_2^{\gamma} E^m + f_3E^{3m}$
$^1D^e$	$c_4 + c_5\zeta$	$f_4E^m + f_5E^{3m}$
$^3S^e$	$0\cdot\gamma + c_6\zeta$	$0\cdot E^m + f_6E^{3m}$
$^3P^o$	$c_7 + c_8\zeta\gamma$	$f_7E^m + f_8^{\gamma} E^{3m}$
$^3D^e$	$c_9\gamma + c_{10}\zeta$	$f_9^{\gamma} E^m + f_{10}E^{3m}$

Appendix 3. The 90° Bender as an Energy Analyzer

In the cooled polarized electron source discussed in Sect. 5.1, it was noted that an aperture was placed at the focusing plane (the plane of the 100-mm diameter disk connected to the bender as shown in Fig. 5.1) of the 90° bender. It can be derived from Purcell's[A.1] work that the trajectories of a charged particle passing through a 90° bender and arriving at the focusing plane satisfy the relations

$$\frac{R_2}{R_0} = \frac{\Delta E_b}{E_0}(1 + \frac{L}{R_0}) \tag{A3.1}$$

$$\alpha_2 = -\frac{R_1}{R_0} + \frac{\Delta E_b}{E_0}, \tag{A3.2}$$

where R_0 is the mean radius of the electron trajectory inside the 90 degree bender, R_1 and R_2 are the radii of the apertures in the entrance and the focusing plane respectively, E_0 is the mean pass energy, $\Delta E_b = E' - E_0$ is the deviation of the energy E' characterizing any particular trajectory from the mean pass energy E_0, L is the distance between the exit and the focusing planes of the 90° bender, and α_2 is the angular divergence of the beam at the exit plane. Eq. (A3.1) determines the maximun energy spread (base width) with which electron beam can still pass through the bender. Since the transmission function of a 90^0 spherical bender is triangular,[A.5] the FWHM energy resolution of the 90^0 bender can be shown from Eq. (3.1) to be

$$\Delta E_{\frac{1}{2}}^{b} = \frac{1}{2}\Delta E_b = \frac{R_2}{R_0(1 + \frac{L}{R_0})}. \tag{3.3}$$

For the design presented in Fig. 5.1, with R_0 = 25.4 mm, R_2 = 1 mm, and L = 36 mm, the FWHM energy resolution is calculated to be

$$\Delta E^b_{\frac{1}{2}} = 16.3E_0\,, \qquad (\Delta E^b_{\frac{1}{2}} \text{ in meV and } E_0 \text{ in eV}) \tag{A3.4}$$

or in term of a Gassian half-width,

$$\sigma_b = 6.9E_0 \qquad (\sigma_b \text{ in meV and } E_0 \text{ in eV})\,. \tag{A3.5}$$

At the three pass energies 33.3, 60 and 83.3 eV where the energy distributions of the thermal cathode were measured, the corresponding Gaussian widths, σ_b, for the energy resolution of the bender, are 230, 414 and 574 meV respectively, all of which are larger than the measured values of energy spread, σ_m, of the beam which were given in Sect. 5.1.3 as 87.5, 90 and 105 meV respectively. Thus we can neglect the influence of the 90^0 bender on the energy distribution measurements of the electron beam passing through it within the statistical uncertainty (± 10 meV) of the retarding field analyzer. If the FWHM energy spread of the electron beam emanating from the GaAs crystal is about 500 meV, the pass energy of the beam through the 90^0 should be greater than 80 eV.

References

Chapter 1

1.1 P. Kush and H. M. Foley, Phys. Rev. 74, 250 (1948); C. S. Wu *et al.*, Phys. Rev. 105, 1413 (1957); C. Y. Prescott *et al.*, Phys. Lett. 77B, 347 (1978).

1.2 J. Kessler, *Polarized Electrons, 2nd Edition* (Springer-Verlag, Berlin, 1985).

1.3 G. F. Hanne, Phys. Rep. 95, 95 (1983); J. Kessler, Adv. At. Mol. Opt. Phys., 27, 81 (1991).

1.4 M. S. Lubell, in *Coherence and Correlation in Atomic Collisions*, ed. H. Kleinpoppen and J. F. Williams, pp. 663-687 (Plenum, New York, 1980).

1.5 G. Flechter *et al.*, Phys. Rev. A 31, 2854 (1985).

1.6 N. F. Mott, Proc. Roy. Soc. A124, 425 (1929); N. Sherman, Phys. Rev. 103, 1601 (1956).

1.7 G. Holzwarth and H. J. Meister, *Tables of Asymmetry, Cross Section and Related Functions for Mott Scattering of Electrons by Screened Au and Hg Nuclei* (University of Munich, Munich, Germany, 1964); Nucl. Phys. 59, 56 (1964); Shin-R Lin, Phys. Rev. 133, A965 (1964); W. Buhring, Z. Physik 208, 286 (1968); 212, 61 (1968); A. W. Ross and M. Fink, Phys. Rev. A. 38, 6055 (1988).

1.8 G. Flechter, T. J. Gay, and M. S. Lubell, Phys. Rev. A 34, 911 (1986); L. G. Gray, M. W. Hart, F. B. Dunning, and G. K. Walters, Rev. Sci. Instrum. 50, 88 (1984).

1.9 W. Gerlach and O. Stern, Z. Physik 8, 110 (1921); N. Chan *et al.*, Z. Physik D 10, 393 (1988), and references therein.

1.10 H. G. Dehmelt, Phys. Rev. 109, 381 (1958).

1.11 W. Lichten and S. Schultz, Phys. Rev. 116, 1132 (1959).

1.12 R. E. Collisions *et al.*, Phys. Rev. A 3, 1976 (1971).

1.13 G. F. Hanne and J. Kessler, Phys. Rev. Lett. 33, 341 (1974).

1.14 R. L. Long *et al.*, Phys. Rev. Lett. 15, 1 (1965); V. W. Hughes, in *High Energy Physics with Polarized Beams and Polarized Targets*, ed. by G. H. Thomas (AIP Conf. Proc. No. 51, Am. Inst. Phys., New York, 1979), p. 171

1.15 U. Fano, Phys. Rev. 178, 131 (1969); Phys. Rev. 184, 250 (1969).

1.16 M. S. Lubell and W. Raith, Phys. Rev. Lett. 23, 211 (1969).

1.17 D. T. Pierce, F. Meier, and P. Zurcher, Phys. Lett. A51, 465 (1975); D. T. Pierce *et al.*, Rev. Sci. Instrum. 51, 478 (1980).

1.18 T. Marnyanra *et al.* Phys. Rev. Lett. 66, 2376 (1991).

1.19 C. G. Shull *et al.*, Phys. Rev. 63, 29 (1943).

1.20 A. Gellrich and J. Kessler, Phys. Rev. A 43, 204 (1991)l; Jeoke, J. Kessler and G. F. Hanne, Phys. Rev. Lett. 59, 1413 (1987); T. Gay *et al.* (submitted to Rev. Sci. Instrum.)

1.21 J. Unguris, R. J. Cellota, and D. T. Pierce, Rev. Sci. Instrum. 57, 1314 (1986); J. J. McClelland *et al.*/ Rev. Sci. Instrum. 60, 683 (1987)

1.22 O. Berger and J. Kessler, J. Phys. B 19, 3539 (1986).

1.23 F. Faussen *et al.*, J. Phys. B 20, 151 (1987).

1.24 H. Borgmann *et al.*, J. Phys. B 20, 1619 (1987).

1.25 V. Nickich *et al.*, Z. Physik D 16, 261 (1990).

1.26 M. J. Alguard *et al.*, Phys. Rev. Lett. 39, 334 (1977); G. D. Fletcher *et al.*, Phys. Rev. A 31, 2854 (1985).

1.27 D. Hils and H. Kleinpoppen, J. Phys. B 11, L283 (1978); 15, 3347 (1982);

1.28 G. Baum *et al.*, J. Phys. B 18, 531 (1985), Phys. Rev. A 40, 6734 (1989); in *17th Int. Conf. on the Physics of Electronic and Atomic Collisions, Brisbane, Australia, July 10-16, 1991, Abstracts of Papers,* p. 106; Phy. Rev. Lett. 57, 1855 (1986); J. Phys. B. 22, 1667 (1989).

1.29 J. J. McCelland *et al.*, Phys. Rev. Lett. 58, 2198 (1987).

1.30 M. H. Kelley *et al.*, Phys. Rev. Lett. 51, 2191 (1983); S. R. Lorentz *et al.*, Bull. Am. Phys. Soc. 36, 1280 (1991).

1.31 See discussions in Chap. 2.

1.32 J. W. McGowan and E. M. Clark, Phys. Rev. 167, 43 (1969).

1.33 C. E. Brion and G. E. Clarke, Phys. Rev. Lett. 20, 241 (1968); P. Marchand *et al.*, Phys. Rev. 180, 123 (1969).

1.34 I. Vinkalns and M. Gailitis, in *5th Int. Conf. on the Physics of Electronic and Atomic collisions, Leningrad, USSR, July 17-23, 1967, Abstracts of Papers,* ed. I. P. Flaks (Nauka, Leningrad, 1967) p. 648

1.35 F. H. Read, J. Phys. B 17, 3965 (1984).

1.36 S. Cvejanovic and F. H. Read, J. Phys. B 7, 1180 (1974).

1.37 F. Pichou *et al.*, J. Phys. B 11, 3683 (1978).

1.38 P. Hammond *et al.*, J. Phys. B 18, L141 (1985).

1.39 J. B. Donahue *et al.*, Phys. Rev. Lett. 48, 1538 (1982).

1.40 Y. K. Bae and J. Peterson, Phys. Rev. A 37, 3254 (1988).

1.41 M. H. Kelley *et al.*, Phys. Rev. Lett. 51, 2191 (1983).

1.42 G. Baum *et al.*, in *17th Int. Conf. on the Physics of Electronic and Atomic Collisions, Brrisbane, Australia, July 10-16, 1991, Abstracts of Contributed Papers* p. 106.

1.43 E. Schubert *et al.*, J. Phys. B 14, 3267; H. Ehrhardt *et al.*, J. Phys. B 2, 1559 (1972).

1.44 P. Fournier-Lagarde *et al.*, J. Phys. B 17, L591 (1984).

1.45 P. Schlemmer *et al.*, Phys. Rev. Lett. 63, 252 (1989); T. Rosel *et al.*, in *Proc. of 2nd Eur. Conf. on (e, 2e) Collisions and Related Problems,* Kaiserslautern, 1989, p. 69 (unpublished).

1.46 P. Sells, J. Mazeau, and A. Huetz, J. Phys. B. 23, 2613 (1990).

1.47 C. Pan and T. Starace, Phys. Rev. Lett. 67, 185 (1991); D. Madison (private communication).

1.48 H. Kossmann, V. Schmidt, and T. Anderson, Phys. Rev. Lett. 60, 1266 (1988).

1.49 J. A. R. Samson and G. C. Angel, Phys. Rev. Lett. 61, 1584 (1988).

1.50 H. Klar and W. Schlecht, J. Phys. B: 9 1699 (1976).

1.51 J. M. Feagin and R. D. Filipczyk, Phys. Rev. Lett. 64, 384 (1990).

1.52 P. Lablanquie *et al.*, Phys. Rev. Lett. 58, 992 (1987).

1.53 S. D. Price and J. H. d. Eland, J. Phys. B 22, L153; J. Phys. B. 23, 2269 (1990).

1.54 See Sect. 2.2.

Chapter 2

2.1 E. P. Wigner, Phys. Rev. 73 1002 (1948).

2.2 A. R. P. Rau, Phys. Rev. A 4 207 (1971).

2.3 G. H. Wannier, Phys. Rev. 90 817 (1953).

2.4 U. Fano , Phys. Rev. A22 2660 (1980), J. Phys. B 7, L401 (1974).

2.5 R. Peterkop, J. Phys. B 16 L587 (1983).

2.6 I. Vinkalns and M. Gailitis , in *5th Int. Conf. on the Physics of Electronic and Atomic collisions, Leningrad, USSR, July 17-23, 1967, Abstracts of Papers,* ed. I. P. Flaks (Nauka, Leningrad, 1967) p. 648

2.7 F. H. Read, J. Phys. B 17, 3965 (1984).

2.8 A. R. P. Rau, J. Phys. B 9, L283 (1976); J. Phys. B 22 189 (1989).

2.9 J. M. Feagin, J. Phys. B 17, 2433 (1984).

2.10 M. Gailitis and R. Peterkop, J. Phys. B 22, 1231 (1989).

2.11 T. A. Roth, Phys. Rev. A 5, 476 (1972).

2.12 H. Klar and W. Schlecht, J. Phys. B 9, 1699 (1976).

2.13 C. Greene and A. R. P. Rau, J. Phys. B 16, 99 (1983); Phys. Rev. Lett. 48, 533 (1982).

2.14 A. D. Stauffer, Phys. Lett. 91A, 114 (1982).

2.15 R. Peterkop and A. Liepinsh, J. Phys. B 14, 4125 (1981).

2.16 H. Klar, J. Phys. B 14, 3255 (1981).

2.17 R. Peterkop, J. Phys. B. 4, 513 (1971).

2.18 A. Temkin, Phys. Rev. Lett. 16, 835 (1966); A. Temkin, A. K. Bhatia, and E. C. Sullivan, Phys. Rev. 176, 80 (1968).

2.19 A. Temkin, in *Recent Developments in Electron-Atom and Electron-Molecule Collisions, Proceedings of the Daresbury Study Weekend, 26-27 March 1982* 44 (unpublished).

2.20 A. Temkin, Phys. Rev. Lett. 49, 365 (1982).

2.21 A. Temkin and Y. Hahn, Phys. Rev. A 9, 708 (1974).

2.22 A. Temkin, J. Phys. B 7, L450 (1974).

2.23 A. Temkin, in *Electronic and Atomic Collisions*, ed. by J. Eichler, I. V. Hertel, and N. Stolterfoht (Elsevier, Amsterdam, 1984), p. 755.

2.24 M. K. Srivastava and A. Temkin, Phys. Rev. A 43, 3570 (1991).

2.25 A. Temkin, J. Phys. B 24, 2147 (1991).

2.26 C. H. Greene and A. R. P. Rau, Phys. Rev. A 32, 1352 (1985).

Chapter 3

3.1 N. Chan *et al.*, Z. Physik D 10, 393 (1988).

3.2 J. W. McGowan and E. M. Clark, Phys. Rev. 167, 43 (1969).

3.3 X. Q. Guo *et al.*, Rev. Sci. Instrum. 61, 1858 (1990).

3.4 C. K. Kuyatt and J. A. Simpson Rev. Sci. Instrum. 38, 103 (1967).

3.5 F. C. Tang, Ph.D. thesis, City University of New York, 1989.

3.6 G. D. Fletcher, T. J. Gay and M. S. Lubell, Phys. Rev. A 34, 911 (1986).

3.7 H.-J. Drouhin and M. Eminyan, Rev. Sci. Instrum. 57, 1052 (1986).

3.8 H. Rose and R. Spehr, *Adv. Electr. Electron Phys. Supp. 13 C,* ed. R. Spehr (Academic Press. Inc., 1983), p. 475

3.9 H.-J. Drouhin *et al.*, J. Phys. Lett. 44, L1027 (1983).

3.10 H.-J. Drouhin *et al.*, Phys. Rev. B 31, 3859,3872 (1985).

3.11 J.S. Blackmore, J. Appl. Phys. 53, R123 (1982).

3.12 A. J. Szadkowski *et al.*, J. Appl. Phys. 53, 557 (1982).

3.13 D. M. Crowe *et al.*, J. Phys. B 23, L325 (1990).

3.14 See Sect. 1.2.

3.15 T. F. Gallagher Rep. Prog. Phys. 51, 143 (1988).

3.16 H. R. J. Walters Phys. Rep. 116, 1 (1984).

3.17 K. Omidvar Phys. Rev. A 140, 38 (1965).

3.18 J. Callaway *et al.* Phys. Rev. A 36, 2576 (1987).

3.19 T. T. Scholz *et al.* J. Phys. B 23, L467 (1990).

3.20 A. H. Mahan, A. Gallagher, and S. J. Smith, Phys. Rev. A 13, 156 (1976).

3.21 G. W. Series ed., *The spectrum of Atomic Hydrogen : Advances* (World Scientific, Singapore, 1988).

Chapter 4

4.1 A. Temkin (private conmunication).

4.2 Y. K. Bae and J. Peterson, Phys. Rev. A 37, 3254 (1988).

4.3 J. B. Donahue *et al.*, Phys. Rev. Lett. 48, 1538 (1982).

4.4 S. Siegel, *Nonparametric Statistics for the Behavioral Sciences* (Mc Graw Hill, New York, 1956); J. V. Bradley, *Distribution-Free Statistical Tests* (Prentice Hall, Englewood Cliff, NJ, 1968).

4.5 J. Durbin and G. S. Watson, *Biometrica* 37, 409 (1950); 38, 159 (1959).

4.6 J. Johnson, *Econometric Methods, 2nd Edition* (McGraw Hill, New York, 1972).

4.7 F. Pichou *et al.*, J. Phys. B 11, 3683 (1978).

4.8 F. H. Read, J. Phys. B 17, 3965 (1984).

4.9 P. Hammond *et al.*, J. Phys. B 18, L141 (1985).

4.10 G. Baum *et al.*, in *17th Int. Conf. on the Physics of Electronic and Atomic Collisions, Brisbane, Australia, July 10-16, 1991, Abstracts of Contributed Papers*p. 106; J. Phys. B 18, 531 (1985).

4.11 M. H. Kelley *et al.*, Phys. Rev. Lett. 51, 2191 (1983).

4.12 P. Schlemmer *et al.*, Phys. Rev. Lett. 63, 252 (1989); T. Rosel *et al.*, in *Proc. of 2nd Eur. Conf. on (e, 2e) Collisions and Related Problems,* Kaiserslautern,1989, p. 69 (unpublished).

4.13 C. Pan and T. Starace, Phys. Rev. Lett. 67, 185 (1991).

4.14 D. Madison (private conmunication).

4.15 See for example, R. V. Jensen *et al.*, Phys. Rev. Lett. 63, 2771 (1989) and references therein.

4.16 R. Peterkop, J. Phys. B. 4, 513 (1971).

4.17 M. Gailitis and R. Peterkop, J. Phys. B 22, 1231 (1989).

4.18 G. H. Wannier, Phys. Rev. 90, 817 (1953).

4.19 See discussions in chap. 2.

4.20 J. M. Feagin, J. Phys. B 17, 2433 (1984).

Chapter 5

5.1 Corning Glass Works, Corning, New York, *Macor™* Machinable Glass Ceramics; Cryogenics (May, 1975).

5.2 H.-J. Droubin *et al.*, Phys. Rev. B 31, 3859,3872 (1985); H.-J. Droubin and M. Eminyan, Rev. Sci. Instrum. 57, 1052 (1986).

5.3 J. H. Moore and C. C. David, and M. A. Coplan, *Building Scientific Apparatus, 2nd Edition* (Addison-Wesley, New York, 1989). 2nd ed., 1989)

5.4 J. A. Simpson, Rev. Sci. Instrum. 32, 1283 (1961).

5.5 F. C. Tang *et al.*, Rev. Sci. Instrum. 57, 3004 (1986).

5.6 J. B. Donahue *et al.*, Phys. Rev. Lett. 48, 1538 (1982).

5.7 M. S. Lubell *et al.*, LAMPF proposal #1237 (1991).

5.8 S. Cvejanovic and F. H. Read, J. Phys. B 7, 1180 (1974).

5.9 F. Pichou *et al.*, J. Phys. B 11, 3683 (1978).

5.10 P. Hammond *et al.*, J. Phys. B 18, L141 (1985).

5.11 M. H. Kelley *et al.*, Phys. Rev. Lett. 51, 2191 (1983).

5.12 K. Richter and D. Wintgen, J. Phys. B. 23, L197 (1990); J. M. Rost *et al.*, J. Phys. B 24, 2455 (1991); G. S. Ezra *et al.* (submitted to J. Phys. B.), and references therein.

5.13 Omega Engineering Inc., Stamford, CT. *The Temperature Handbook* (1991).

Appendices

A.1 C. E. Kuyatt and J. A. Simpson, Rev. Sci. Instrum.. 38, 103 (1967); E. M. Purcell, Phys. Rev. 54, 818 (1938).

A.2 C. Greene and A. R. P. Rau, J. Phys. B 16, 99 (1983).

A.3 C. Pan and T. Starace, Phys. Rev. Lett. 67, 185 (1991).

A.4 T. Starace (private conmunication).

A.5 M. E. Rudd, in *Low Energy Electron Spectrometry*, ed. by K. D. Sevier, Wiley-Interscience, New York, 1972, Chap. 2, Sect. 3; Kisker *et al.*, Rev. Sci. Instrum. 50, 1598 (1979).